Personal Account

THE CHEMICAL RECORD

DOI: 10.1002/tcr.201500279

The Application of Graphene and Its Derivatives to Energy Conversion, Storage, and Environmental and Biosensing Devices

Asif Ali Tahir,*[a] Habib Ullah,[a] Pitchaimuthu Sudhagar,[b] Mohd Asri Mat Teridi,*[c] Anitha Devadoss,[d] and Senthilarasu Sundaram*[a]

ABSTRACT: Graphene (GR) and its derivatives are promising materials on the horizon of nanotechnology and material science and have attracted a tremendous amount of research interest in recent years. The unique atom-thick 2D structure with sp^2 hybridization and large specific surface area, high thermal conductivity, superior electron mobility, and chemical stability have made GR and its derivatives extremely attractive components for composite materials for solar energy conversion, energy storage, environmental purification, and biosensor applications. This review gives a brief introduction of GR's unique structure, band structure engineering, physical and chemical properties, and recent energy-related progress of GR-based materials in the fields of energy conversion (e.g., photocatalysis, photoelectrochemical water splitting, CO_2 reduction, dye-sensitized and organic solar cells, and photosensitizers in photovoltaic devices) and energy storage (batteries, fuel cells, and supercapacitors). The vast coverage of advancements in environmental applications of GR-based materials for photocatalytic degradation of organic pollutants, gas sensing, and removal of heavy-metal ions is presented. Additionally, the use of graphene composites in the biosensing field is discussed. We conclude the review with remarks on the challenges, prospects, and further development of GR-based materials in the exciting fields of energy, environment, and bioscience.

Keywords: energy conversion, energy storage, graphene, photocatalysis, sensors

1. Introduction

The main challenges for scientific and technological research into solar energy conversion, energy storage, and environment are the stability, durability, and performance of low-cost functional materials. The discoveries of sp^2-hybridized carbon nanomaterials such as buckminsterfullerene,[1,2] carbon nanotubes,[3] and graphene (GR)[4] have revolutionized the research directions in the fields of physics, material science, chemistry,

[a]A. Ali Tahir, H. Ullah, S. Sundaram
Environment and Sustainability Institute (ESI)
University of Exeter
Penryn Campus
Penryn
Cornwall TR10 9FE (UK)
E-mail: a.tahir@exeter.ac.uk
E-mail: hu203@exeter.ac.uk
E-mail: s.sundaram@exeter.ac.uk
[b]P. Sudhagar
School of Chemistry and Chemical Engineering
Queen's University Belfast
David Keir Building
Belfast BT9 5AG (UK)
E-mail: S.Pitchaimuthu@qub.ac.uk
[c]M. Asri Mat Teridi
Solar Energy Research Institute
National University of Malaysia
43600 Bangi
Selangor
(Malaysia)
E-mail: asri@ukm.edu.my
[d]A. Devadoss
College of Engineering
Swansea University
Singleton Park
Swansea SA2 8PP (UK)
E-mail: anitha.devadoss@swansea.ac.uk

and life sciences.[5] These carbon nanomaterials will continue to play a vital role in overcoming the major technological and practical challenges of material science. Among the carbon nanomaterials, GR is the most exciting material due to its monolayer structure composed of a network of six-membered rings.[6] Considering its planar state, GR can be rolled into zero-dimensional spherical fullerenes, one-dimensional carbon nanotubes, or two-dimensional honeycomb structures, or stacked into three-dimensional graphite.[7] GR can be used as a basic building block for all carbon nanomaterials and in composites with other materials. GR has unique and stimulating properties, such as high theoretical surface area (2630 $m^2\ g^{-1}$),[8] high room-temperature charge carrier mobility (~100000 $cm^2\ V^{-1}\ s^{-1}$),[9] the highest electrical conductivity (10^6 S cm^{-1}), high thermal conductivity (~2000 to 5000 $W\,m^{-1}\,K^{-1}$),[10] and the capacity to support large electrical current density (10^8 A

Asif A. Tahir graduated from the Department of Inorganic Chemistry at Quaid-i-Azam University, Pakistan, in 2009. He worked as a research associate at Loughborough University for three years and then moved to the University of Liverpool before joining the College of Engineering, Mathematics and Physical Sciences (CEMPS) at the University of Exeter as a Lecturer in Renewable Energy. He specializes in the fabrication of nanomaterials using state-of-the-art techniques for solar energy conversion and photocatalysis. His research focus includes the design, synthesis, and characterization of new materials using soft chemistry approaches and the optimization of nanomaterials for high performance.

Habib Ullah obtained his M.Phil. in Physical Chemistry from the Institute of Chemical Sciences, University of Peshawar, Pakistan, in 2014. Currently, he is doing his Ph.D. in Renewable Energy at CEMPS, University of Exeter, under the supervision of Dr. Asif A. Tahir. His research involves the design of novel materials, i.e., conjugated organic polymers (graphene), inorganic metal oxides, and their composites, for sensors, solar cells, rechargeable batteries, light-emitting diodes, and corrosion inhibition applications.

Pitchaimuthu Sudhagar is currently working as a Research Fellow at the School of Chemistry and Chemical Engineering, Queen's University Belfast, UK. He was the recipient of a JSPS Post-Doctoral Fellow Award under the guidance of Prof. Akira Fujima at the Photocatalysis International Research Center, Tokyo University of Science, Japan, during 2013–2015. He received his Ph.D. degree (Physics) from Bharathiar University, India, and later moved to the Center for Next Generation Dye-Sensitized Solar Cells of Hanyang University, South Korea (2009–2013). He has published about 67 articles in peer-reviewed international journals and three book chapters. His research interest is to pioneer the creation of nanostructured electrodes, semiconductor photoabsorbers, and electrocatalysts for high-efficiency solar cells and solar fuel cells.

Mohd Asri Mat Teridi received his Ph.D. on cathodic sensitization solar cells in 2012 from Loughborough University. He joined the Solar Energy Research Institute, National University of Malaysia, as a Junior Research Fellow/Lecturer in 2007. After he received his Ph.D., he was appointed as Research Fellow/Senior Lecturer at the same university in 2013. His recent research activity has focused on nanostructured metal oxides for solar water splitting, perovskite solar cells, polymer solar cells, and dye-sensitized solar cells.

Anitha Devadoss received her Ph.D. from Dublin City University in 2011 under the supervision of Prof. Robert J. Forster and Prof. Tia E. Keyes. She worked as a Brain-Korea-21 postdoctoral fellow at Hanyang University, South Korea, and later as a researcher at Tokyo University of Science, Japan. Currently, she works at Swansea University, UK, and her research focuses on developing various biosensors (electrochemical, ECL, and photoelectrochemical) and signal amplification strategies for highly sensitive and selective bioanalysis. She has published over 25 research articles.

Senthilarasu Sundaram graduated from Bharathiar University, Coimbatore, India, in 2006. Currently, he works at the University of Exeter, UK, and his research focuses on the development of nanostructured solar cells, especially dye-sensitized solar cells and perovskite thin-film solar cells through low-cost fabrication techniques. He is concentrating specifically on scale-up engineering challenges in novel solar cells, system-level integration, and spectral dependence analysis.

cm^{-2}).[11] Thus, GR is a unique material for capacitors,[12] batteries,[13] and sensors.[14] On the other hand, its high surface area, excellent transparency, light absorption, and charge transport properties have triggered huge interest from different research fields concerned with energy conversion and environmental pollution remediation, which are gaining traction in modern society.[7,15] Along with energy conversion, storage, and photocatalysis of environmental pollution, GR also has a wide range of other applications in the fields of nanoelectronics, optoelectronics, chemical and biochemical sensing, polymer composites, intercalation materials, and drug delivery.[16]

Certainly, the discovery of GR in 2004 has opened up enormous scientific opportunities. Recently, technologies for preparing GR, its derivatives, and GR-based nanomaterials/nanocomposites have grown rapidly because of more sophisticated fabrication methods. The versatile methods developed for the synthesis of GR and its derivatives include chemical vapor deposition (CVD) on metal surfaces; epitaxial growth on single-crystal SiC; micromechanical cleavage of graphite crystals; and "top-down" exfoliation of graphite by means of oxidation, intercalation, and/or sonication.[17] The chemical oxidation of graphite to GR oxide (GO) and its subsequent reduction to reduced GR oxide (rGO) was considered as an effective method for preparing GR nanosheets because of its scalability, high yield, and low cost.[18] The rGO possesses reactive groups, such as epoxide, hydroxyl, carbonyl, and carboxylic groups, allowing the development of functionalized GR-based materials.[18] There is increased popularity in the use of GR, GO, and rGO in energy conversion (photoelectrochemical (PEC) water splitting, photocatalytic water splitting, and photovoltaic devices), energy storage (capacitors and batteries), and environmental applications (photocatalytic degradation of pollutants, gas sensors and heavy-metal removal). Therefore, it is necessary to compile a comprehensive review of the energy and environmental applications of GR and its derivatives.

The progress made in GR-based materials for energy and environmental applications has been discussed in several review articles with a focus on either specific materials or general preparation methods and functionalization.[1,7,15,19] Recently, Zhang et al. have compiled a few excellent reviews highlighting the importance of GR as a template for composite photocatalyst synthesis and an excellent candidate for artificial photosynthesis.[7,20] They also critically reviewed the entrepreneurial aspects of the commercialization of GR-based technologies.[7] This article aims to give a relatively systematic update on the development and current research status of GR-based materials from the perspective of energy conversion, energy storage, and environmental purification. After a brief introduction of the structure and properties of GR, GO, and rGO, we will discuss the electron acceptor and transport properties of GR and its derivatives. Each section provides key challenges and requirements to enhance the performance of GR-based materials in photocatalysis and energy storage. Afterwards, we explore and summarize the recent progress of GR usage and its derivatives for PEC and photocatalytic water splitting and photocatalytic conversion for fuels, photovoltaics, and applications in supercapacitors, batteries, degradation of pollutants, heavy-metal removal, and so forth. The main applications of GR and its derivatives are summarized in Figure 1. In addition, key challenges encountered with GR-based materials, for their effective use in energy conversion, storage, and environmental applications, are discussed in the final section. This update promotes a more efficient and rational review of the structural and electronic properties of GR and a more efficient design of GR-based materials for solar energy conversion, energy storage, biosensors, and environmental applications.

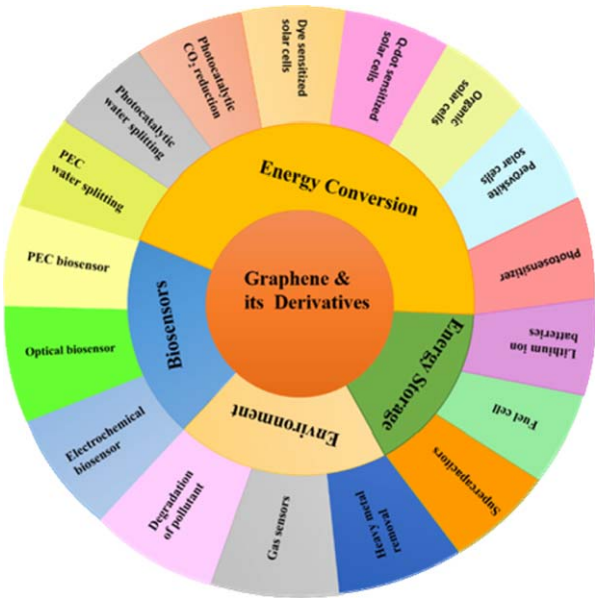

Fig. 1. Overview of GR-based materials in energy conversion, energy storage, environmental, and sensing applications.

1.1. Structure and Properties of Graphene

Carbon, which is a past, present, and future backbone of chemistry, regained popularity in the last decade and won the Nobel Prize for Physics in 2010.[21] The different types of carbon produced at different stages and in different forms such as C^{12}, coal, and gasoline have been used in electrode technologies, lubricants, carbon-fiber-reinforced plastics, pencil lead, and nanotechnology. GR is a carbon-containing compound that has a two-dimensional stable geometrical structure containing delocalized π-conjugated systems. Generally, GR exists in different isotropic forms, three of which are depicted in Figure 2. The versatile applications of GR stem from its unique structure and highly anisotropic properties. Its characteristic

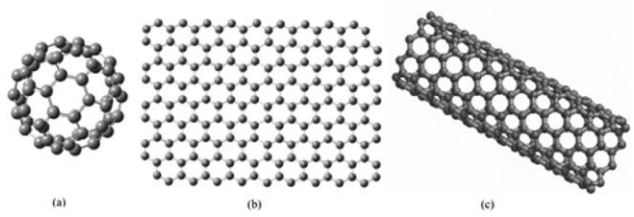

Fig. 2. Three different geometrical structures of GR.

properties depend on the orientation and the dislocation of sheets in an ensemble structure to create macroscopic properties.[22] Each geometrical shape of GR has its own technological applications in the fields of energy storage and sensors, etc. Its simplicity, ease of synthesis, affordability, feasible methods of handling in electronic devices, retention of its unique characteristics in different shapes, compatibility with industrial processes, and large volume production with a reasonable time and effort make it attractive to scientists. Ball-shaped GR molecules, which consist of hollow cage molecules of dimensionless fullerene dots as shown in Figure 2a, are commonly known as buckyballs. Derivatives have been used as acceptors in donor–acceptor photovoltaic cells. This carbon-containing ball-shaped GR has a strong ability to accept electrons from nucleophilic species. Once an electron enters, it then circulates around the backbone, which leads to the production of an electrical current.

GR nanoribbons (GNRs) can also be synthesized from carbon nanotubes (CNTs) by unzipping their multiple walls by plasma etching. CNTs have a longer length compared to their width and a one-dimensional geometry, as shown in Figure 2c. Synthesized GNRs have very smooth edges with a narrow width distribution of 10–20 nm.[23] One of the benefits of the sheet-like structure of carbon (GR) over the ball and nanotube is that it is exposed/available to attacking species and every carbon atom with sp^2 hybridization is chemically available.

The large surface area of a GR sheet allows π electrons to move freely over the geometry, give it good conductivity, and make it fully reactive. Usually, nanotubes can be opened into a GR sheet by applying a mixture of strong oxidizing agents such as H_2SO_4 and $KMnO_4$. This mixture pries open some of the carbon–carbon bonds, opens a crack in the hexagonal cells, and produces an extraordinarily long and thin conductive ribbon upon continuous chemical reactions. Another advantage is that it has a fine thin layer and a strength that is more than 200 times the tensile strength of steel.[24]

1.2. Structure and Properties of Graphene Derivatives

Although pure GR is chemically inert, due to the widely exposed delocalized π electrons on its surface, it can be easily opened via covalent chemistry, doping, GO, thiolate, fluoride, defects, nanoribbons, and edges.[25]

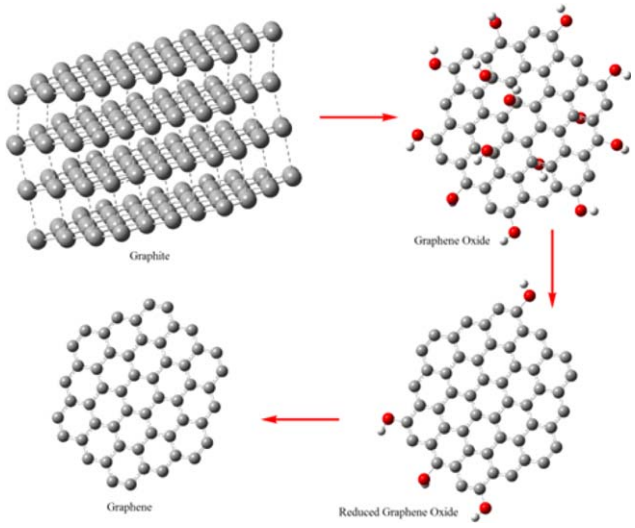

Fig. 3. Synthetic scheme of GO, rGO, and GR.

1.2.1. Graphene Oxide

Wide-bandgap derivatives of GR, such as GOs, are semiconductors that could replace silicon in electronics applications.[26] Commonly, GO can be synthesized through the exfoliation of GR sheets by chemical oxidation. These oxidizing agents, such as HNO_3, $KMnO_4$, H_2SO_4, and H_2O_2, modify the 2D structure of GR by attaching carboxylate, hydroxyl, and epoxide groups, to create the species commonly referred to as GO, as shown in Figure 3.[27]

GR is covalently attached with the oxygen-containing functional groups, either on the basal plane, middle, or at the edges of the thin film sheet.[28] Due to the attachment of these functional groups, GR (GO) is a potential and cost-effective candidate in the field of energy storage, sensors, optical devices, biomedical applications, field-effect transistors, clean energy devices, and sensors.[29] Because of these different oxidic functional groups, GO is extremely useful in improving the performance of photoelectrochemical solar cells. GO has the ability to adsorb organic molecules and thus enhances its local concentration near the photocatalyst.[29]

1.2.2. Reduced Graphene Oxide

GR in the fully oxidized state (GO) has numerous oxygen functional groups, which reduce its electrical conductivity and can be used as a conductance-based sensor. However, the chemical reduction using some reducing agents like hydrazine can restore the conductivity by several orders of magnitude by removing oxygen-containing functional groups, which restores the aromaticity of –C=C– double–single bonds. However, this process cannot repair the material to a pure GR sheet, as some of the oxygen groups remain present even after long exposure to hydrazine. Thus, rGO is both conductive and

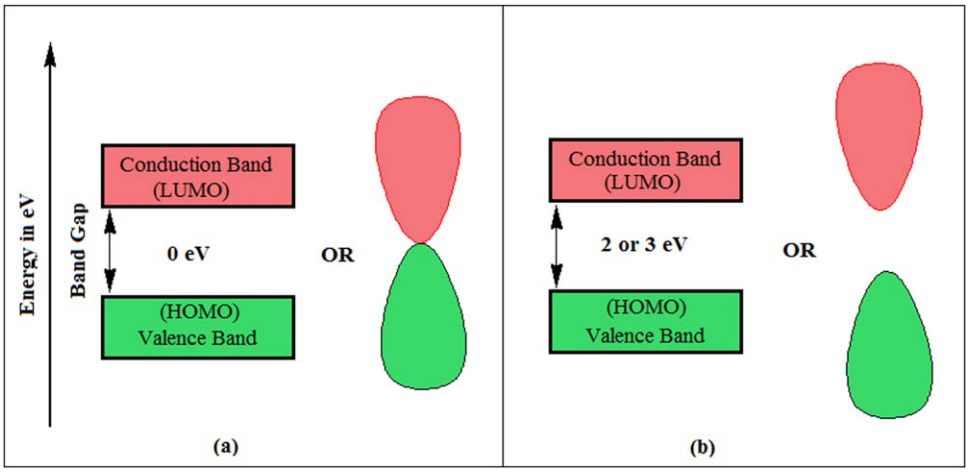

Fig. 4. Energy level diagram for the (a) unmodified GR and (b) modified GR.

chemically active (reactive sites), which makes it a promising candidate as an active material in the field of sensors. Essentially, when one of the GO sheets is subject to the chemical reduction process then a large-scale production of GR monolayers occurs with 2–3 times less conductivity and electron mobility compared to that of pure GR.[30] The reduction in conductivity is due to the lattice vacancies that cannot be restored during the reduction process, as shown in the typical example of an rGO in Figure 3.

1.3. Bandgap Engineering

Bandgap determination is a useful simulating tool for semiconductor materials that enables quantitative light absorption (UV–vis). Visible parts of the sunlight spectrum (380–800 nm wavelength) can be adequately captured by those materials with a threshold energy gap (bandgap of 2 to 3 eV); otherwise artificial bandgap engineering is required. GR and benzene have similarities, including characteristics like the –C=C– structure, sp^2 hybridization, and the bandgaps. GR has zero or near-to-zero bandgap, which results in semimetallic characteristics, while benzene possesses a wide HOMO–LUMO energy gap. The sp^2 carbon atoms of GR give rise to the valence (π) and conduction (π^*) bands, which are only accessible to touch at six points (Dirac points). So, the zero-bandgap or semimetallic nature of GR is due to these orthogonal π and π^* orbitals, which do not interact with each other.

The inherent zero bandgap limits the versatile applications of GR and results in a high leakage of current and power dissipation. Therefore, in order to compete with the classical silicon, GR needs bandgap modification/engineering. Different strategies have been reported in this regard, including composites with large-bandgap species (e.g., TiO_2), chemical modification, and photoinduced free radical reactions such as photochlorination, photocatalytic oxidation, and photomethylation.[31]

TiO_2 is an excellent photoactive compound but its large bandgap value lacks its unique characteristics in the pristine state. However, when TiO_2 is chemically mixed with GR or other delocalized π-conjugated systems, it results in the formation of an efficient photoelectrode.[32] In this process, GR acts as a sensitizer of TiO_2 by shifting the band edges and enlarging and reducing the bandgap (see Figure 4). Composites of GR and TiO_2 interchange their electron–hole between themselves, which finally led to the induction of visible-light photocatalytic activity.[33] Basically, when sunlight is illuminated on the surface of GR, it results in the production of OH radicals, which convert GR into an insulating GO. Prolonged illumination by UV light on the GR effectively converts the OH radicals into scissors and cuts the GR sheet into nanoribbons. These nanoribbons or nanomeshes are useful electroactive materials, which can be used to design many GR-based devices and circuits.

Chemical modification is an effective way to change the sp^2-hybridized orbitals of –C=C– per unit cell to sp^3-hybridized orbitals, which is a consequence of opening the zero bandgap. The opening of the bandgap starts from the covalent chemistry when two carbon atoms (per unit cell) are fully distinguished. The process is also like the benzene-related reaction that breaks the unsaturated carbon–carbon double bonds through free radical addition.[34]

In the photoinduced free radical reactions, irradiation with UV–vis light triggers the addition reaction of the chemically inert zero-bandgap GR. Moreover, this is an easy, cheap, clean, and attractive tool in terms of device fabrication.[35] Furthermore, in photochemical bandgap engineering, Li et al. have successfully developed a few reaction paths such as photochlorination, photocatalytic oxidation, and photomethylation.[31] The photochlorination concept originated from the Cl_2 addition reaction of benzene in the presence of light. Following this

reaction strategy, GR and Cl_2 interacted with each other in the presence of light, which resulted in high electrical conductivity because of adsorbed Cl radicals on the surface of GR. Photomethylation is also similar to photochlorination; after accumulation on the surface of GR these free radicals reacted (addition reaction) with the –C=C– bonds in GR in a short period of time. It was further found that this photochlorination reaction opens a gap between the π and π* orbitals, which makes GR a suitable candidate for electronic devices.[36] The –C=C– double bonds of GR can also be broken to open a gap between the HOMO and LUMO orbitals with the help of the Diels–Alder reaction. GR can act as both an electron acceptor and a donor because of its twofold degenerate orbitals, so if an electron acceptor species is in close proximity then it works as a donor.[37] Other methods of opening the bandgap of GR include doping it with n- or p-type materials and compression or stretching. In all of these processes the main feature is the conversion of sp^2 orbitals of the –C=C– double bond per unit to sp^3 (–C–C–), which causes the opening of frontier molecular orbitals of the chemically inert GR.[38]

2. Solar Energy Conversion Applications

The alarming problems of fossil fuel depletion, global warming, and environmental pollution have intensified the search for suitable photocatalysts to address these challenges.[16a] The conversion of sunlight into electrical energy has been considered as a state-of-the-art solution to the energy crisis. The high cost and high material utility of Si-based solar cells have triggered research in low-cost photovoltaics such as dye-sensitized solar cells (DSSCs), quantum-dot-sensitized solar cells (QDSSCs), organic solar cells, and perovskite solar cells.[39] Photocatalysis is also a solar energy conversion process that has the potential to convert photon energy into chemical energy (solar fuel) and be used in environmental purification.[40] Photocatalysis is considered to be green technology and is widely used for water splitting to generate H_2 as fuel, degradation of pollutants, selective organic transformations for the synthesis of fine chemicals, and other photoelectrochemical processes in both the gas and liquid phases.[41] The high electrical conductivity, transparency, excellent charge carrier mobility, and bandgap tunability of GR and its derivatives have made it an ideal material in the field of solar energy conversion and photocatalysis.[15a,42]

2.1. Photocatalytic Water Splitting

Hydrogen has long been identified as one of the most promising energy carriers. Solar-driven hydrogen generation (solar fuel), also known as solar water splitting, is believed to be the most promising means of large-scale H_2 production from renewable resources: water and sunlight.[43] One of the most convenient approaches is to use hydrogen production with an appropriate photocatalyst. Thus, many materials have been studied in order to find a potential photocatalyst for water splitting. Solar water splitting consists of three basic processes. The first process is the absorption of photons to generate electron–hole pairs. This is highly dependent on the band structure (position of the valence (VB) and conduction (CB) bands). The second process is the charge separation process, where the photoinduced electron–hole pair migrates to different sites of the photocatalyst before recombination. The third process is the surface chemical reactions, which include the reduction of water to generate H_2 and the oxidation of water to generate O_2 using a photogenerated electron and hole, respectively. Thus, for efficient photocatalytic water splitting, a suitable photocatalyst should have an appropriate band structure to harvest the maximum amount of the solar spectrum and appropriate band edge positions for spontaneous water splitting.

The hole diffusion length should allow the fast charge transfer to the respective reaction site and the photocatalyst should have fast reaction kinetics in order to split water and minimize the recombination. GR, GO, and rGO have been extensively studied in photocatalytic water splitting; however, the role that GR and its derivatives play in enhancing the photocatalytic performance is not clearly explored and needs further elucidation. Yu et al. have summarized the recent advances in graphene-based photocatalysts for solar-fuel production, including water splitting to H_2 and CO_2 reduction to hydrocarbon fuel.[46] Similarly, Putri et al. have reviewed the heteroatom-doped GR-based photocatalyst,[47] while Zhang et al. have discussed the challenges for future exploitation of GR-based photocatalysts in the hope of designing smarter and more efficient GR-based photocatalysts instead of joining the graphene "gold rush".[7]

A summary of photocatalysts based on GR and its derivatives for water splitting is given in Table 1. Yeh and co-workers demonstrated that under visible- or UV-light irradiation, graphite oxide acts as a photocatalyst for stable H_2 production when using a 20% methanol solution or pure water.[36] The CB edge of graphite oxide formed by the anti-bonding (π*) orbital has a higher energy level than the reduction potential of water to facilitate the spontaneous water splitting (Figure 5a). The four possible mechanisms enhancing the photocatalytic water splitting performances of GR and its derivatives are (i) suppressing the recombination of the photogenerated electron–hole pairs, (ii) acting as a support to provide adsorption and catalytic sites, (iii) tuning the bandgap size of the semiconductor and/or acting as a photosensitizer, (iv) and using a co-catalyst to catalyze the hydrogen evolution. Xiang et al. proposed the mechanism shown in Figure 5b for designing next-generation photocatalysts for solar water splitting.[45]

Table 1. GR-based photocatalysts for H_2 production by photocatalytic water splitting.

Photocatalyst	Synthesis method	Graphene content (wt %)	Reactant solution	Incident light source	H_2 evolution		Year/ref.
					Co-catalyst	Activity (μmol h^{-1})	
$YInO_3$/rGO	Solvothermal	0.5	CH_3OH/H_2O	UV–visible (Xe)	GR	400.4 μmol h^{-1} g^{-1}	2014[74]
$CaIn_2O_4$/rGO	Solvothermal	1	CH_3OH/H_2O	UV–visible (Xe)	rGO	62.5	2014[76]
$Ni(OH)_2$-CdS/rGO	Precipitation	1	Na_2S, Na_2SO_3	$\lambda > 420$ nm	$Ni(OH)_2$	4731 μmol h^{-1} g^{-1}	2014[81]
SiC/rGO	Solution mixing	1	KI	$\lambda \geq 420$ nm (Xe)	None	95 (μl/h)	2013[98]
$ZnIn_2S_4$/rGO	Solvothermal	5	Na_2S, Na_2SO_3	$\lambda > 420$ nm (Xe)	None	81.6	2013[99]
CTAB/TPPH-rGO	Solution mixing	2/3	TEOA	UV–visible (Xe)	Pt	2240	2013[100]
TiO_2/rGO	Hydrothermal	2	Na_2S, Na_2SO_3	UV–visible (Xe)	None	5.4	2012[54]
TiO_2/rGO	Solution mixing	0.7	Methanol	$\lambda > 320$ nm (Xe)	Pt	50	2012[57]
N-TiO_2/rGO	Hydrothermal	N/A	Methanol	UV (Hg), visible (Xe)	None	716 (UV), 112 (vis)	2012[90]
CdS/rGO	Two-phase	N/A	Methanol	~365 nm (Hg)	Pt	5500	2012[65]
CdS/rGO	Precipitation	5	Na_2S, Na_2SO_3	$\lambda \geq 420$ nm (Xe)	None	314	2012[63]
CdS/rGO	Hydrothermal	1	Na_2S, Na_2SO_3	$\lambda \geq 420$ nm (Xe)	None	70	2012[101]
$TiSi_2$/rGO	Precipitation	1	Pure water	$\lambda \geq 420$ nm (Xe)	RuO_2	97.5	2012[102]
RB-rGO	Solution mixing	N/A	TEOA	$\lambda \geq 420$ nm (TH)	Pt	14.2	2012[103]
EY/RB-rGO	In situ photoreduction	N/A	TEOA	$\lambda \geq 420$ nm (TH)	Pt	36.7	2012[104]
TPA-rGO	Solution mixing	N/A	KI	UV–visible (Xe)	Pt	2.3	2012[105]
Ru(dcbpy)$_3$-rGO	Solution mixing	N/A	EOA	UV–visible (Xe), visible (Xe)	Pt	2533 (UV), 118 (vis)	2012[106]
CdS@TaOH-rGO	Hydrothermal	1	Na_2S, Na_2SO_3	$\lambda > 420$ nm (Xe)	Pt	633	2012[83]
Cu_2O/rGO	In situ growth	3.8	Methanol	$\lambda > 400$ nm (Xe)	Pt	264.5	2012[107]
TiO_2/rGO	Hydrothermal	2.8	Methanol	UV–visible (Xe)	None	0.29	2012[108]
ZnCdS/rGO	Coprecipitation-hydrothermal	0.25	Na_2S, Na_2SO_3	UV–visible (Xe)	rGO	1824	2012[68]
CdS/rGO	Sol–gel	2	Na_2S, Na_2SO_3	$\lambda > 380$ nm (Xe)	rGO	~5	2012[109]
TiO_2/rGO	Hydrothermal	N/A	Methanol	UV–visible (Xe)	rGO	~55	2012[109]
CdS/Al_2O_3/rGO	Solid state	1	Na_2S, Na_2SO_3	Visible (TH)	rGO	350	2012[82]
CdS/ZnO/rGO	Solid state	1	Na_2S, Na_2SO_3	Visible (TH)	rGO	751	2012[82]
TiO_2/MoS_2/rGO	Hydrothermal	5	Ethanol	UV–visible (Xe)	MoS_2/rGO	165.3	2012[71]
EY-MoS_2/rGO	Solution mixing	N/A	TEOA	$\lambda \geq 420$ nm (Xe)	MoS_2/rGO	83.8	2012[110]
Cu/P25/rGO	Hydrothermal	2	Methanol	UV–visible (Hg)	Cu/rGO	1275	2012[111]
Ni/rGO	Wet chemical	97	Methanol	$\lambda \geq 420$ nm (Hg)	Ni	~70	2012[112]
NiO/rGO	Wet chemical	97	Methanol	$\lambda \geq 420$ nm (Hg)	NiO	~30	2012[112]
$[Ru(bipy)_3]^{2+}$/rGO	Solution mixing	N/A	Methanol	$\lambda = 532$ nm (laser)	None	3290	2012[113]
TiO_2/rGO	Hydrothermal	2	TEOA	$\lambda \geq 420$ nm (Xe)	Pt	380	2012[114]
TiO_2/rGO	Solution mixing	1	Methanol	$\lambda > 320$ nm (Xe)	rGO/Pt		2011[59]
TiO_2/rGO	Microwave-hydrothermal	1	Methanol	UV–visible (Xe)	rGO	736	2011[115]
Ru/$SrTiO_3$:Rh/rGO/$BiVO_4$	Photoreduction	5	H_2SO_4	$\lambda > 420$ nm (Xe)	Ru	11	2011[80]
EY-rGO	Solution mixing	50	TEOA	$\lambda > 320$ nm (Xe), $\lambda > 420$ nm (Xe)	None	3350 (UV–vis), 400 (vis)	2011[116]
$Sr_2Ta_2O_{7-x}N_x$/rGO	Photoreduction	5	Methanol	UV–visible (Xe)	Pt	293	2011[75]
EY-rGO		3/13	TEOA	$\lambda \geq 420$ nm (Xe)	Pt	10.17	2011[117]

Table 1. (*Continued*)

Photocatalyst	Synthesis method	Graphene content (wt %)	Reactant solution	Incident light source	H_2 evolution		Year/ref.
					Co-catalyst	Activity (μmol h^{-1})	
	In situ photoreduction						
CdS/N-rGO	Solution mixing	2	Na_2S, Na_2SO_3	$\lambda \geq 420$ nm (Xe)	N-rGO	210	2011[111]
C_3N_4/rGO	Impregnation-chemical reduction	1	Methanol	$\lambda > 400$ nm (Xe)	Pt	451	2011[118]
TiO_2/rGO	Hydrothermal	N/A	Na_2S, Na_2SO_3	UV (Xe)	None	20	2011[119]
TiO_2/rGO	Self-assembly	N/A	Methanol	UV–visible (Xe)	None	~16	2011[120]
P25/rGO	Hydrothermal	1/6	Methanol	UV–visible (Xe)	None	74	2011[56]
CdS/rGO	Solvothermal	1	Lactic acid	$\lambda > 420$ nm (Xe)	Pt	1120	2011[64]
TiO_2/rGO	Sol–gel	5	Na_2S, Na_2SO_3	UV–visible (Xe)	None	8.6	2010[52]
rGO	Hummers	100	Methanol	UV–visible (Hg)	None	2833	2010[121]
TiO_2/rGO	Sol–gel	N/A	Na_2S, Na_2SO_3	UV–visible (Xe)	None	8.6	2009[122]

2.1.1. GR–TiO_2-Based Photocatalytic Water Splitting

Since the pioneering work of Fujishima and Honda,[48] TiO_2 has been extensively studied as a potential semiconductor for water splitting and degradation of environmental pollutants. The band edge positions of TiO_2 are suitable for spontaneous water splitting and TiO_2 is a cheap, abundant, chemically stable, and non-toxic material.[15a] However, due to its wide bandgap (3.2 eV) it can only absorb UV light and also suffers from severe charge recombination.[49] Many attempts have been made to improve this, including the loading of noble metals such as Pt, Pd, Ru, or Rh as co-catalyst onto the surface of TiO_2 to improve the charge separation and surface redox reaction. This enhances the efficiency of water splitting. However, the high cost of these metals limits the practical application of TiO_2 as a photocatalyst.[50] The recent discovery of GR nanosheet, a metal-free co-catalyst,[51] and GO–rGO as electron acceptors and transporters have resulted in significant improvements in the photocatalytic water splitting activities of GR–TiO_2-based materials.[52]

Along with other reasons, there are three fundamental aspects that make GR–TiO_2 materials excellent candidates for water splitting. The first benefit is that they enhance the separation of photoinduced electrons and holes because GR and its derivatives have high charge mobility properties. The second aspect is that they have an increased absorption range because of Ti–O–C bonds and nanosized Schottky interfaces, which act as a sensitizer (by directly capturing visible light). Finally, nanosheet GR and its derivatives act as metal-free co-catalysts to enhance the surface redox reaction by minimizing the surface recombination.[36] The GO–rGO has been extensively studied for water splitting applications. The GO–TiO_2 composite creates a p–n junction, which considerably improves the separation of photogenerated charges. The electrons quickly shifted from the CB of TiO_2 into the GO–rGO systems as the GO–rGO redox, with lower potential than the CB of TiO_2. The GR sheet not only increased the charge transfer, but also effectively reduced protons to generate H_2 (Figure 6).[53]

It is important to understand that the improvement in the photocatalytic activity of GR–TiO_2 composites is highly dependent on the synthetic method, uniform distribution, GR content, and degree of oxidation of GR to GO and reduction to rGO. In other words, the photocatalytic activity of GR–TiO_2 composite materials is dependent on the electron acceptor and transport, interfacial interaction, and the contact area of TiO_2 and GR. For example, the dependence of catalytic activity on electron acceptors and transporters has been studied by varying GR content; Zhang et al. studied the photocatalytic performance of rGO–TiO_2 photocatalysts by varying the rGO content from 0 to 10%.[52,54] The amount of hydrogen generation increased with the increase in rGO content and attained a maximum rate at 5% rGO content in the sol–gel prepared rGO–TiO_2 composite. The decrease in the H_2 generation rate with further increase in rGO content is attributed to the formation of recombination centers. The group of Zhang et al. also obtained similar results for hydrothermally prepared rGO–TiO_2 composites and they strongly believe that the improvement was due to the electron acceptor and fast transport properties of the composite.[52]

Similarly, Zhang et al. evaluated the H_2 evolution photocatalytic activity of GR–TiO_2 composites using aqueous Na_2S and Na_2SO_3 as sacrificial agents under UV–vis

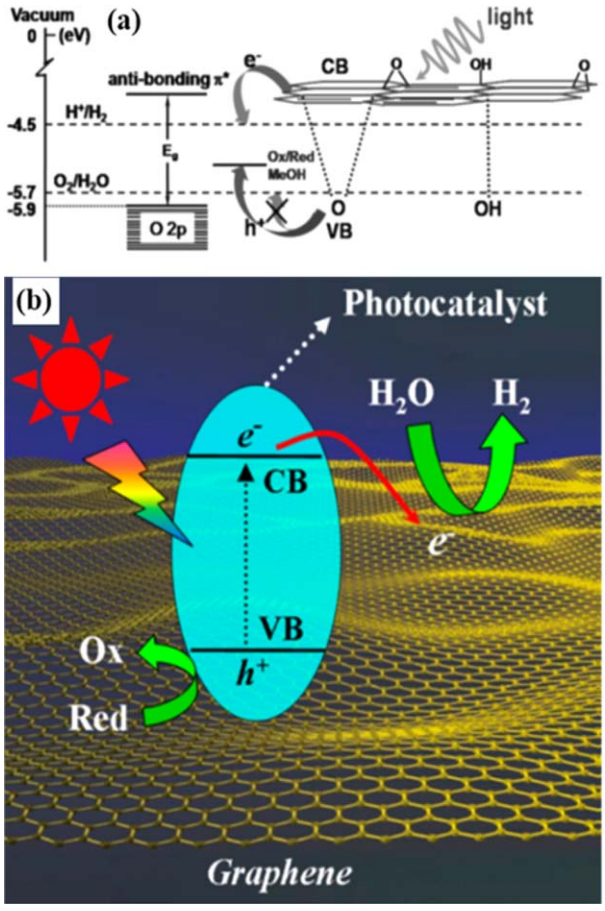

Fig. 5. (a) Schematic energy level diagram of GO relative to the levels of H_2 and O_2 generated from water. Reprinted with permission from reference [44]. (b) The proposed mechanism for GR-based photocatalysts in enhancing photocatalytic performance. Reprinted with permission from reference [45]. Copyright 2014 American Chemical Society.

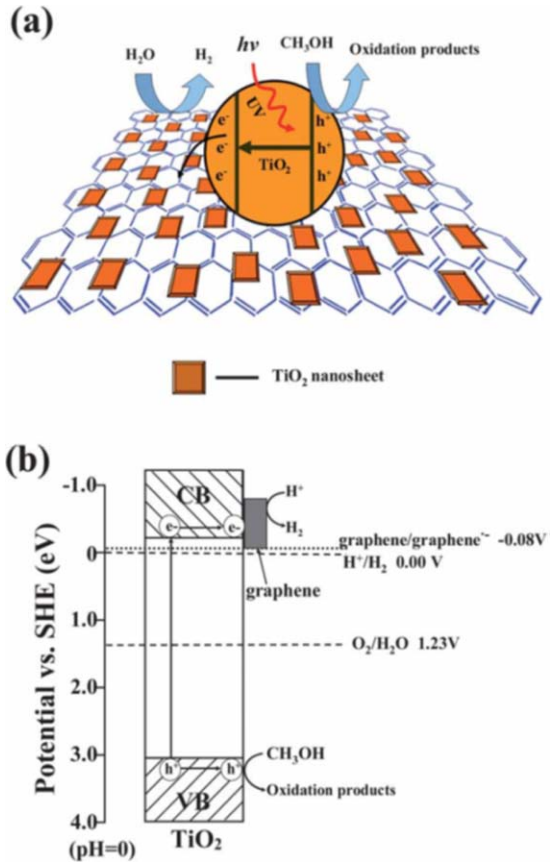

Fig. 6. (a) Schematic illustration of the charge transfer and separation in the GR-modified TiO_2 nanosheet system under UV-light irradiation. (b) Proposed mechanism for photocatalytic H_2 production under UV-light irradiation.[53] Copyright 2014 Royal Society of Chemistry.

illumination.[52] They determined that the photocatalytic activity of the composite depends upon the GR content and calcination atmosphere. They also observed an increase in the rate of H_2 evolution with the increase in GR content to 5 wt %, where the rate of H_2 evolution reached 8.6 μmol h^{-1}, which is 1.9 times higher than that of P25. Lin et al. also found that the calcination atmosphere affected the photocatalytic activity of the composites, and TiO_2–GR composites calcined in a nitrogen atmosphere showed a higher photocatalytic performance than those calcined in air due to the formation of oxygen vacancies in the TiO_2 lattice, which act as electron traps.[55]

The interfacial interaction has a pronounced effect on the charge mobility within the photocatalyst and the interfacial interaction between GR and TiO_2 is highly dependent on the synthetic method; therefore, a rational design for the synthesis of GR–TiO_2 composites is required to enhance the photocatalytic performance. Fan et al. compared H_2 evolution efficiency using methanol as a sacrificial agent with a range of GR–P25 composites synthesized through different methods such as UV-assisted photocatalytic reduction, hydrazine reduction, and the hydrothermal method. All the GR–P25 composites exhibited significantly improved H_2 evolution performance compared to P25 alone. Fan's group also compared the hydrogen evolution activity of P25, P25–CNT, and rGO–P25 with different mass ratios.[56] The rate of hydrogen evolution was higher in rGO–P25 synthesized by the hydrothermal method compared with rGO–P25 composites synthesized by other methods, as well as the P25–CNT composite. The TEM images showed that the composites were composed of GR sheets and 20–30 nm P25 nanoparticles. However, the contact between the P25 and rGO sheet was different for the composites prepared by different methods. The composites prepared by hydrothermal methods showed a uniform and more dispersed distribution of P25 nanoparticles as compared to the segregation of P25 nanoparticles on rGO sheets prepared by

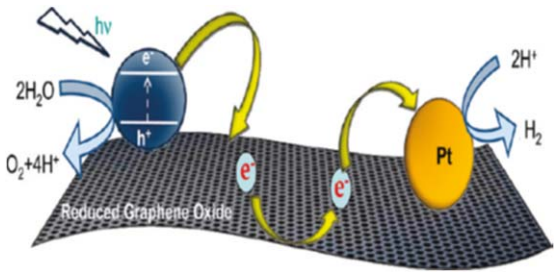

Fig. 7. Schematic illustration of selective oxidation and reduction processes on a single GR sheet at two different catalytic sites. Reprinted with permission from reference [60]. Copyright 2014 American Chemical Society.

other methods. The authors proposed that the hydrothermal method resulted in stronger interactions and uniformly distributed P25 nanoparticles on the rGO sheet, which accelerated the photogenerated electrons of P25 to rGO, suppressed the recombination of charge carriers, and resulted in higher photocatalytic activity.[56]

Attempts have been made to prepare GR–TiO_2 composites with uniform distribution and stronger interfacial interactions between the TiO_2 nanoparticles and the GR sheet. Among the different fabrication strategies, the hydrothermal, solvothermal, solution mixing, and sol–gel methods are believed to be the best for fabrication of GR–TiO_2 composites.[36] Although there has been a significant improvement in the synthetic strategies, the 2D GR sheets can only contact the bottom part of the TiO_2 nanoparticles, which limits the electron transport from TiO_2 to GR. The contact area between the TiO_2 nanoparticles and GR has been improved by the core–shell approach of the Choi group.[36] The core–shell nanocomposite was prepared in a two-step process involving the preparation of TiO_2 self-assembled GR nanosheets in the first step followed by photocatalytic reduction under UV irradiation in the second step to obtain an rGO–TiO_2 core–shell structure. The Choi group observed that the rates of H_2 production were higher in the rGO–TiO_2 core–shell structure as compared to the rGO–TiO_2 2D sheet structure, which indicates that the presence of rGO shells on the surface of TiO_2 facilitates the interfacial electron transfer. The direct contact between rGO and TiO_2 is maximized in a core–shell structure by retarding the charge recombination and accelerating the electron transfer. The geometry of the core–shell structure should be effective in the design of a GR–TiO_2 composite for solar conversion applications.[57]

The increased photocatalytic water splitting activity of Pt-loaded TiO_2 in the presence of sacrificial reagents (electron donors or hole scavengers) is well known and has been extensively studied.[58] Recently, Park et al. compared the hydrogen generation performance of three composite catalysts, Pt/TiO_2, GO/TiO_2, and GO/Pt/TiO_2, under UV-light irradiation.[59] They observed that the rate of H_2 evolution decreased in the order of GO/Pt/TiO_2>Pt/TiO_2>GO/TiO_2, indicating that TiO_2 alone with GO is not catalytically active in the production of H_2. However, the presence of GO and Pt on the TiO_2 surface can synergistically enhance the H_2 generation activity when GO serves as an auxiliary co-catalyst, reducing the cost of photocatalyst preparation by consuming less Pt. Kamat has proposed a possible mechanism of water splitting by incorporating semiconductor nanoparticles (e.g., TiO_2) and Pt nanoparticles in a GR sheet. The role of the GR sheet in this mechanism is to capture electrons and shuttle them across the 2D carbon network to the Pt site to facilitate hydrogen reduction (Figure 7).[60] Wang et al. have developed an efficient GR–TiO_2–Au photocatalyst by combining the surface plasmon resonance effect of Au NPs, which broadens the visible-light response of the TiO_2, and the excellent electron transport properties of graphene, which hinders the fast recombination of photoelectron and hole pairs. Their results showed that the composite photocatalyst has significantly increased visible-light absorption and enhanced photocatalytic H_2 production compared with pure TiO_2, graphene–TiO_2, and Au–TiO_2 composites.[61]

2.1.2. Graphene–Metal Sulfide Composites for Photocatalytic Water Splitting

Metal sulfides, especially CdS, are some of the most attractive visible-light-driven water splitting photocatalysts due to their ideal band structure. However, CdS suffers from high levels of photocorrosion and its photocatalytic activity is limited by the high recombination rate of the photoinduced electron–hole pairs. Time-resolved fluorescence spectroscopic studies have shown a picosecond ultrafast electron transfer process from photoexcited CdS to the GR sheets in GR–CdS composites.[62] The fast electron transfer to the GR sheet demonstrates that GR could reduce the recombination rate of the photoinduced electron–hole pairs in CdS photocatalysts because of its high electron acceptor and transporter properties. Peng et al. have reported higher photocatalytic activity for a series of GO–CdS nanocomposites fabricated using a facile precipitation process by using $Cd(Ac)_2$ and Na_2S on a prefabricated GO using Na_2S/Na_2SO_3 as a sacrificial reagent. They claimed that GO acts as a CdS supporting matrix, co-catalyst, and electron acceptor for effective charge separation in the GO–CdS nanocomposite; therefore, it provides an inexpensive means to achieve high-performance visible-light-driven photocatalysts for hydrogen production without noble-metal loading.[63] Li et al. have synthesized rGO–CdS nanocomposites by a solvothermal method using $Cd(Ac)_2{\cdot}2H_2O$, DMSO, and GO as precursors to achieve deposition of CdS on rGO simultaneously, and found that the nanocomposites with 1.0 wt % content of rGO and 0.5 wt % Pt showed a higher H_2

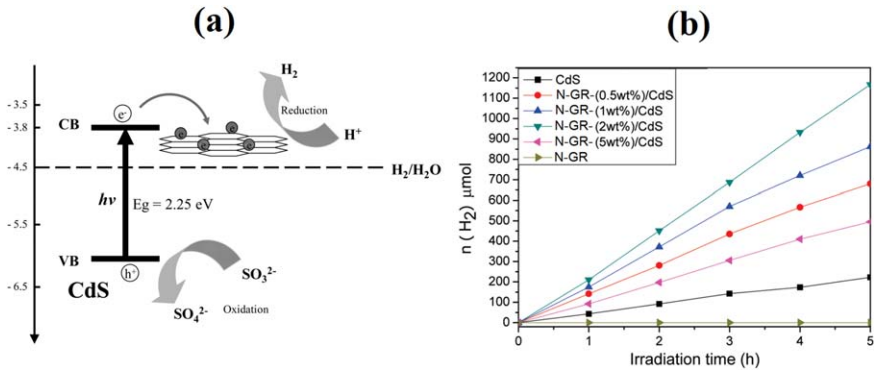

Fig. 8. (a) Energy level diagram for N-GR–CdS nanocomposites in relation to the redox potentials for the water splitting process in Na_2S/Na_2SO_3 aqueous solution. (b) H_2 evolution of CdS and N-GR–CdS composites with various contents of N-GR. Measurement conditions: 0.2 g sample, 300 mL aqueous solution containing 0.1 M Na_2S and 0.1 M Na_2SO_3. Light source: 300 W Xe lamp (λ_g 420 nm). Reprinted with permission from reference [66]. Copyright 2014 American Chemical Society.

production rate of 1.12 mmol h^{-1} under visible-light irradiation using lactic acid as a sacrificial reagent.[64] Similarly, Gao et al. have proved the role of the electron acceptor and transport characteristics of rGO for enhancing photocatalytic water splitting properties in the rGO–CdS nanocomposite.[65] Li et al. prepared a series of highly durable N-doped GR–CdS nanocomposites for hydrogen production from water under visible-light irradiation at $\lambda \geq 420$ nm and showed that N-GR–CdS nanocomposites have higher photocatalytic activity than pure CdS. The enhanced transient photocurrent response proved an effective transfer of photoinduced electrons from CdS to N-doped GR, which results in higher photocatalytic performance due to suppressed recombination of the electron–hole pairs. The amount of N-GR is an important factor that affects the photocatalytic activity of N-GR–CdS nanocomposites; 2 wt % of N-GR was optimal for the highest photoactivity. Furthermore, the N-GR–CdS photocatalyst showed a constant rate of H_2 evolution for more than 30 h without degradation, indicating that N-GR forms a protective layer to prevent photocorrosion of CdS under light irradiation.[66] Figure 8 shows the energy level diagram and electron transfer mechanism of N-GR–CdS nanocomposites in the Na_2S/Na_2SO_3 aqueous solution. Similarly, Liu et al. have constructed one-dimensional silver-nanowire-doped reduced graphene oxide (NW-rGO) integrated with CdS nanowire network hybrid structures for artificial photosynthesis, which resulted in a prolonged lifetime of the photogenerated charge carriers excited from the CdS NW network, thus making Ag NW-rGO an efficient co-catalyst with the CdS NW network toward artificial photosynthesis.[67]

Zhang et al. have reported a noble-metal-free rGO–$Zn_{0.8}Cd_{0.2}S$ nanocomposite as an efficient solar photocatalytic system for H_2 production from water splitting.[68] The rGO–$Zn_{0.8}Cd_{0.2}S$ composite showed a 450% higher H_2 production performance compared to pristine $Zn_{0.8}Cd_{0.2}S$ and an optimized Pt–$Zn_{0.8}Cd_{0.2}S$ system. Figure 8a shows the mechanism of electron injection from $Zn_{0.8}Cd_{0.2}S$ to rGO while Figure 8b shows the respective band edge positions and redox reaction centers. The rGO–$Zn_{0.8}Cd_{0.2}S$ composite GO functions as an electron collector and transporter to enhance the lifetime of the charge carriers; additionally, it also facilitates the photocatalytic reaction to take place on the surface. This work created a green and simple way for using rGO as a support for the $Zn_xCd_{1-x}S$ photocatalyst, but also demonstrated that rGO is a promising substitute for noble metals in photocatalytic H_2 production.[68,69] Similarly, Li et al. also prepared a GR–$Zn_xCd_{1-x}S$ composite photocatalyst that showed higher H_2 evolution without the use of a noble-metal co-catalyst. Their work revealed the significance of the choice of organic or inorganic S source in the design and fabrication of GR-based sulfide photocatalysts.[70]

More recently, Xiang et al. developed a new noble-metal-free ternary composite material by growing TiO_2 nanocrystals in the presence of a layered MoS_2–GR (MG) hybrid using a simple two-step hydrothermal process.[71] The TiO_2–MoS_2–GR composite reached a high H_2 production rate of 165.3 μmol h^{-1} and the apparent quantum efficiency reached 9.7% at 365 nm, when the content of the MoS_2–GR co-catalyst was 0.5 wt %, while the co-catalyst itself contained 5.0 wt % content of GR. The high photocatalytic activity of this ternary composite was due to the positive synergetic effect between the MoS_2 and GR components, which not only acted as an electron collector but also as an active adsorption site, respectively. Xiang et al. have also prepared a GR–CdS–MoS_2 composite with homogeneous dispersion of MoS_2 nanoparticles by a photodeposition method without the characteristic stacked layer structure of MoS_2.[72] This GR–CdS–MoS_2 composite exhibited a much higher activity toward photocatalytic water splitting under visible-light irradiation compared with the hydrothermally synthesized GR–CdS–MoS_2 composite with

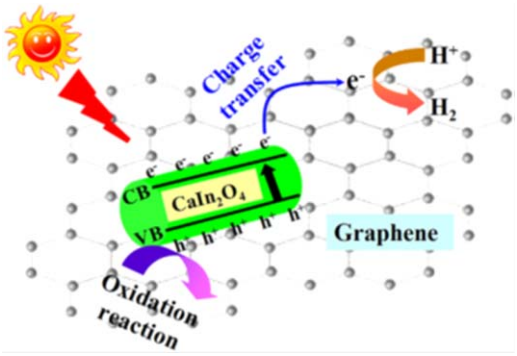

Fig. 9. Schematic illustration of the charge separation and transportation over rGO–$CaIn_2O_4$ composites under visible-light irradiation. Reprinted with permission from reference [76]. Copyright 2014 *Int. J. Hydrogen Energy.*

the characteristic MoS_2 layer structure. The improved activity and homogeneous dispersion of tiny MoS_2 for GR–CdS–MoS_2 was attributed to better separation and transfer of charge carriers and provided the increased number of catalytically active sites. The composite also had a higher stability towards photocorrosion.[72] The study by Xiang et al. demonstrated an inexpensive photocatalyst with high solar H_2 evolution without noble metals.[71,72] Similarly, Yu and co-worker fabricated noble-metal-free GR–CdS–MoS_2 hollow spheres with superior photocatalytic activity due to the large surface area of the hollow structure, minimum charge recombination, and better synergetic electron transfer within the photocatalyst composite.[73]

2.1.3. Graphene-Based Single Oxide Composites for Photocatalytic Water Splitting

Recently, Gao and co-workers have fabricated a series of rGO–$CaIn_2O_4$ composites via a facile solvothermal method by depositing $CaIn_2O_4$ nanoparticles on the GR sheets to simultaneously enhance the photocatalytic performance of $CaIn_2O_4$. The rGO–$CaIn_2O_4$ composite evolved H_2 at a rate of 62.5 mmol h^{-1} using methanol as a sacrificial agent when the content of GR was 1 wt %. Furthermore, the composite was very highly stable and did not show deactivation for H_2 evolution for over 32 h. The tentatively proposed mechanism (Figure 9) proves that GR acts as an efficient electron acceptor and transporter, as well as a co-catalyst for the reduction of H_2 to produce hydrogen.[36] Similarly, Ding and co-workers also prepared a new rGO–$YInO_3$ composite by the solvothermal method, which showed a remarkable H_2 evolution rate of 400.4 μmol h^{-1} g^{-1} when the content of GR was 0.5 wt %, which is 127 and 3.7 times higher than that of pure $YInO_3$ and Pt–$YInO_3$, respectively. The study showed that the addition of GR as a co-catalyst can narrow the bandgap of $YInO_3$ to visible photon energy and prolong the separation and lifetime of electron–hole pairs by the chemical bonding between $YInO_3$ and GR.[74] Mukherji et al. studied a new type of nitrogen-doped tantalite, $Sr_2Ta_2O_{7-x}N_x$, which exhibited significantly increased visible-light absorption and improved photocatalytic hydrogen production by 87% under solar irradiation, compared with its undoped counterpart $Sr_2Ta_2O_7$. An additional 80% in efficiency improvement was recorded by making a composite with GR–Pt to provide an overall quantum efficiency of 6.45%. The study attributed the increase in efficiency to a better charge carrier separation on the photocatalyst.[75]

2.1.4. Graphene as Redox Mediator in Z-Scheme/ Heterojunction Water Splitting Photocatalysts

Although a number of GR-based single-photocatalyst systems have been developed for effective water splitting, they have very low efficiency for practical applications. By mimicking natural photosynthesis, the Z-scheme/heterojunction photocatalysis system, consisting of a H_2 evolution photocatalyst, an O_2 evolution photocatalyst, and an electron mediator, has great potential to improve the water splitting efficiency under visible light.[77] Recent studies show that the electron transfer between the two photocatalysts is the rate-determining process in Z-scheme or heterojunction systems.[78] Substantial research has been done on ionic redox shuttles to improve the electron transport from the O_2 to the H_2 photocatalyst.[79] Compared to the ionic redox couples, a solid mediator is more favorable in terms of reclamation of clean water and recovery of the photocatalyst. Considering the excellent electron separation and transport ability of GR, it is promising in making a contribution to improve the hydrogen evolution efficiency of many single photocatalysts. The Iwase group has constructed a series of Z-scheme systems by mixing photoreduced rGO with $BiVO_4$ (rGO–$BiVO_4$) and Ru–$SrTiO_3$:Rh (rGO–Ru–$SrTiO_3$:Rh). As shown in Figure 10, the rGO functions as a solid-state electron mediator, transferring the electrons from the conduction band of $BiVO_4$ to the vacancies in the impurity levels of Ru–$SrTiO_3$:Rh to reduce water to H_2 on the Ru co-catalyst, while the holes in $BiVO_4$ oxidize water to O_2. The rGO–$BiVO_4$ and Ru–$SrTiO_3$:Rh systems show the highest H_2 evolution rate and are stable over a period of 24 hours. This important work has paved the way for the use of GR in the design of efficient photocatalysts for water splitting.[80]

Since the studies have proven that the built-in electric field at the interface between different semiconductors can promote the separation and transport of photoinduced electron–hole pairs, there has been great interest in the development of heterojunction photocatalysts. Recently, combining GR with heterojunction nanostructures to enhance the H_2 evolution efficiency of heterojunction photocatalysts has been on the rise due to the better electron acceptor and transporter functions of GR. Yan et al. have synthesized a series of nickel hydroxide modified cadmium sulfide–rGO ($Ni(OH)_2$-CdS–rGO) nanocomposites and

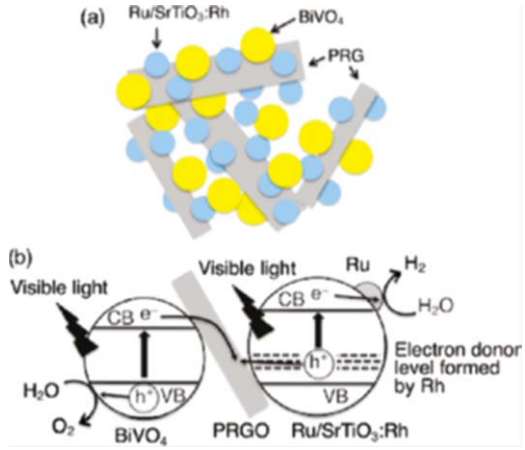

Fig. 10. (a) Schematic image of a suspension of Ru–$SrTiO_3$ and rGO–$BiVO_4$ in water at pH 3.5. (b) Mechanism of water splitting in a Z-scheme photocatalysis system consisting of Ru–$SrTiO_3$:Rh and rGO–$BiVO_4$ under visible-light irradiation. Reprinted with permission from reference [80]. Copyright 2014 American Chemical Society.

demonstrated that the heterojunction material is an efficient photocatalyst for water splitting. The $Ni(OH)_2$-CdS–rGO materials with 1.0 wt % $Ni(OH)_2$ loading produced hydrogen from water under visible-light irradiation (λ>420 nm) at a rate of 4731 μmol h^{-1} g^{-1}, which is nearly ten times higher than that of the CdS–rGO photocatalyst under the same conditions. The study proved that $Ni(OH)_2$ is a good noble-metal-free co-catalyst for water splitting and that the positive synergetic effect between CdS, rGO, and $Ni(OH)_2$ can efficiently suppress charge recombination by improved interfacial charge transfer and photocatalytic H_2 evolution by providing active sites.[81] Khan et al. also demonstrated the superior electron collector and transporter nature of GR by preparing GO–CdS–oxide (oxide: ZnO, Al_2O_3) photocatalysts in a single-step hydrothermal process. The GO–CdS–Al_2O_3 and GO–CdS–ZnO both exhibited enhanced photocatalytic activity for hydrogen generation with apparent quantum yields (AQYs) of 14% and 30%, respectively. The superior photocatalytic properties are attributed to the sheet-like structure of GO, which provides enhanced surface area and effective separation of photoinduced charge carriers.[82]

In another study, Hou et al. prepared CdS@TaON core–shell nanocomposites by an ion-exchange route with assistance from a hydrothermal process on GO as the support. The CdS@TaON core–shell heterojunction decorated GO nanosheets proved to be an efficient water splitting photocatalyst, with a H_2 production rate of 306 μmol h^{-1} and an apparent quantum efficiency (QE) of 15% under 420 nm monochromatic light when coupled with 1 wt % of GO and 0.4 wt % of Pt, which was about 141 times higher than that of the pristine TaON. The high water splitting performance of heterojunction photocatalysts was attributed firstly to the presence of

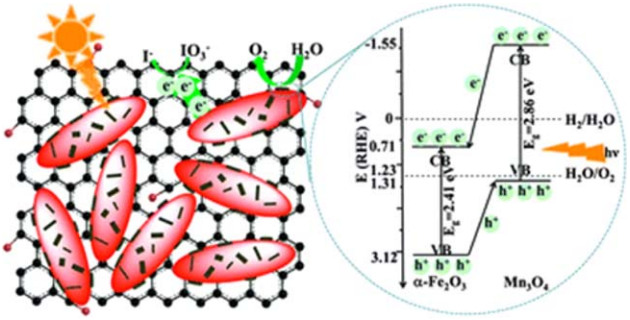

Fig. 11. Schematic mechanism of oxygen evolution from the α-Fe_2O_3/Mn_3O_4-1/rGO-3 photocatalyst. Reprinted with permission from reference [84]. Copyright 2014 Royal Society of Chemistry.

CdS nanocrystals, which modify the band structure in the coupled semiconductor system, and secondly to the involvement of GO, which serves as an electron collector and transporter to efficiently lengthen the lifetime of the photogenerated charge carriers from CdS@TaON composites.[83]

Most of the work discussed above focused on the development of efficient H_2 evolution photocatalysts using GR and its derivatives, but very recently Yin et al. have developed a novel O_2 evolution photocatalyst consisting of α-Fe_2O_3, Mn_3O_4, and rGO nanocomposites.[84] The α-Fe_2O_3–Mn_3O_4–rGO nanocomposite has been facilely synthesized through a two-step solvothermal process. The optimized photocatalyst showed an oxygen evolution rate of 1406.2 μmol g^{-1} under UV–vis light irradiation and the quantum yield was ca. 4.35% at 365 nm. The high photocatalytic oxygen evolution activity of the heterostructural α-Fe_2O_3–Mn_3O_4–rGO nanocomposite is attributed to its high light-harvesting efficiency, a lowered overpotential for water oxidation, and excellent charge transfer performance (Figure 11). This study highlights the potential application of GR in the design of heterostructured photocatalysts for O_2 evolution.[84] Similarly, Hou et al. have prepared a GR-supported Ag_3PO_4–Ag–AgBr photocatalyst for O_2 evolution by a photoassisted deposition–precipitation reaction, followed by a hydrothermal treatment. The hybrid rGO–Ag_3PO_4–Ag–AgBr composite exhibits double the O_2 production activity than that of bare Ag_3PO_4 under visible-light irradiation. The increase in activity is attributed to a combination of conduction band depletion, lowered valence band of Ag_3PO_4 by the addition of Ag/AgBr and rGO, and better charge transfer and distribution onto the GR support.[85]

2.2. Photoelectrochemical Water Splitting

As described above, photocatalytic H_2 generation is carried out using a suspension system of particulate semiconductor photocatalysts, while PEC water splitting is based on thin-film electrodes and carried out in a PEC cell under light irradiation. PEC cells consist of a photoanode/working electrode (PA) for

Table 2. GR-based photoelectrodes for photoelectrochemical H_2 production by water splitting.

Photoelectrodes	Preparation method	Electrolyte	Light source	Bias (V)	Year/ref.
Cu_2O/GR	–	–	AM 1.5	0 (vs RHE)	2014[93]
$BiVO_4$/rGO	Hydrothermal	–	AM 1.5G (Xe)	0.5 (vs Ag/AgCl)	2013[88]
α-Fe_2O_3/rGO	Electrodeposition	NaOH	AM 1.5G (Xe)	0.5 (vs Ag/AgCl)	2013[89]
Si/rGO	Spin coating	H_2SO_4, K_2SO_4	UV–visible (Xe)	−0.754 (vs MSE)	2013[35]
ZnO/rGO	Electrophoresis	Na_2SO_4	AM 1.5G (Xe)	0.4 (vs Pt)	2012[123]
α-Fe_2O_3/rGO/$BiV_{1-x}Mo_xO_4$	Spin coating	Na_2SO_4	AM 1.5G (Xe)	−0.04 (vs Ag/AgCl)	2012[91]
α-Fe_2O_3/CNT-rGO	Spray coating	NaOH	AM 1.5G (Xe)	1.23 (vs Ag/AgCl)	2012[124]
TiO_2/rGO	Assembly	Na_2SO_4	$\lambda > 420$ nm (Xe)	0 (vs Ag/AgCl)	2012[125]
$BiVO_4$/rGO	Drop casting	Na_2SO_4	$\lambda \geq 420$ nm (Xe)	0.75 (vs Ag/AgCl)	2010[126]

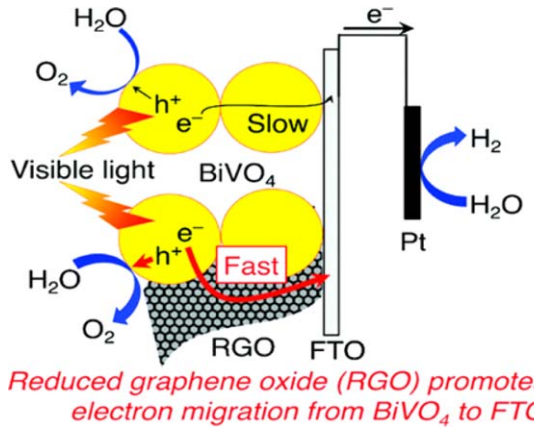

Fig. 12. Electron transport in a PEC system based on rGO and $BiVO_4$. Reprinted with permission from reference [87]. Copyright 2014 American Chemical Society.

O_2 evolution, a photocathode/counter electrode for H_2 evolution (mostly Pt is used as a counter electrode due to the lack of suitable photocathode materials), and an electrolyte solution. Both electrodes are connected together through a wire, completing the current loop between the photoelectrodes. Similar to the particulate photocatalysts, the photoelectrode materials should fulfill the fundamental requirements of band structure for spontaneous water splitting. The number of reliable and stable materials capable of spontaneous water splitting, without external bias, is limited due to the stringent band structure requirements. Following the pioneering work of Kay and coworkers on α-Fe_2O_3,[86] PEC received much more scientific attention due to its potential advantages over photocatalytic water splitting. Due to the excellent electron acceptor and transporter properties, GR and its derivatives are at the forefront to improve the PEC performance of photoanode and photocathode materials. A summary of GR-based photoelectrodes (photoanode and photocathode) for PEC water splitting is given in Table 2.

2.2.1. Graphene-Based Photoanodes for PEC Water Splitting

Ng et al. demonstrated for the first time that GR could improve the PEC performance of a $BiVO_4$ photoanode by synthesizing rGO–$BiVO_4$ composites using the spin-coating technique. Under visible-light irradiation, rGO–$BiVO_4$ composites showed H_2 and O_2 evolution rates of 0.75 and 0.21 μmol h^{-1}, with an external bias of 0.8 V, while negligible gas evolution was observed on pure $BiVO_4$. The PEC water splitting performance is ascribed to the scaffold roll of rGO, which improved contact between the $BiVO_4$ particles and the transparent conducting electrode, as well as to the longer electron lifetime of excited $BiVO_4$. This is because the electrons are injected into rGO instantly at the site of generation, leading to a minimized charge recombination as shown in Figure 12.[87] This work has triggered more interest in synthetic strategies to develop rGO–$BiVO_4$ composites with better PEC performance.[88]

Zhang et al. have reported the PEC performance of the well-studied α-Fe_2O_3 photoanode by inserting a GR interlayer using the template-assisted electrodeposition method.[89] The incorporation of the GR interlayer remarkably improved the photocurrent density and incident photon-to-electron conversion efficiency (IPCE) of rGO–α-Fe_2O_3 compared to that of an α-Fe_2O_3 PA. This increase in the PEC performance indicates that the GR interlayer acts as both an electron transfer layer and an electrolyte blocking barrier, by which it can not only reduce the charge recombination at the substrate–electrolyte interface but also improve the electron transfer from α-Fe_2O_3 to the substrate. They concluded that GR can provide solutions to the fast charge recombination in α-Fe_2O_3 PAs and to the high charge transfer resistance of the photoelectrode–electrolyte interface in PEC cells.[89] Wu et al. fabricated an rGO–WO_3 hybrid nanocomposite PA on fluorine-doped tin oxide (FTO) substrates via hydrothermal growth of ultrathin WO_3 nanoplates followed by in situ photoreduction to deposit rGO layers on the WO_3 nanoplate surfaces. The rGO–WO_3 nanocomposites have achieved the highest photocurrent density of 2.0 mA cm^{-2} at 1.23 V versus the reversible hydrogen

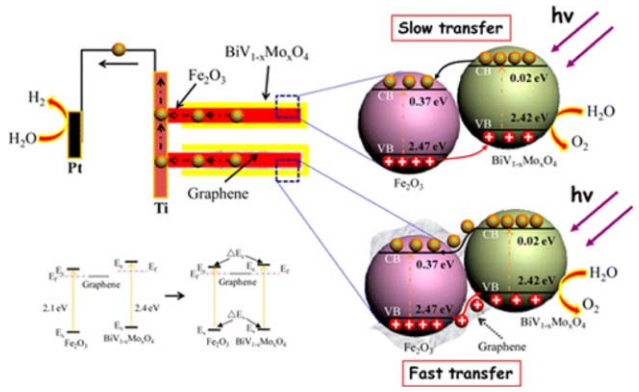

Fig. 13. Schematic of the energy band structure of the α-Fe_2O_3–rGO–$BiV_{1-x}Mo_xO_4$ heterojunction and proposed mechanism of PEC water splitting. Reprinted with permission from reference [91]. Copyright 2014 American Chemical Society.

electrode (RHE) in electrochemical impedance spectroscopy (EIS) measurements, which proved that the increased PEC performance is due to the enhanced charge transfer by the incorporation of rGO.[90]

In another work, Hou et al. prepared heterojunction core–shell arrays of α-Fe_2O_3–rGO–$BiV_{1-x}Mo_xO_4$, which consisted of an α-Fe_2O_3 nanorod as the core, rGO as the interlayer, and $BiV_{1-x}Mo_xO_4$ as the shell. The core–shell array was fabricated by hydrothermal deposition of α-Fe_2O_3 nanorods onto a Ti substrate, followed by the deposition of the rGO interlayer and a $BiV_{1-x}Mo_xO_4$ shell using photoreduction and spin coating, respectively. The α-Fe_2O_3–rGO–$BiV_{1-x}Mo_xO_4$ heterojunction had increased absorption by the α-Fe_2O_3 cores and $BiV_{1-x}Mo_xO_4$ shells and enhanced separation of photocarriers at the interfaces. Thus, the composite could achieve a much higher photoconversion efficiency (PCE) of ~0.53% at −0.04 V (0.56 V vs NHE) as compared to rGO–α-Fe_2O_3 or α-Fe_2O_3. The PEC water splitting mechanism of the α-Fe_2O_3–rGO–$BiV_{1-x}Mo_xO_4$ heterojunction given in Figure 13 shows that the energy bands of α-Fe_2O_3 and $BiV_{1-x}Mo_xO_4$ shift upward and downward, respectively, until their Fermi levels reach equilibrium.

The photogenerated holes and electrons appeared only in the VB and CB of α-Fe_2O_3 and $BiV_{1-x}Mo_xO_4$ upon irradiation. In this process, rGO acts as an electron conductor to enhance the electron–hole separation. The excellent band structure alignment and potential difference help rGO to efficiently transfer electrons from the conduction band of the $BiV_{1-x}Mo_xO_4$ shell to the conduction band of the α-Fe_2O_3 core, which then quickly transfer through the Ti substrate and external electrostatic field to the Pt counter electrode for the liberation of H_2 from water. Simultaneously, the hole in the VB of α-Fe_2O_3 migrates to the VB of $BiV_{1-x}Mo_xO_4$ via the rGO interlayer to oxidize water for O_2 evolution. The enhanced PEC water splitting efficiency is attributed to the combined effects of core–shell heterojunction formation and effective separation and transportation of photogenerated electron–hole pairs by rGO. This study opens a new avenue for the design and fabrication of GR-based core–shell heterojunctions for PEC water splitting.[91]

2.2.2. Graphene-Based Photocathodes for PEC Water Splitting

As described above, the practical implementation of PEC water splitting cannot be achieved without the development of suitable p-type semiconductors/photocathodes. Among the very few available as photocathode materials, Cu_2O is considered a potential candidate for water splitting due to its suitable band structure. However, Cu_2O suffers from severe photocorrosion under PEC water splitting. Researchers have found that GR can effectively reduce photocorrosion by rapidly extracting photoinduced charges from semiconductors due to its excellent electron acceptor and charge transfer capabilities. Tran et al. have successfully addressed the photocorrosion issue of Cu_2O by synthesizing an rGO–Cu_2O composite that shows a photocurrent of 0.12 mA cm^{-2} and H_2 production of 1.4 μmol h^{-1} g^{-1} at an applied bias of −0.4 V under visible-light irradiation. These experiments also showed a linear H_2 evolution for up to 15 h, in contrast to pristine Cu_2O, which completely deactivated after 5 h due to the self-reduction of Cu_2O into Cu by the photoinduced electrons. The increased stability and PEC performance is attributed to the rapid electron collection and transport properties of rGO, which not only suppressed the recombination of the photoinduced electron–hole pairs but also prevented the self-reduction of Cu_2O into Cu.[92] More recently, Dubale et al. obtained a higher and improved photocurrent density of −4.8 mA cm^{-2}, which is two times that of bare 1D Cu_2O (−2.3 mA cm^{-2}), at 0 V versus RHE under AM 1.5 illumination (100 mW cm^{-2}), and a solar conversion efficiency of 3.3% at an applied potential of −0.55 V by overlapping 1D Cu_2O with GR. The GR-modified photocathode showed a good photostability by retaining 83% of the initial photocurrent density after 20 minutes of standard solar irradiation, which is more than five times that of the bare Cu_2O (14.5%). The high PEC performance of the GR–Cu_2O nanocomposite is attributed to the improved crystallinity and the synergetic effect of GR in absorbing visible light, and the suppression of charge recombination and photocorrosion of the photoelectrode by preventing direct contact with the electrolyte.[93] In another study, Huang et al. have remarkably enhanced the PEC water splitting activity of silicon nanowires by spin-coating rGO on the nanowires, and the EIS measurements suggest that the reduction of trapping and recombination of photogenerated carriers, as well as the remarkable enhancement of PEC performance,

can be attributed to the low charge transfer resistance at the SiNW–rGO and rGO–electrolyte interfaces.[35]

2.3. Photocatalytic CO_2 Reduction

Solar-to-fuel generation (C1 hydrocarbons) from the photocatalytic reduction of CO_2 has become an attractive process and provides simultaneous solutions to global warming and the energy crisis. Many GR-based photoactive materials have been employed for photocatalytic CO_2 conversion to valuable hydrocarbon products. Huang et al. have discovered the role of GR and its defects on the photoreduction of CO_2 in a GR–P25 nanocomposite. The results show that GR–TiO_2 nanocomposites prepared by solvent exfoliation have lower defect density, which can effectively reduce CO_2 in the presence of water to produce CH_4 under visible- and UV-light irradiation. The high CO_2 reduction efficiency is attributed to the superior electrical mobility of GR, which facilitates the diffusion of photoexcited electrons to reactive sites, and the study provided new insights into the use of GR-based photocatalysts for the production of solar fuels.[35] Tu et al. fabricated robust hollow spheres of alternating TiO_2 nanosheets and GR nanosheets (GR–$Ti_{0.91}O_2$) using layer-by-layer deposition methods for the reduction of CO_2 to solar fuel. A ninefold increase in the photoreduction of CO_2 into renewable fuels (CO and CH_4) by GR–$Ti_{0.91}O_2$ hollow spheres was obtained as compared to commercial P25. The enhancement in photocatalytic activity is attributed to three aspects: (i) the ultrathin nature of $Ti_{0.91}O_2$ nanosheets, allowing charge carriers to move rapidly onto the surface to participate in the photoreduction reaction; (ii) the sufficiently compact stacking of ultrathin $Ti_{0.91}O_2$ nanosheets with GR nanosheets, allowing the photogenerated electron to make a fast transfer from the $Ti_{0.91}O_2$ nanosheets to GR and enhancing the lifetime of the charge carriers; and (iii) the hollow structure potentially acting as a photon trap-well to allow the multi-scattering of incident light for the enhancement of light absorption.[94] An et al. have successfully prepared an rGO–Cu_2O composite using a one-step microwave-assisted chemical method and proved that the rGO coating dramatically increases Cu_2O activity for CO_2 photoreduction. The CO_2 reduction efficiency of the rGO–Cu_2O composite was six times higher than the bare Cu_2O and 50 times higher than the Cu_2O/RuO_x junction after 20 hours under optimized conditions. The improved activity was attributed to the enhanced stability of Cu_2O due to the protective coating of rGO, as well as the efficient charge separation and transfer functions of rGO.[95]

Yu et al. have prepared rGO–CdS nanorod composites by a one-step microwave-hydrothermal method for the reduction of CO_2 to CH_4 without a noble metal like the Pt co-catalyst. The noble-metal-free optimized rGO–CdS composite with 0.5 wt % rGO content showed a high CH_4 production rate of 2.51 μmol h^{-1} g^{-1}, which was ten times better than the pure CdS nanorods and the Pt–CdS nanorod composite under optimized reaction conditions. The high photocatalytic activities are the result of effective electron acceptors, transport of photogenerated charge carriers, enhanced adsorption, and activation of CO_2 molecules by the rGO sheet.[84]

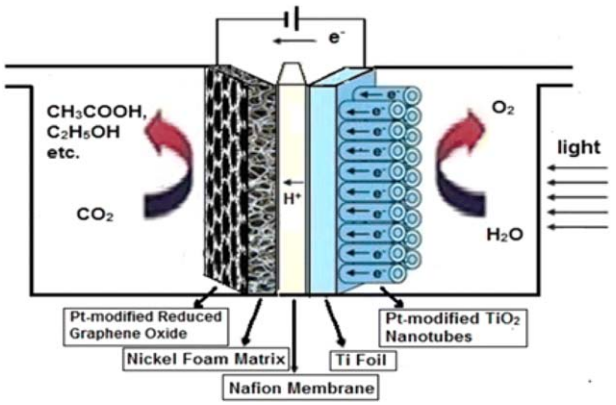

Fig. 14. Schematic diagram of the PEC system for CO_2 reduction. Reprinted with permission from reference [97]. Copyright 2014 American Chemical Society.

Lv et al. have prepared NiO_x-loaded rGO–Ta_2O_5 composites using a one-step hydrothermal method for the photocatalytic reduction of an aqueous CO_2 solution to CH_3OH and H_2. NiO_x–Ta_2O_5–rGO composites with 1 wt % GR content showed a conversion rate of CO_2 into methanol of up to 0.5 μmol g^{-1} h^{-1}, which was 3.4 times higher than the corresponding photocatalyst without GR. The enhanced conversion efficiency was due to the electron transfer and collection characteristics of GR, and rGO was found to be important in achieving high methanol yields for this multi-electron reduction process.[96]

Following the successful applications of GR to enhance the CO_2 reduction efficiency of particulate photocatalysts, Cheng et al. developed a novel light-driven PEC reactor (Figure 14), with Pt–rGO as a cathode catalyst and Pt-modified TiO_2 nanotubes (Pt-TNT) as PA. They found the effective conversion of CO_2 into species such as C_2H_5OH and CH_3COOH. The carbon atom conversion rate reached 1130 nmol/(h·cm^2), which was much higher than those achieved using Pt-modified carbon nanotubes and platinum carbon as cathode catalysts. The efficient dual-chamber PEC reactor, which combines the electrical cathode and PA, was designed to separate the photoinduced process into two physically distinct areas related to water oxidation and CO_2 reduction. This reaction system was able to limit the charge recombination, reduce the energy input, and increase the efficiency of CO_2 reduction reactions. The outstanding catalytic activity of Pt–rGO was mainly attributed to its high reactant absorptivity and efficient

charge transportation, which opens up a new direction for PEC CO_2 reduction to useful liquid products.[97]

2.4. Graphene: An Energetic Component in Solar to Electricity Conversion

The impressive properties of high optical transparency, remarkable electrical conduction, and mechanical flexibility of 2D GR and its derivatives have received profound attention for next-generation solar cells. The viability of large-scale synthesis through physical and chemical methods[17a,127] and the p-type behavior to achieve effective physical and catalytic properties[128] make GR a promising candidate for use in solar cells. Recent progress in the utilization of GR in solar cells has been widely reported elsewhere.[129] The recent application of GR in different solar cell architectures such as DSSCs and QDSCs and its underlying mechanism in improving the overall PCEs of the respective device configurations have been discussed.

The first report on DSSCs in 1991 by O'Regan et al.[130] opened up new avenues in next-generation solar cells at a low cost compared with silicon solar cells, with a remarkable PCE of 11.1%, and they recently reached a benchmark efficiency of 13%.[131] A schematic of the DSSC architecture is presented in Figure 15a. Photosensitizer molecules are assembled onto the mesoporous PA, which acts as a light receptor for solar irradiation and is sandwiched with an electrocatalyst (EC)-coated charge collector filled with a hole-transport electrolyte (HT). The photoexcitation of the PS ($D^+ + h\upsilon \rightarrow D^*$) under light irradiation leads to rapid electron injection into the conduction band of the PA (i.e., TiO_2), and further electrons reach the charge collector, where the original state of the dye can be regenerated by electron donation from the electrolyte ($D^* \rightarrow D^+ + e$). The collected photoelectrons in the charge collector are further transported to the counter electrode through an external circuit, and the circuit is completed through dye regeneration by half of a redox couple ($I_3^- \leftrightarrow 2I^-$) in the electrolyte.[132]

Typically, the following materials are used in DSSCs: indium- or fluorine-doped tin oxide (window layer or charge collector), a mesoporous TiO_2 layer (electron transport layer), organic/inorganic dye molecules (photosensitizers), iodide/triiodide (redox shuttle), and platinum counter electrodes (electrocatalyst towards triiodide reduction). Despite their effective performance, the inadequate and weak light transparency, significant sheet resistance of charge collectors (ITO or FTO substrates), poor charge separation at the TiO_2–dye/electrolyte interfaces, and expensive Pt counter electrodes limit the device parameters of open-circuit photovoltage (V_{oc}) and photocurrent density (J_{sc}), which restricts further industrial implementation. In this context, GR and its derivatives have been utilized in DSSCs, which can be overwhelmed by the above issues. In view of the recent literature, huge amounts of research have been conducted on GR-based DSSCs. Based on the reports of GR in DSSCs, the role of GR in various DSSCs is schematically illustrated alongside the corresponding energy level diagrams in Figure 15b.[129a] It clearly shows that GR can be practically applied as (a) a transparent window layer, (b) an electron transport layer or sensitizer with the PA, and (c) electrocatalytic counter electrodes. The underlying mechanism of each layer in Figure 15b will be discussed in the coming section.

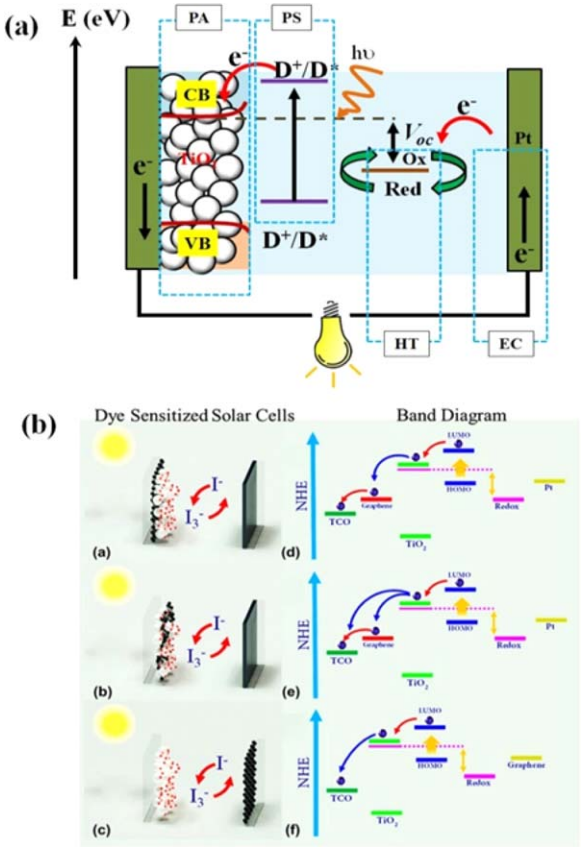

Fig. 15. (a) Structure of a DSSC. (b) Schematic illustration of GR utilization in DSSCs as (a) window layer, (b) electron transport layer, and (c) electrocatalyst; (d–f) the corresponding energy diagrams are presented on the right-hand side of each scheme. Reprinted from reference [129a]. Copyright 2014 Materials Research Society, London.

2.4.1. Graphene as a Photoanode

The advantages of layer thickness depend on optical transparency[133] and resistivity.[134] The GR has transparent conduction oxides, metal electrodes, and a preferred window layer (Figure 16a). The first-ever report by Wang et al.[135] on as-synthesized GR platelets transferred onto glass substrates led to a high-transmittance electrode material (97.7%, Figure 16b) compared with ITO and FTO substrates and opened up a new

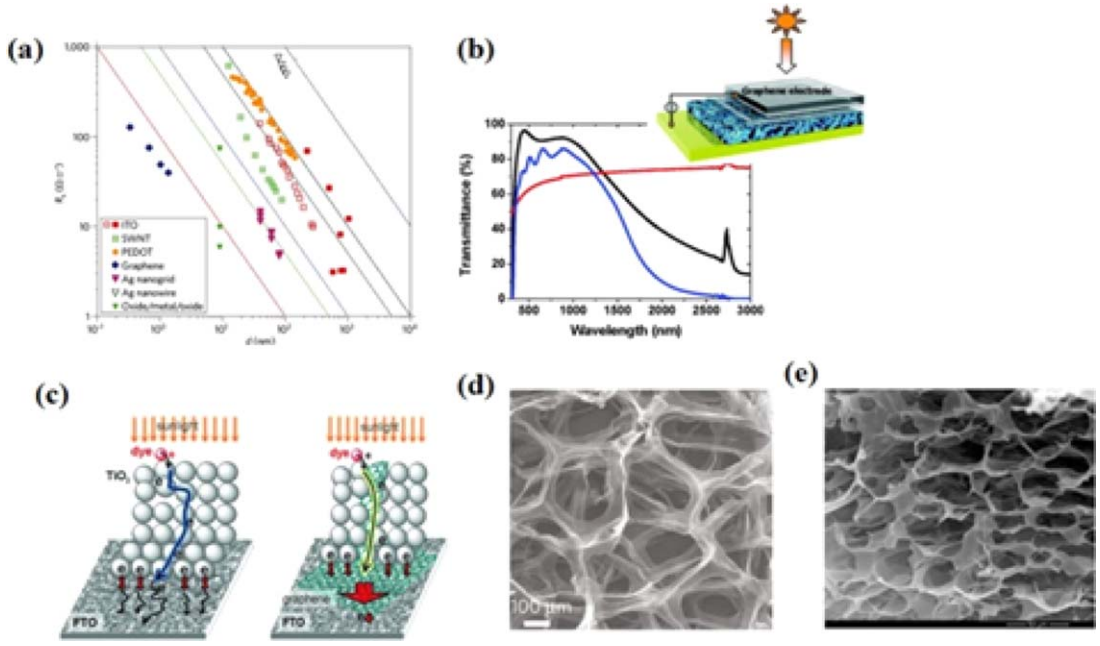

Fig. 16. (a) The plot of sheet resistance (R_s) versus film thickness (d) for various transparent conduction electrodes. Reprinted from reference [134]. Copyright 2014 Nature Publishing Group. (b) Transmittance of a ca. 10 nm thick GR film (red), in comparison with those of ITO (black) and FTO (blue). Inset: illustration of a DSSC using GR film as the electrode. Reprinted from reference [135]. Copyright 2007 American Chemical Society. (c) Schematic illustration of electron transport pathways at TiO_2/dye with and without GR interlayer. Reprinted from reference [139]. Copyright 2012 Wiley-VCH, Weinheim. (d,e) SEM images of 3D GR electrodes prepared by (d) the physical method (reprinted from reference [148], Copyright 2011 Nature Publishing Group) and (e) the chemical method (reprinted from reference [149], Copyright 2013 American Chemical Society).

avenue in the utilization of GR in DSSCs. However, assembling the pre-synthesized GR platelets onto the glass substrate resulted in highly defected edges of sheets (hopping from platelet to platelet), and introduced significant resistance in the electrodes, thus affecting the charge collection at external circuits. This issue can be overcome by replacing the continuous GR films with low defect concentration. For instance, the CVD-grown continuous films were transferred onto a glass substrate, and performed at a higher optical transference compared with ITO and FTO substrates.[136] The defect-controlled GR front contact substrate based DSSCs[136] exhibited 4.5 times higher PCE values compared with those reported by Wang et al.[135] under identical photoelectrode configurations. This led to controlling the PCE of the device by the GR defects at the front contact.

As shown in Figure 15a, the PA of a DSSC performs as an electron transporter, and conducts the electron from the excited dye sensitizers to the external circuit. Mostly, nanoparticulate-based electron transport layers (TiO_2 spherical particles) have been used in DSSCs and showed random electron transport from the point of electron injection (dye) to charge collector. Due to the presence of a higher amount of grain boundaries at the nanoparticulate electrode and control of the electron transport through an electron trapping/de-trapping mechanism,[137] there has been a lower efficiency of the device. A highly conducting 2D GR sheet is the appropriate composite candidate for the nanoparticulate electron transport layer (TiO_2), which markedly promotes the electron transfer from TiO_2 to a current collector[138] (auxiliary transport indicated in blue color in Figure 16b). In addition, the favorable band position of GR NHE at ca. −4.4 eV lies between the FTO (NHE ca. −4.7 eV) and TiO_2 (NHE ca. −4.2 eV) and can increase the electron mobility to the PA.[139] Moreover, the high electron-conducting characteristics of GR displayed a better performance than that of other 1D composite facilitators (carbon nanotubes), and the spatially well-dispersed GR 2D sheets also extend compatibility in order to accommodate a larger quantity of TiO_2 particles.[140] Apart from these merits, GR acts as an auxiliary binder (0.8 wt %) in producing crack-free TiO_2 mesoporous thick films without sacrificing the PCE of the device.[141]

A wide range of metal oxide–GR composites have been reported as PAs in photoelectric conversion devices. However, more reports are available on DSSCs using GR–TiO_2[139,142] and ZnO–GR[143] composites due to their flexible and facile synthesis. As previously reported, GR–TiO_2 composites (GT) can be synthesized by either (a) decoration of GR on pre-synthesized TiO_2 frameworks[144] and/or (b) in situ deposition of TiO_2 nanoparticles on pre-synthesized GR scaffolds.[145] Herein, GR could enhance the photocurrent density (J_{sc}) of

DSSCs compared with pristine TiO_2 electrodes.[146] The J_{sc} enhancement of GT composites is governed by several factors: (a) optical scattering phenomena that harvest red photons from the solar spectrum, and (b) auxiliary transport at metal oxide–dye interfaces that amplify the charge collection.[139] Nevertheless, GR composites enhance the performance of the DSSCs. Both GR and TiO_2 play a vital role in the overall performance of the device. One of the issues is that GR also absorbs light photons and may be detrimental for PCE when exceeding the optimized amount.[147]

Conversely, the TiO_2 particle size also affects the TiO_2–GR composite performance.[150] The smaller-sized TiO_2 could produce better connectivity with the GR network compared with the larger-sized TiO_2 particles. Further improving the conducting properties of GR by nitrogen doping (0.2 wt % N-rGO) led to a higher photocurrent density, thus resulting in a 13.2% higher PCE than pristine TiO_2 and GR–TiO_2 composites.[147] It is noteworthy to mention that TiO_2–GR composites enhance the photocurrents of the device through lowering the charge recombination at TiO_2–dye interfaces,[151] and do not shift the conduction band of TiO_2 or influence the recombination process. The recent demonstration on extending the wide porous PA with highly interconnected 3D GR backbone membranes[148,149,152] results from rapid electron transport with highly diffusive electrolyte percolation pathways (effective mass transfer),[153] which drastically lower the recombination loss at PA–dye/electrolyte interfaces.[154,155] It is anticipated that a thin layer of TiO_2 films on 3D GR electrodes (Figure 16d,e) could offer ample room for loading different wavelength-based dye sensitizers on one roof (panchromatic dye sensitizers).[156] Unlike conventional small-pore-sized GT electrodes, assembling panchromatic dye sensitizers at larger-pore-sized 3D GT electrodes is a futuristic approach for extending the visible-light harvesting across a broad range of the solar spectrum for graphene-based QDSCs.

Utilizing low-dimensional semiconductor quantum dots as light-harvesting components (denoted as PS in Figure 15a), instead of dye molecules, could reduce the device cost.[157] QDs have unique properties, such as (a) flexibility in bandgap tuning by varying the particle size, (b) high extinction coefficients, and (c) high dipole moment, making them important for next-generation solar cells.[158] Furthermore, multiple exciton generation phenomena and the extraction of hot electrons from QDs can promote the theoretical PCE of cells to surpass the Shockley–Queisser limit (31%).[159] Great efforts have been invested in designing the QDSC architecture over the last five years and the PCE has monotonically increased and currently stands at a certified efficiency of 6.6% for CuInS QD sensitizers.[160] Still, further development is required to achieve competitive performance with DSSCs.

Compared with dye sensitizers (10^{-8} s), faster electron–hole recombination times for QDs (10^{-11} s)[161] lead to band–band recombination or surface states[162] and often affect the charge extraction from QDs. In order to improve the charge extraction from QDs, extensive research has been carried out on combining a variety of narrow-bandgap-energy semiconductor QDs (e.g., CdS, CdSe, PbS, CuInS, CuInSSe, CdTe) with 1D[163] and 3D[164] (nanoparticulate, nanowire, nanofiber, and nanotree) structures. These 1D and 3D nanowires, based on the PA framework, encompass radial electron transport and result in efficient charge extraction from QD–electrolyte interfaces to the charge collector. Despite the effective charge transport, a complicated procedure involved in these electrodes restricts further development of QDSCs. Inserting highly conductive 2D GR layers as an electron transport layer in between the TiO_2–QD or TiO_2–TCO interfaces could enhance the charge extraction from QDs to the external circuit. The first report on QD-sensitized GR solar cells was from Guo et al.[165] They demonstrated that the CdS QDs in between the GR layers (30 nm) were assembled by several coating cycles onto the conducting substrate as shown in Figure 17a. Interestingly, the QD–GR electrode showed a higher photocurrent than that of similar QDs coated on a single wall of carbon nanotube membranes (inset of Figure 17a). This implies that there is a good distribution of QDs on GR. Furthermore, the favorable work function of GR could afford effective separation of the photogenerated electron–hole pairs and transfer of the electrons to the electrode surface. Moreover, the layer-by-layer GR-assembled electrode results in different wavelength or particle sizes of QDs, thus forming "rainbow-type QDSCs".[166]

However, the photocurrent obtained by reducing the GR thickness resulted in poor internal surface area for substantial QD loading. This issue can be resolved by introducing TiO_2 to the interfacial layer in between GR and the QDs, which enhances the internal surface area of the electrode and obviously amplifies the QD loading. Thus, the output photocurrent density is improved.[167] A schematic illustration of facilitated electron transport in QD–GR composites with the TiO_2 interfacial layer is presented in Figure 17b (inset shows the IPCE spectra).[167] In addition, the low-temperature-processing characteristics of GR would allow the possibility of flexible QDSCs as compared to other TCO materials. Chen et al. fabricated flexible QDSCs based on a GR interfacial layer with an internal quantum efficiency of 17%, endorsing the viability of GR in flexible devices.[168]

Lightcap et al. explored the advantages of GO and rGO composites in QDs sensitized by TiO_2 mesoporous electrodes.[169] The schematic structure of GO- and rGO-incorporated QDSCs is depicted in Figure 17c. Here, the GO composite layer triggers the charge separation and electron conduction through the QD film, thus allowing three-dimensional sensitization and improved photocurrent response (~150%) over those prepared without GO. As shown in the inset of Figure 17c, the IPCE

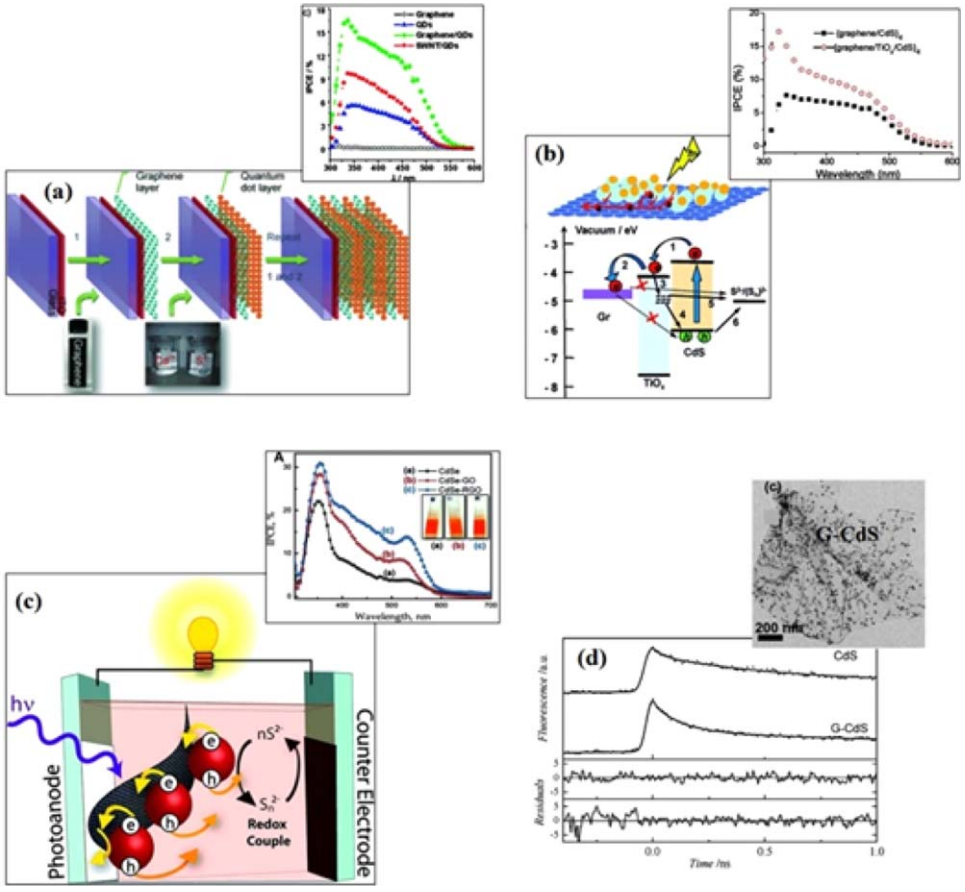

Fig. 17. (a) Layer-by-layer grown GR-based QDSCs (inset: IPCE spectra). (b) Schematic illustration of energy level of GR interfacial layer in between QD-sensitized TiO_2 and TCO substrates (inset: IPCE spectra). (c) Typical device structure of GR/TiO_2 PA based QDSCs (inset: IPCE spectra). (d) Time-resolved fluorescence decay spectra of the free CdS QDs and G-CdS (inset: TEM image of G-CdS).

spectrum clearly demonstrates the critical role of the rGO composite layer in enhancing the internal quantum efficiency of the QDSCs.

Chen et al. explored the GR composite in TiO_2 electrodes (GT) and showed a 40% higher PCE ($\eta = 4.02\%$) than that of the pristine TiO_2 electrode ($\eta = 2.85\%$) due to improved charge transport at the TiO_2 network and charge extraction from the QDs to TiO_2.[170] Several authors have studied the efficient charge transfer from semiconductor to GR.[171] Typical time-resolved fluorescence spectroscopy results of CdS QDs with and without GRs are illustrated in Figure 17d (inset shows the corresponding TEM image of CdS QD decorated GR matrix).[172] This clearly explains the lifetime of the CdS, reduced from 0.47 ns to 0.12 ns in the GR composite, which ensures the charge extraction from QDs to GR. Furthermore, charge extraction from QDs to GR under light irradiation was confirmed by Jung et al.[173] The charge transfer from CdSe QDs to GR was exclusively studied by different types of connecting binders, which were covalently attached with GR using (a) aryl radicals and (b) pyridine binders. The covalently attached aryl radical binders with GR electrodes showed ~10% higher external quantum efficiency than pyridine binders, thus confirming the interaction between CdSe QDs and GR film.[173] Chen et al. reported the influence of GR in the underneath layer in between the FTO substrate and QD-sensitized ZnO nanowire array.[170] As a result of reduced series resistance between FTO and GR–ZnO, the electron transfer increases the fill factor of the device, and the overall PCE increased to 54.7% compared to without the GR interfacial layer.[170]

2.4.2. *Graphene as a Counter Electrode*

The redox mediator (I_3^-/I^-) plays a crucial role in the charge transport of DSSCs. As shown in Figure 15a, under light irradiation, the photoelectrons pass to the charge collector through the electron transport layer (TiO_2) and then traverse to the external load, until they finally reach the counter electrode. At the counter electrode, these electrons reduce triiodide to iodide as follows: $I_3^- + 2e^- \rightarrow 3I^-$. Furthermore, the reduced redox

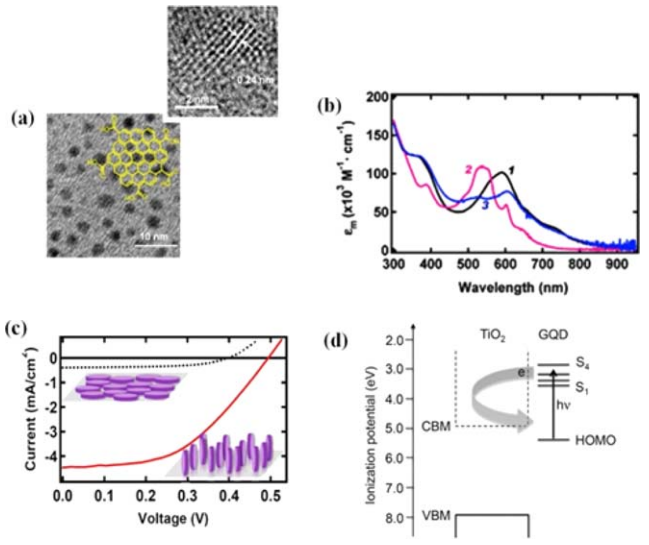

Fig. 18. (a) TEM image of solution-grown GQDs (inset: lattice distance of GQDs with 0.24 nm). Reprinted from reference [184]. Copyright 2013 American Chemical Society. (b) The optical absorption spectra of graphene QDs in toluene prepared from different carbon moieties (1:C168, 2:C132, and 3:C170 indicated in Figure). Reprinted from reference [186]. Copyright 2010 American Chemical Society. (c) Current–voltage characteristics of solar cells sensitized by GQDs with different orientations. Reprinted from reference [186]. Copyright 2010 American Chemical Society. (d) Energetic structure of TiO_2–GQD interface. Reprinted from reference [197]. Copyright 2013 American Chemical Society.

species (I^-) diffuse into bulk electrolyte and mesoporous photoanode (PA in Figure 18a) and the dye molecules are regenerated from their oxidized state: $2D^* + 3I^- + 2D \rightarrow I_3^-$.

Therefore, regeneration of the dye sensitizers relies on the performance of the counter electrode and they are considered as indispensable components in DSSCs.[174] For obtaining fast reaction kinetics in triiodide reductions, a thin platinum film coated TCO has often been utilized as a counter electrode. Besides the excellent performance of Pt electrodes in triiodide reduction, the lower material usage (about 50 mg m^{-2}) of the thin layer of platinum, which is expensive and less abundant in nature, makes this method suitable for mass commercial production. In this context, the low-cost and high electrocatalytic property 2D graphene sheets are an appropriate choice for counter electrodes toward triiodide reduction. A huge amount of research has been conducted over the last five years on graphene-based counter electrodes to compare their use as anodes, sensitizers, and electrolytes in DSSCs. This not only elucidates the potential of graphene for reducing the cost of the device but also encourages the DSSC architecture to have a new dimension.

One of the limitations of graphene is that it possesses large amounts of basal planes that are not catalytically active in nature, thus inhibiting the charge transfer kinetics at the electrode–electrolyte interface. The poor catalytic performance of the basal plane increases the charge transfer resistance of graphene and thus lowers the mass diffusivity of triiodide species.[175] Therefore, the catalytic sites have to be promoted in the graphene layer by forming edge sites through (a) doping with metals and non-metals,[176] (b) surface treatment[128d] or functionalization,[177] (c) decorating metal or semiconductor co-catalysts,[178] or (d) coating it with electrocatalytic composite materials (e.g., polymers, alloys). However, the basal planes are responsible for the conducting nature of graphene. Therefore, tailoring graphene with substantial catalytic edges, without sacrificing the conductive properties, remains a challenge. We strongly recommend the recent reviews by Das et al.[129a] and Roy-Mayhew et al.[129c] for more insight and greater functionality of graphene in counter electrodes. They briefly reviewed the wide range of graphene composites.

The advantage of low-temperature processing is that graphene is highly desirable in fabricating flexible counter electrode based DSSCs.[179] Also, the highly conducting nature combined with the substantial optical transparency of graphene could support the development of TCO-free DSSCs.[180] Exclusively, for non-transparent metal-based photoanodes (TiO_2 nanowire grown onto Ti), the highly reflective nature of Pt is not suitable for allowing backside illumination. Herein, the graphene-coated glass substrates afford dual usage as optically transparent TCO-free substrates (allowing the backside illumination) and catalytic counter electrodes. In QDSCs, polysulfide is the most utilized electrolyte and often results in sluggish coating on the Pt counter electrode, which is detrimental for the long-term performance in maintaining the S_x^-/S^{x-} reduction.[181] Interestingly, the hydrophobic nature of graphene prevents sulfur coating, unlike Pt. As a result, graphene-based counter electrodes drastically enhanced the overall performance of the QDSCs compared with the Pt-based counter electrode. Recently, semiconductor (CuS, PbS)[182] coated rGO composite counter electrodes were widely applied in QDSCs, where the semiconductors are partially supported by rGO in polysulfide reduction and lower the charge transfer resistance at the counter electrode.

2.4.3. Graphene as a Sensitizer

Undoped graphene shows a broad absorbing profile of about 2.3% of light with each monolayer.[183] This highlights the versatility of graphene as a light-harvesting sensitizer in analogue with dye molecules. Nevertheless, bulk graphene has serious limitations compared with dye sensitizers: (a) bulk graphene has a zero bandgap inadequate to produce excitons, and (b) a monolayer of graphene assembling onto the photoanode (PA in Figure 15a) is also not a trivial task. Along these lines, a single-atom-thick and nanometer-sized (0.23 nm lattice distance) (Figure 18a)[184] planar sheet of graphitic carbon called graphene quantum dots (GQD) has received promising attention, and recent reports on GQD-based fluorophores in

bioimaging display their potential for light reception.[185] Figure 18b shows the optical absorbance spectra of GQDs prepared from solution-chemistry approaches, emphasizing the visible-light action.[186] The tunable photoluminescence[187,188] properties originating from quantum confinement, excellent edge effect,[189] photostability, biocompatibility with nature,[190] water solubility, chemical inertness, and low cost make them attractive as a new class of materials in solar cells.[191] Particularly, the bandgap and redox energy level tuning properties of GQDs allow them to be utilized as sensitizer in DSSCs.[192] The possibility of GQDs as a light-harvesting sensitizer was first demonstrated by Yan et al.[193] Li et al.[79] demonstrated the function of GQDs in mesoscopic solar cells by tuning the bandgap from UV to visible-light wavelength. The mostly solution-based GQD synthesis affords low dimensions with appreciable bandgap energy and an edge effect.[194] However, an unexpected particle aggregation issue arose from solution-chemistry-based GQDs, which results in graphitic properties and affects their bandgap formation. This issue was overcome with shielding agents, by covalently attaching multiple 1,3,5-trialkyl-substituted phenyl moieties (at the 2-position) to the edges of the graphene.[195] However, the shielded GQD-based DSSC configuration shows lower efficiency with a J_{sc} of 200 μA/cm^2, V_{oc} of 0.48 V, and fill factor of 0.58.[193] The much lower current density is attributed to the weak adsorption of GQDs onto metal oxide surfaces, thus leading to poor charge injection from GQDs to TiO_2. Strikingly, the orientation modified GQDs (in plane with substrate) as disk-like shapes showed a higher photoconversion efficiency than that of the "face-on" orientation of GQDs due to the higher packing density (Figure 18c).[195,196] The possibility of using hot electron injection at GQDs anchored by TiO_2 (110) was exposed by Williams et al.,[197] which was evidence that the GQDs can be implemented in a hot carrier solar cell. Yet, the energy level position of GQDs is not favorable to TiO_2, as the HOMO level of the GQDs is closer to the TiO_2 conduction band (Figure 18d), which allows the back flow of electrons and leads to recombination (boomerang effect).[186] Very recently, Ji et al. proposed a pre-treatment layer of polyphenylene precursor functionalized onto the TiO_2 surface, which showed effective anchoring of the graphene molecules (GM) without aggregation and resulted in a broad range of visible-light absorbance at 550 nm with a 0.8% PCE.[198] The synergetic approach of hot electrons harvested from GQDs and enhanced visible-light harvesting from dye sensitizer with minimal utilization provided a new platform for dual sensitizers (GQDs/dye) in the future approach to DSSCs. Fang et al.[199] realized composite (GQDs/dye) sensitizer based DSSCs with a minimum dye adsorption with a J_{sc} of 14.07 mA cm^{-2} and η of 6.10 ± 0.01%, which were higher than those of the conventional DSSC (without GQDs). The enhanced photoconversion efficiency is mainly attributed to the unique photoexcitation response of the GQDs and the hot electron injection from GQDs into TiO_2. This study indicated that GQDs can improve the properties of DSSCs and reduce the dye sensitizer loading quantity significantly. Further research is required to minimize the recombination at TiO_2–GQDs interfaces by using appropriate material engineering, and is expected to offer GQDs as a superficial sensitizer in mesoscopic solar cells.[197]

3. Energy Storage Applications

Since GR was introduced, it has received considerable attention in energy storage devices due to its unique properties such as high porosity, large surface area, robust mechanical strength and elasticity, high conductivity, electrochemically active nature, stability, and low-cost preparation. Its abundant availability and lack of toxicity make it fit to be used for energy storage devices. This review is focused on the applications of GR in the areas of lithium-ion batteries, fuel cells, and supercapacitors.

3.1. Lithium-Ion Batteries

Lithium-ion batteries are devices that can store and supply electricity within a certain period of time. GR has been used as a promising material in lithium-ion batteries as an anode and cathode candidate. The advantages of applying GR to lithium-ion batteries are higher energy capacities and longer cycle lifetimes. Such batteries are suitable for use within electric vehicles, where they can be a solution to prevent pollution and reduce emissions of greenhouse gases from petroleum-based vehicles.[200] Portable electronic devices such as computers and telephones also use lithium-ion batteries based on GR. However, in the future, lithium-ion batteries need to have a higher rate of recharging, longer lifetime, and lower cost. GR has been used as an anode and cathode material in lithium battery applications.

3.1.1. Anode Materials

Commercially, graphite has been employed as an anode material for lithium-ion batteries because of its high Coulombic efficiency.[201] Nevertheless, GR showed significant improvement, where the power output of the device increased and the charging time was also reduced.[202] The specific capacitance increased from 372 mA h g^{-1} (commercial) to 1264 mA h g^{-1} at a low charge–discharge rate (such as 50–100 mA g^{-1}); at a high charge/discharge rate (500 mA g^{-1} or higher), the durability also increased up to 848 compared to that of the commercial with only 240.[200a] The results suggested that the physical properties of the GR help in improving the lithium-ion batteries in terms of high electrical conductivity, vast surface area, unique heterogeneous electron transfer, and charge carrier rates. Further works have been done by Wu et al. to enhance the rate capabilities of the lithium-ion battery by introducing dopants.[203] The nitrogen- and boron-doped GR showed great potential. The results indicated at a low charge/

discharge rate of 50 mA g^{-1}, the rate of reversible capacity increased up to 1043 mA g^{-1} and 1540 mA g^{-1} for nitrogen- and boron-doped GR, respectively. Furthermore, the results also exhibited that the charge and discharge process can be done in a very short amount of time ranging from one hour to several tens of seconds. The improvement in the results is due to the improved surface structure, heteroatomic defects, better electrode–electrolyte interface, increased intersheet distance, high conductivity, and thermal stability.

GR has been doped with Fe_2O_3, SnO_2, C_{60}, carbon nanotubes, and Mn_3O_4.[13,204] However, the results showed lower performance compared with GR nanosheet. Wang et al. have reported that Mn_3O_4 and rGO have enhanced performance.[13] The rate of reversible capacity was ~390 mA h g^{-1} until a high current density of 1600 mA g^{-1}, which is higher than the theoretical specific capacity of graphite (372 mA h g^{-1}). This may be because the composite materials have low electrical conductivity and uncontrolled structures or interfaces that affect the composite. The results may also suggest that the electron transfer could have an effect because of the presence of other materials. However, GR is more suitable to be applied as an anchoring nanoparticle and for creating good contact between the electrode and current collector.[13,205] At the same time, by introducing GR, the volume of expansion/contraction and the aggregation of nanoparticles can be controlled during the reverse process.[206] This type of research has been performed by Zhou et al.[206] They found that the composite of rGO and Co_3O_4 exhibited high cycling stability. The results obtained in their study showed 1100 mA h g^{-1} at a current density of 74 mA g^{-1} and a discharge capacity of 1000 mA h g^{-1} of up to 130 cycles. The results illustrated that by controlling the microstructure of the semiconductor material, the devices have a higher performance, as supported by the work by Xu et al.[207] that used GO nanosheets wrapped with Cu_2O microspheres. By obtaining large surface areas of a core–shell structure, Cu_2O and GR formed composite materials and showed enhancement in the performance of anode materials for lithium-ion batteries. The GO functions as an efficient 3D conductive network and lithium storage active material, and the Cu_2O is a skeleton to support the multilayer GO sheets and avoid aggregation. The results indicated 458 mA h g^{-1} of reversible capacity of 100 mA g^{-1} after 50 cycles. The devices also demonstrated highly stable performance even at a high charge–discharge rate of 1000 mA g^{-1}, showing a reversible capacity of 240 mA h g^{-1} after 200 cycles. At the same time, Kim et al. demonstrated that lithium incorporated with rGO exhibited a capacity of 540 mA h g^{-1} that was reversibly obtained over 100 cycles, as illustrated in Figure 19.[208]

This finding leads to the conclusion that GR is a superior electrode for anode materials in lithium-ion battery applications. Finally, the performance of GR as an anode material for lithium-ion batteries is listed and compared in Table 3.

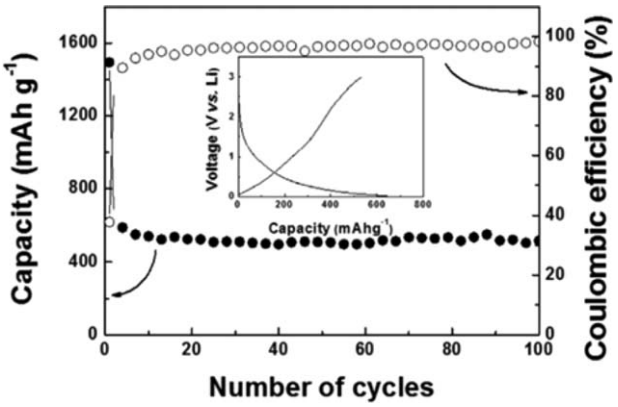

Fig. 19. Cycle stability of the rGO anode (inset: charge/discharge profile) in the voltage window between 0.01 and 3.0 V. Adapted from reference [208] with permission from Nature Publishing Group, copyright 2014.

Table 3. The performance of GR or incorporated GR as an anode for lithium-ion batteries.

Material	Specific capacity (mA h g^{-1})	Current density (A g^{-1})	Year/ref.
Cu_2O/GO	458	0.1	2014[207]
Li/rGO	540	0.1	2014[208]
MnO_2/GR nanoribbons	890	0.100	2013[209]
N-doped GR/SnO_2	683	1.000	2012[210]
B-doped GR	1540	0.05	2011[203]
Co_3O_4/rGO	1000	0.074	2011[206]
N-doped GR	1043	0.05	2011[203]
Mn_3O_4/rGO	390	1.6	2010[13]
GR	540	0.05	2010[202c]

3.1.2. Cathode Materials

GR has been employed in lithium-based rechargeable batteries because of its superior characteristics. In lithium-ion batteries, the cathode plays an important role in the performance of the devices. However, many studies focus on GR as an anode current collector rather than studying it as a cathode material. This is because cathode material properties include poor electrical conductivity, sluggish kinetics of electron and lithium-ion transportation, low specific capacities, and particle agglomeration generated from their nanostructures.[211] In an early study by Liu et al., it was reported that the nanocomposite $Li_3V_2(PO_4)_3$ (LVP)/GR functioned as the cathode in a lithium-ion battery.[212] In the presence of GR, the devices showed very high rate performance and cycling ability for lithium-ion batteries. This occurred due to the large surface area of GR, which adsorbed and attached tightly with the LVP.

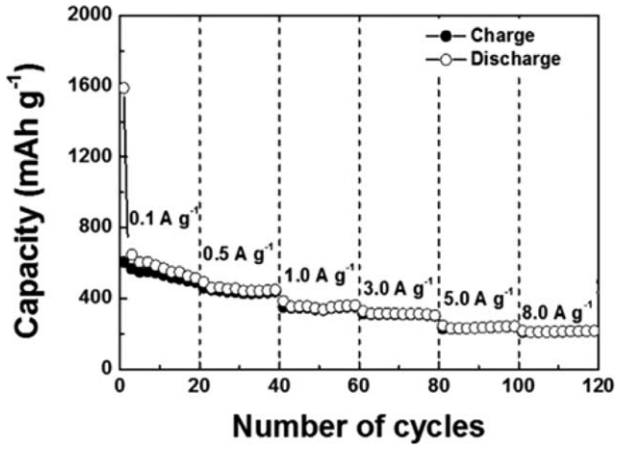

Fig. 20. Rate capability of the rGO anode at different current rates from 0.1 to 8.0 A g^{-1}. Adapted from reference [208] with permission from Nature Publishing Group, copyright 2014.

Through these, the Li^+ ions easily can intercalate and exfoliate. These results showed high electron conductivity and electrochemical performance. However, the cathode material properties such as low ion conductivity limited the performance of the devices. Similar results were obtained with other composites, such as $LiFePO_4$/GR,[213] $LiMn_2O_4$/GR,[214] and $LiMn_{1-x}Fe_xPO_4$/GR.[215] The highest-reported lithium-based composite is $LiMn_{1-x}Fe_xPO_4$/GR.[215] The results from this experiment demonstrated specific capacities of 107 mA h g^{-1} at 50 cycles and 65 mA h g^{-1} at 100 cycles.

Then, vanadium-based devices showed to be more promising, where VO_2/GR led to a device with high reversible capacity and ultrafast charging and discharging capability.[216] This result was achieved by controlling the surface morphology by making GR nanoribbon and crystalline structures. The structure increased the number of ions that moved between the interfaces, which led to an improved performance of the device. V_2O_5/GR subsequently took the lead.[217] By introducing V_2O_5 nanowires, which are already known to have a large surface area, the results exceeded expectation. This experiment demonstrated specific capacities of 10000 mA h g^{-1} for 100000 cycles. Thus, it can be concluded that the electron-conducting GR networks formed, largely improving the electron conductivity and electrochemical properties of the materials. In 2014, Kim et al. showed greater improvement with Li/functionalized GR as a cathode material, where the capacity was 100 mA h g^{-1} at a current density of 8000 mA g^{-1} as seen in Figure 20.[208]

The results suggest that the incorporated Li will produce superior cathode electrodes. This is also due to the characteristic factors of the material itself, where the lithium and GR have a higher surface area and higher rate of charge transfer. In order to clearly compare the performance of these materials, the results are displayed in Table 4.

Table 4. The performance of GR or incorporated GR as a cathode for lithium-ion batteries.

Material	Specific capacity (mA h g^{-1})	Current density (mA g^{-1})	Year/ref.
Li/functionalized GR	100	8000	2014[208]
$LiMn_{1-x}Fe_xPO_4$/GR flake	208	17	2013[214b]
GR/$LiFePO_4$	165	17	2012[212]
V_2O_5/GR	94.4	10000	2012[216]
$LiMn_{1-x}Fe_xPO_4$/rGO	65	17000	2011[214b]

3.2. Fuel Cells

Fuel cells are energy storage devices that use oxygen and methanol as a medium to convert chemical energy from a fuel into electrical energy. For environmental impact toward green energy technology, fuel cells are required to have an ideal electrode material, oxygen, and oxidation of methanol.[218] Before GR, carbon nanotubes were suitable nanomaterials for oxygen reduction reactions towards fuel cell applications.[219] In 2009, Kou and co-workers obtained significant electrocatalytic activity in acidic medium, using Au nanoparticles and multiwalled carbon nanotube composite materials.[220] GR has received great interest in fuel cell applications for anode and cathode current collectors, and is advantageous because of its large surface area, excellent electrical conductivity, electrocatalytic properties, and low production costs.[221] In 2006, Alexeyeva et al. used GR sheets with platinum nanoparticles for the electrocatalytic reduction of oxygen.[222] The results obtained in this study represented a new era for GR, with the composite showing better performance in terms of catalytic activity, stability in electrochemical surface area, and oxygen reduction activity. The high performance is due to the large surface area of platinum nanoparticles produced by small-sized nanoparticles and less aggregation of platinum.

Furthermore, Brownson et al. reported that GR doped with nitrogen acts as a metal-free electrode, which exhibited improvement in electrocatalytic activity, long-term operational stability, and tolerance.[223] In proton exchange membrane fuel cells (PEMFCs), as reported by Jafri et al., replacing commercial Pt catalysts with the Pt-loaded GR nanosheet and nitrogen-doped GR nanosheet in the fuel cell resulted in improved performance in terms of electrical conductivity and adsorption.[224] This was due to the presence of nitrogen in GR that created the defects and increased the surface area, allowing the platinum nanoparticles to attach. Therefore, it can improve the adsorption and electron transport and lead to improvements in the electrical conductivity of the fuel cell as reported by Zhang et al.[225] They demonstrated that the Pt nanoparticles were deposited on graphite submicron particles, using an ethylene glycol reduction method used for polymer

electrolyte membrane fuel cells. The results have been compared to the CNT and carbon black doped with Pt; they have shown improvement in the electrocatalytic activity and enhanced durability. Much research has been carried out using GR as a catalyst in fuel cell technology, leading to improvement in terms of the performance and cycle of the cells. The highest-performance fuel cells were reported with GR by Kakaei and Zhiani.[226] They modified the platinum–GR, using cyclic voltammetric techniques, and observed a reduced onset potential of 180 mV compared with the commercial platinum/carbon value of 280 mV. However, the catalytic activity improved to 1315 A g^{-1} from the commercial value of 725 A g^{-1}. The results indicated that the use of GR in fuel cells leads to enhanced electrocatalytic activity, durability, and improvements in the absorption of the surface, as reported by Xin et al.[227]

3.3. Supercapacitors

Supercapacitors can be classified as energy storage devices that have high power density and high cyclability compared to batteries. The advantages of supercapacitors are that they are maintenance free, have simple circuits required for charging, and are environmentally friendly devices. The device can store the charge electrostatically using reverse adsorption of ions of the electrolyte onto an active material.[228] The key to success in all electrochemical devices is to produce electrodes with a large surface area and excellent electrical conductivity, which makes GR a suitable candidate for supercapacitor device applications.

In the early stages where GR was introduced to supercapacitors, the results obtained were 130 F g^{-1} using chemically modified GR, which is far away from the theoretical capacity. The supercapacitors based on GR materials can achieve an electric double-layer capacity of ~550 F g^{-1} if all the area is fully covered.[8,229] The improvement in capacity of up to 264 F g^{-1} using hydrazine rGO sheets resulted from the improvement of the surface area, but this is still lower than the theoretical capacitance.[230] This may be due to the aggregation and restacking between individual GR sheets.[231] Two years later, Yu et al. improved the device up to 315 F g^{-1} using MnO_2–rGO.[232] The results indicated that by incorporating semiconductor materials with rGO, high charge capacitance can be obtained.

The next approach indicated that GR incorporated with polymers is more promising, where the polyaniline nanorod composite with rGO represented the first supercapacitor to surpass the theoretical value. The resulting pattern has been reported to be as high as 970 F g^{-1} at a discharge current density of 2.5 A g^{-1}.[233] Furthermore, the NiO–GR composite has been explored, which indicated a large capacitance result. A capacitance of ~1100 F g^{-1} was obtained in this study at a current density of 10 A g^{-1} with high cycling stability.[210] The results suggest that better contact between the GR and NiO and large surface area for both materials allow for rapid charge transfer between the materials and active material to collect current. In addition, this is also due to the characteristics of the materials chosen. Xu et al. reported that the holey GR framework exhibited superb potential as a supercapacitor of up to 310 F g^{-1} at a current density of 1 A g^{-1} in aqueous electrolyte solution, as shown in Figure 21.[234]

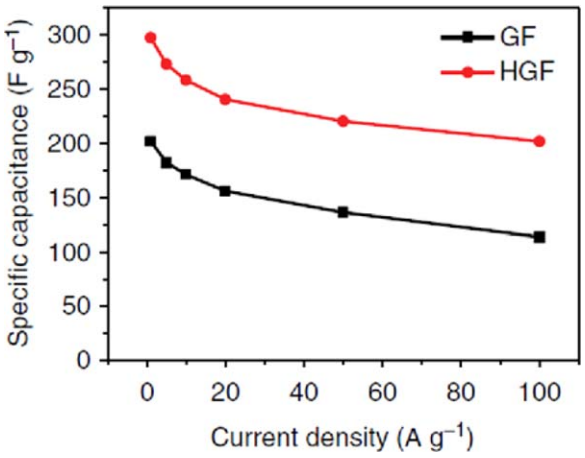

Fig. 21. Comparison of specific capacitances of HGF and GF electrodes versus current densities. Adapted from reference [234] with permission from Nature Publishing Group, copyright 2014.

Compared with the other types of carbon-based material, the large surface area produced by abundant wormlike tortuous pore channels leads to an increase in the performance of the supercapacitor. However, in this research, it can be concluded that the GR building block with an ideal two-dimensional flat surface of the holey GR increased the porous network structure. The nanopores in the GR building block also have desired sizes that can function as ion transport shortcuts between each layer of GR in order to enhance the ion transport process for improved rate performance. It also suggested that this type of nanopore is suitable to be used in the organic and aqueous electrolytes, which only give 4% different results. Furthermore, there are still a lot of aspects that need to be covered in order to obtain the desired supercapacitor. For comparison, the electrochemical performance of GR as an electrode for supercapacitors is illustrated in Table 5.

4. Environmental Applications of GR Molecules

The effects of globalization and industrialization have increased the amount of contamination in soil and water. This leads to severe environmental problems and health issues. Industrial plants generate increasing amounts of environmental concerns through enormous amounts of wastewater

Table 5. The electrochemical performance of GR as an electrode for supercapacitors.

Material	Capacitance ($F\,g^{-1}$)	Current density ($A\,g^{-1}$)	Year/ref.
Holey GR	310	1	2014[234]
Vertically oriented GR	130	10	2013[235]
NiO/GR	1100	10	2012[210]
PANI/GR	970	10	2012[233]
MnO_2/rGO	315	10	2011[236]
Poly modified GR	185	10	2010[237]
Hydrazine rGO	264	10	2009[230]
Chemically modified GR	130	10	2008[8]

production. Such wastewater contains toxic organic compounds,[238] including organic dyes, phenols, biphenyls, pesticides, fertilizers, hydrocarbons, plasticizers, detergents, oils, greases, pharmaceuticals, proteins, carbohydrates, etc.[239] The increasing environmental contamination concerns lead to an emphasis on new material synthesis, with new molecular materials, especially those using GR composites, to increase the photoredox activities.[240] This section will review the environmental applications of GR in pollution management via gas adsorption and water remediation. The organic components in the wastewater can be removed through various physical, chemical, and biological technologies such as the advanced oxidation processes (AOPs), including the Fenton reaction, photocatalysis, sonolysis, ozonation, and combinations of these techniques.[241] GR has been used as a remediation agent, especially through the adsorption and photocatalytic approaches. Adsorption is a surface phenomenon that depends on many factors such as the nature of the adsorbate and adsorbent and the physical characteristics, i.e., temperature, pH, concentration of pollutants, contact time, and particle size.[242] The photocatalytic approach involves light-induced photochemical reactions due to the unique electronic band structure of the semiconducting materials involved in the reaction process. The absorption of photons in the semiconductor generates excited electrons and holes in the conduction and valence bands, respectively.[243] These excited charge carriers recombine or get trapped in metastable surface states on the catalyst surface due to their highly reactive radical nature, with robust reducing and oxidizing capacity.[243] Large numbers of semiconductor[238f,244] materials have been used in the pollutant degradation process in both the liquid and gaseous regimes. Carbon-based materials have been used extensively in water purification and pollutant degradation processes. Carbon materials have received more attention in photocatalytic applications due to their unique structural properties, large surface area, pore volume, and presence of surface functional groups.[245]

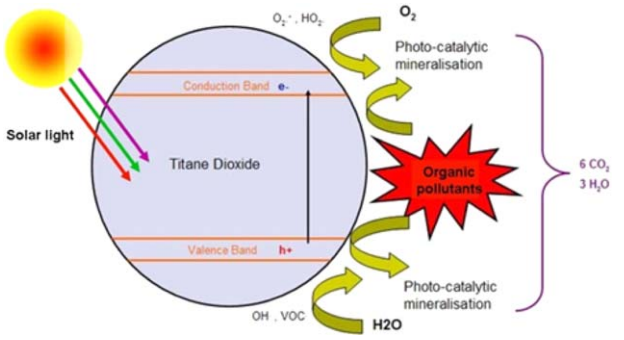

Fig. 22. Illustration of the photocatalytic process for degradation of pollutants by TiO_2. Reprinted with permission from Xiaobo Chen, University of Missouri – Kansas City.

4.1. Photocatalytic Degradation of Pollutants

The photocatalytic action requires the catalytic species to be active with respect to the illumination by light on the semiconductor surface. Upon illumination, the semiconductor will generate electron (e^-)–hole (h^+) pairs that take part in subsequent dark (thermal) redox reactions with adsorbed molecules that then decompose.[246] The following steps are involved in the process of photocatalytic degradation of pollutants, as shown in Figure 22 (here TiO_2 semiconductor is used as the photocatalytic material):

- The excitation of electrons from the valence band to the conduction band, when TiO_2 absorbs energy equal to or larger than the bandgap.
- The excitation of these electrons results in the generation of "holes" (electron vacancies) in the valence band.
- The results of excitation will also generate oxidizing and reducing agents.
- The holes (h^+) react with water and generate highly active hydroxyl radicals ($OH^\bullet$) that can act as a powerful oxidant.
- The hydroxyl radicals can react with organic pollutants to degrade or oxidize them to form CO_2 and H_2O.

The reducing power of electrons can induce the reduction of molecular oxygen (O_2) to superoxide (O_2^-). It has been confirmed that superoxide is almost as effective as the holes and hydroxyl radicals in the chain reactions for the breaking down of organic compounds.

TiO_2 has been demonstrated to be the most promising catalyst in environmental pollution removal due to its suitable bandgap and stability. The ionic pollutants in water are mostly classified into two forms: (i) metal ions such as cadmium, chromium, cobalt, arsenic, selenium, and lead; and (ii) non-metal ions such as fluoride, phosphate, nitrate, and sulfide.[243] Nanomaterials have excellent pollutant absorbent qualities,[244q] as they tend to agglomerate due to their high surface area. This leads to the reduction of active adsorption sites, which can be

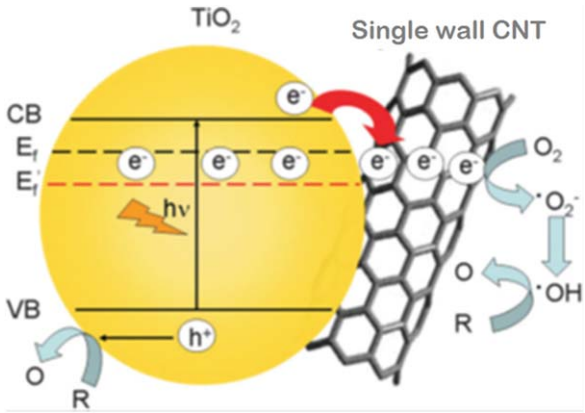

Fig. 23. The proposed mechanisms for the TiO_2–CNT heterojunction. Reprinted from reference [251]. Copyright 2014 Royal Society of Chemistry.

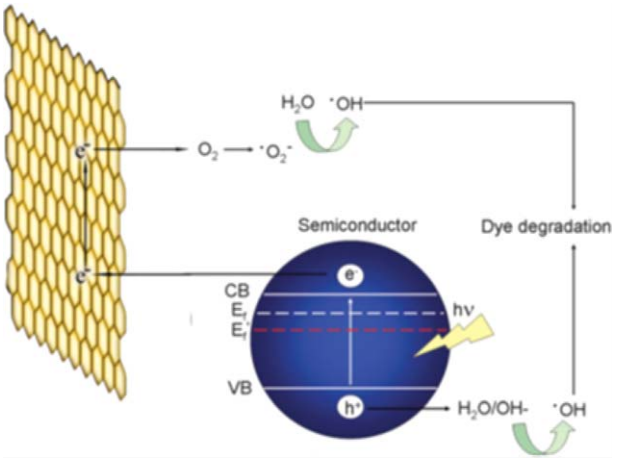

Fig. 24. The schematic structure of semiconductor–GR heterojunctions. Reprinted from reference [251]. Copyright 2014 Royal Society of Chemistry.

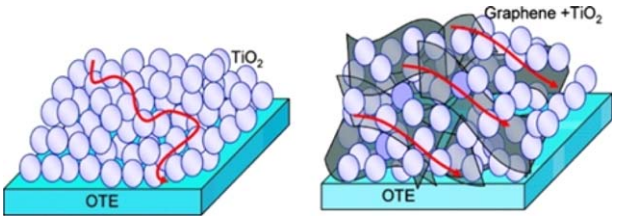

Fig. 25. Electron transport in pristine TiO_2 (left) and rGO–TiO_2 nanocomposite (right). Films cast on an optically transparent electrode (OTE). Reprinted from reference [252]. Copyright 2014 American Chemical Society.

overcome with the addition of supporting materials.[243] GR has been used as a supporting material due to its variable size, stability, and large surface area.[247] The enhancement of the photocatalytic activity of TiO_2 can be achieved through bandgap tuning, suppressing the recombination issues, and increasing the absorbency by increasing the active sites.

4.1.1. Graphene-Based TiO_2 Photocatalyst

GR or carbon–TiO_2 composites can be made via simple mixing, which is possible with pre-functionalization of surfaces. This method often failed due to poor chemical bonding.[248] The direct oxidation of Ti metals in the flame of a burner can lead to carbon doping.[249] However, the combination of semiconductors can lead to improved photocatalytic activities, which can be concluded from the Langmuir–Hinshelwood mechanism. The improved adsorption of pollutants by P25 was achieved through a GR composite. The formation of the Schottky barrier between the semiconductor and GR is an effective way to increase the recombination time. The photocatalytic mechanism proposed by Hoffmann et al. explains the enhancement of the photocatalytic properties of TiO_2–CNT composites (Figure 23).[250]

In principle, the excited photogenerated electrons in the conduction band of TiO_2 are to form the space charge regions and exchange electrons to achieve equilibrium in the Fermi levels between the semiconductor and CNT. The excited electrons participate in the oxidation, and holes in the TiO_2 can participate in the reduction reaction. GR incorporation in the TiO_2 effectively promotes charge separation and suppresses the recombination. This process generates a surface/interface for heterogeneous reactions at the interface, which leads to the enhanced catalytic activities.[251]

Figure 24 shows the electron–hole pair generation in a semiconductor, upon light illumination and electron transfer to the attached GR. The transferred electrons diffused by the dissolved oxygen, which will separate the electron–hole pair. The holes in the VB can react with surface hydroxyl to form hydroxyl radicals, which will oxidize the organic compound. As explained by Ng et al., there are enhanced electron transport properties of the TiO_2,[252] which are shown in Figure 25, and GR scaffolding in TiO_2 can increase the photocurrent generation efficiency. This will lead to the GR degradation of methylene blue (MB), methyl orange (MO), rhodamine B (RhB), phenol, butane, and 2-propanol.[253] The photocatalytic activities of TiO_2 have been enhanced by up to 3.46 times with rGO composite.[254] Wang et al. have shown the photocatalytic activities of three different nanocarbon composites such as SWCNT, C_{60}, and GR.[254] Figure 26 shows the highlights of the different types of carbon materials with P25. GR shows better performance in UV-light irradiation.

This increase in photocatalytic activity is due to the conductivity increase, which creates a more uniform distribution of nanoparticles on the GR surface compared with other nanocarbons. Zhang et al. have used a P25–rGO composite, which showed a seven times increase in visible-light photocatalytic activity.[255] The reduction of Cr(VI) with a maximum removal rate of 91% was achieved by the GR–TiO_2 composite under UV-light irradiation. Apart from this, GR–TiO_2

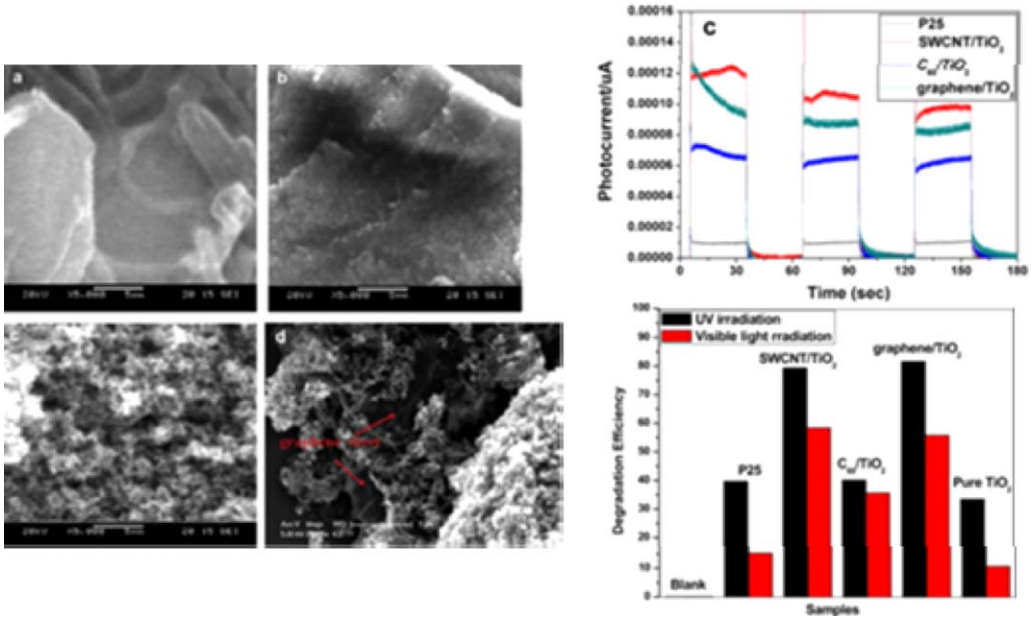

Fig. 26. (i) SEM images of nanocarbon–TiO_2 nanocomposites, (a) SWCNT–TiO_2, (b) C_{60}–TiO_2, and (c) GR–TiO_2; (d) FE-SEM image of GR–TiO_2 nanocomposites. (ii) Visible-light photoelectrochemical responses of the P25 and nanocarbon–TiO_2 nanocomposites. (iii) Photocatalytic degradation behaviors of MO over P25, as-prepared TiO_2, and nanocarbon–TiO_2 nanocomposites under UV and visible-light irradiation. Reprinted with permission from reference [254]. Copyright 2014 Elsevier Publishers.

composites with modified nanostructures have been used as removal agents in aqueous environments.[256]

Although GR–TiO_2 composites have shown the best photocatalytic properties, other semiconductors such as ZnO,[257,258] Ag/AgX (X = Br, Cl),[259] C_3N_4, ZnS, $Bi_2O_2CO_3$,[260] and Cu_2O[261] have also been studied in graphene composites to prepare photocatalysts.[262] Graphene-based hybrids were used for organic pollutant removal without using photoirradiation with iron oxide nanoparticles and chitosan.

4.2. Gas Sensor Applications

Gas sensors play an important role in detecting combustible, flammable, and toxic gases and the level of oxygen.[263] Among the reported materials for gas sensors, graphene-based gas sensors have attracted attention due to their flexible structure and properties.[264] The extensive application of graphene in gas sensors is due to the large specific surface area that can adsorb gas molecules on the surface. The gas sensitivity of graphene comes from these large specific areas that enable graphene to provide the largest sensing area per unit volume, strong covalent interactions between surface atoms and adsorbates, and high carrier mobility. The interaction between gas molecules and graphene atoms perturbs the graphene electronic system, which can be monitored with external electronic components.[263c] Interestingly, graphene has low electrical noise due to its high-quality crystal lattice arrangements that make it capable of screening more charge fluctuation. The ability of charge fluctuation screening in graphene provides a noticeable change in the conductance.[265] Graphene has been used to detect CO_2, CO, NO, NH_3, SO_2, H_2, Cl_2, NO_2, and organic vapors including acetone, benzene, and toluene.[266] Limits of gas detection as low as parts per billion have been reported for single-layer graphene using mechanical exfoliation,[265d] adhesive tape methods, and mechanically exfoliated graphene[266a] for NO_2 detection. In other studies, rGO was applied to detect chemical warfare agents, NO_2, NH_3, and Cl_2 at low ppm levels.[266c,267] Many groups have studied the potential of graphene-based materials for sensing applications using graphene nanosheets or their composites. Jung et al. have determined that the increase of temperature of the graphene surface significantly increases the sensitivity.[268] The facile wet transfer has been used to form graphene films, as shown in Figure 27.

There have been reports of graphene composites used in gas sensors. Ji et al. reported their use for toxic organic hydrocarbon detection. These toxic organic gases include hexane, cyclohexane, ethanol, acetone, benzene, pyridine, and toluene.[269] Palladium-decorated graphene, platinum–graphene nanosheet-SiC, and polyaniline–graphene have been used in NO and H_2 sensors.[270] The Pd-decorated graphene demonstrated high-speed sensitivity for NO according to Li et al.[270a] Metal oxide based graphene composites have been reported for CO, NH_3, and NO detection.[271]

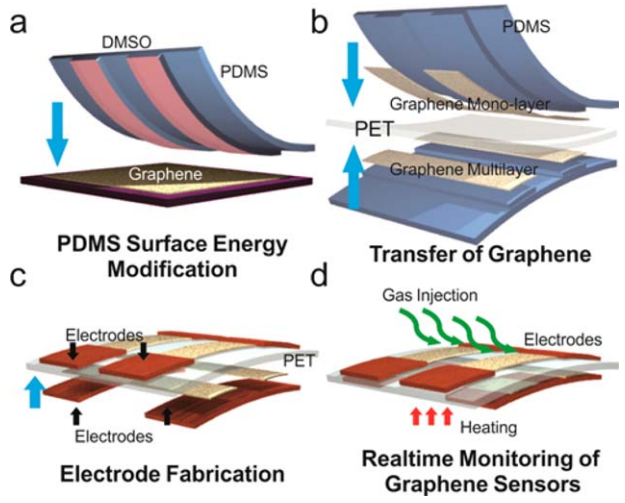

Fig. 27. (a) Schematic diagram of the facile wet transfer and soft lithography patterning of graphene films. (b) Patterned graphene was transferred to the top and bottom of the PET film to produce the graphene sensor and heater. (c) Au/Ti electrode deposited on the end of the graphene line via sputtering. (d) Sensor properties measured via gas injection and heating. Reprinted with permission from reference [268]. Copyright 2014, American Chemical Society.

4.3. Heavy-Metal-Ion Detection and Removal

Environmental contamination is often from toxic heavy-metal ions and other pollutants. Heavy-metal ions, such as arsenic (Ar), antimony (Sb), cadmium (Cd), chromium (Cr), lead (Pb), mercury (Hg), and zinc (Zn), are hazardous to human health when consumed in excess amounts or over longer periods of contact. Heavy-metal ions commonly lead to mental confusion, acute pains in joints and muscles, short-term memory loss, food intolerances/allergies, headaches, gastrointestinal upsets, etc.[272] Each element is responsible for some serious health issues related to the nervous system, cardiovascular system, kidneys, and even reproductive system.[272] In recent years, there has been a lot of interest in using carbon-related materials for the detection and removal of toxic and harmful substances from the environment, especially from water and air. CNTs have been used in various applications since the first report[273] and in environmental protection for pollutant removal from waste industrial drainage since 2010.[272] Electrochemical methods are more suitable for detecting heavy-metal ions than spectroscopic methods. They are not only simple and more sensitive, but they also have a short duration of analysis and are portable and low in cost.[274] For toxicity reasons, common hanging drop mercury electrodes,[275] or mercury electrodes,[276] are being replaced with new electrodes based on nanostructured materials. Solid-phase extraction (SPE) is popularly used in heavy-metal-ion determination based on spectrometric methods[277] and electrochemical methods.[278] The efficient way of determining the heavy-metal-ion concentration

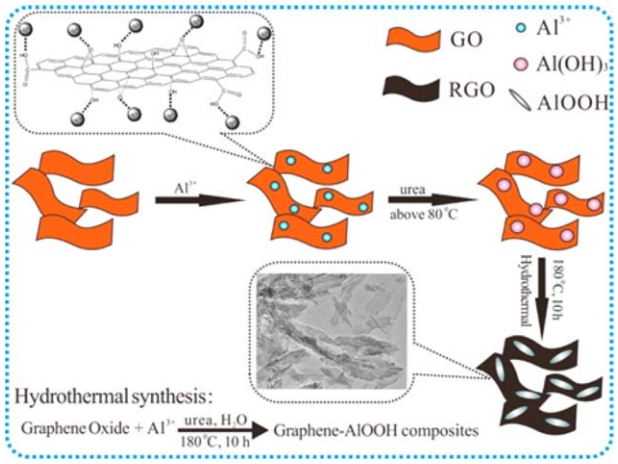

Fig. 28. Schematic of one-pot synthesis of AlOOH–rGO nanocomposites for heavy-metal-ion detection. Reprinted with permission from reference [274]. Copyright 2014, American Chemical Society.

is based on preconcentration of metal ions onto a certain substrate. This can be done with more precision through stripping voltammetry combined with SPE.[274] Graphene-based electrodes are used to determine the heavy-metal ions in place of metal oxide electrodes, where it failed due to low conductivity. The addition of graphene will increase the carrier concentration and the conduction pathways to surface electrons. Carbon nanotubes, graphite nanofibers, mesoporous carbon, and CNTs were used in electrochemical detection.[279] However, graphene showed extraordinary electronic properties. Gao et al. have used graphene with AlOOH to enhance metal-ion detection, as shown in Figure 28.[274] Graphene hybrids with aptamers[280] and cytosine-rich oligonucleotides[281] (SSO) were used for Hg^{2+} and Ag^{+} detection. Microarray and photoluminescence (PL) techniques were used to detect silver and mercury ions. However, PL sensors are selective for Hg^{2+} and Ag^{+} detection and not for Cd^{2+} and Mg^{2+} ions. Graphene-based field-effect transistors use the bipolar transport of graphene and sensitivity of Dirac point (charge neutral point) to surface charges for heavy-metal-ion detection.[282] Graphene-based FET detectors[283] are able to detect Hg^{2+} ions at 10 ppm; this increased the surface roughness to a level of 1 nm when modified with rGO and combined with metallothionein type II protein (MT-II).[284] Reduced graphene oxide functionalized with calmodulin (CaM) was used to detect Ca^{2+} and Mg^{2+} ions.[285] Sudibya et al. have explored the possibilities of using rGO-FETs as metal-ion detectors with metallothionein type II protein (MT-II) for physiological (Zn, Cu, and Se) and xenobiotic (Cd and Hg) heavy metals with high affinity.[285]

Magnetite–graphene hybrids have been used for As(III) and As(V) removal.[286] Figure 29 shows the TEM analysis of magnetite–graphene hybrids with magnetic separation from water dispersions for arsenic removal. The graphene-based

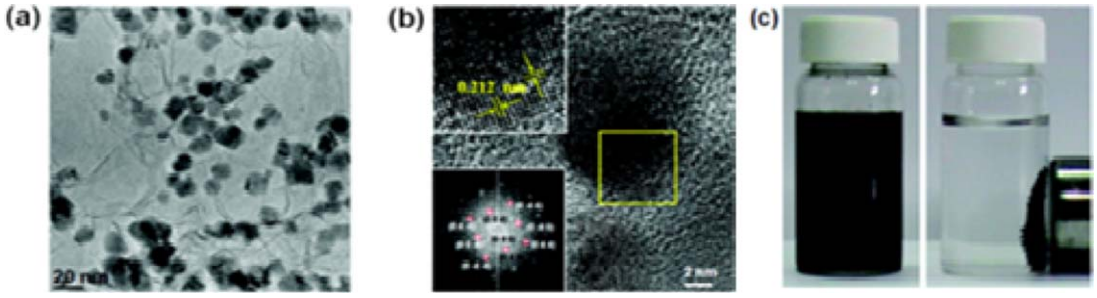

Fig. 29. (a) TEM image of Fe_3O_4–rGO. (b) HRTEM image and selected area diffraction pattern of M–rGO, where the top inset shows a close view of lattice fringes with an interlayer distance of 0.212 nm corresponding to the (400) plane. (c) M–rGO composite dispersed in water solution and magnetic separation thereof. Reprinted with permission from reference [286]. Copyright 2014, American Chemical Society.

magnetite hybrids have a higher binding capacity for As ions, which leads to 99% of As(V) removal. Chromium removal from wastewater was achieved with magnetic β-cyclodextrin–graphene oxide nanocomposites (MCGN).[287] The removal capacity was extremely fast, with a capability of more than 120 mg g^{-1}.

Graphene composites have often been used to detect and remove organic dyes, along with heavy-metal ions. The CNT-based aerogel composite with graphene was used for Pb^{2+}, Ag^{+}, and organic dyes.[288]

5. Biosensing Applications

Biosensors utilize biological or molecular recognizers and transducers to register a specific biomolecular interaction and/or the amount of target analyte. The development of simple, sensitive, and low-cost biosensing platforms with high selectivity is critical in bioanalysis. The excellent physicochemical characteristics render GR and its derivatives excellent transducing elements in bioanalysis.[18,289] For example, the existence of π-rich conjugation domains in GR facilitates the interaction between the single-stranded DNA molecules through π–π stacking interactions.[290] Also, extensive efforts have been made in analyzing the nano–bio interface of GR, and its derivatives, with various biomolecules.[291] It is shown that in a favorable environment, the immobilization of enzymes on GR and its derivatives improves enzyme stability and specificity together with prolonged enzyme functionality.[291b,292] Over the past decade, GR has become extremely popular in bioanalysis; thus, it continually brings many strategies for improving efficiency. More specifically, the high electron conductivity, large surface area, high signal-to-noise ratio due to fast heterogeneous electron transport, and low-cost production have expanded the utilization of GR in numerous vital transduction technologies including optical, electrochemical, and photoelectrochemical bioanalysis. Recent review articles have summarized the biological and chemical sensing applications of GR.[289b,293] However, in this review, from a different viewpoint, we recapitulate the great potential of GR and its derivatives towards strengthening the efficiencies of transduction methods for bioanalysis, with a particular focus on optical, electrochemical, and photoelectrochemical processes.

5.1. Optical Bioanalysis

Optical biosensors derive an analytical signal from the change in optical properties of the electrode surface upon recognizing a target biomolecule, wherein the output signal variation is proportional to the amount of the target species. Several types of optical bioanalysis, including fluorescence, electrochemiluminescence (ECL), and surface plasmon resonance, are usually used for sensing signals based on light transducers rather than collecting electrochemical signals. GR acts as a good energy acceptor in the energy transfer process due to its peculiar electronic properties.[294] Photophysical calculations confirm the feasibility of energy transfer from dyes to GR,[295] and GR can be an excellent quencher based on photoinduced electron transfer mechanisms or energy transfer mechanisms.[291b,296] Liu et al. demonstrated a one-step homogeneous fluoroimmunoassay based on GR as a powerful fluorescence acceptor, with CdTe quantum dots as donors.[297] This report, using the GR sheet, has significantly ruled out the distance limitation (10 nm) in traditional fluorescent biosensors, which extended the application of GR in the optical biosensing field.[99,101,298]

On the other hand, Zhao et al. demonstrated the fluorescence "turn-on" based detection of Pb^{2+} using the strong affinity between GR and DNAzyme, obtaining an ultralow detection limit of 300 pM for Pb^{2+}.[299] Very recently, Wang and co-workers developed a hapten-grafted GR biosensor by integrating both GR and immunoassay sensing technologies for homogeneous competitive immunoassays of small molecules.[300]

Figure 30a shows a schematic illustration of a homogeneous competitive immunoassay for bisphenol A (BPA) in water. Here, the hapten grafting enhances the antigen–antibody binding and the subsequent sandwich structure increases the quenching efficiency of the organic dye, thereby resulting in

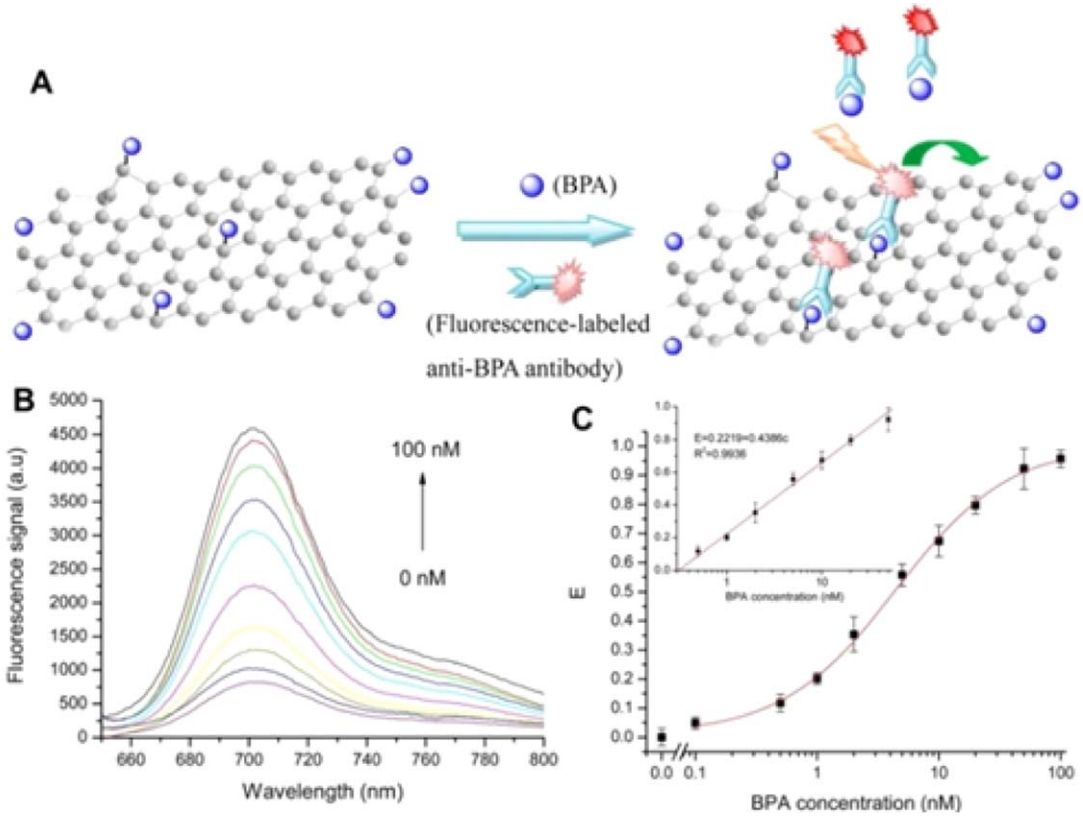

Fig. 30. (a) Schematic illustration of homogeneous competitive immunoassay for bisphenol A (BPA) in water. (b) Fluorescence spectra and (c) fluorescence-enhanced efficiency as a function of BPA concentration ranging from 0 to 100 nM. Reprinted from reference [300]. Copyright 2014 American Chemical Society.

high signal-to-background ratios. Based on the homogeneous competitive immunoassay mechanism, high BPA concentrations in the sample result in increased fluorescence signals. Figures 30b,c show the fluorescence spectra and fluorescence-enhanced efficiency as a function of BPA concentration from 0 to 100 nM. Thus, the GR-based sandwich assay shows a detection range from 0.5 to 50 nM, with a detection limit determined as 0.12 nM for BPA. Moreover, the significance of GR-based nanocomposites was further extended in surface plasmon resonance[301] based biosensors and surface-enhanced resonance Raman spectroscopy (SERS).[302]

Electrochemiluminescence gained attention for both quantitative and qualitative analysis of biomolecules due to its high sensitivity and wide dynamic range.[303] The ECL process involves an electron transfer reaction between two charged species generated on the electrode surface, which forms an excited state that emits light. Although the existing ECL-based sensors show adequate sensitivity towards biomolecular detection, the early diagnosis of ultralow-abundance biomarkers demands the development of various signal amplification strategies for improving the efficiency of ECL sensors. The signal amplification strategies in the ECL process involve improving (a) the electrode matrix, (b) the QE of the ECL species, and (c) the number of signal labels.[304] Utilization of GR as an effective matrix is an important aspect in signal amplification strategies in ECL biosensors.[305] In addition, a wide range of GR-based nanocomposites have been employed for signal amplification in ECL biosensors. By using quantum-dot-labeled GR nanocomposites as conducting bridges, an ECL immunoassay for simultaneous determination of two different tumor markers, alpha-fetoprotein (AFP) and carcinoembryonic antigen (CEA), was developed.[306] A 30-fold enhancement of the ECL intensity was achieved, resulting in ultralow-level detection of both analytes at 0.4 fM. This novel multiplexed ECL immunoassay provided a simple, sensitive, and reliable alternative for the simultaneous detection of tumor markers. In another work, 48-fold ECL amplification was attained using a carbon quantum dot (CQD) functionalized GR nanocomposite.[100] Recently, Shao et al. reported a "stretch–stowage–growth" strategy to fabricate a non-enzymatic triply amplified ECL immunosensor for ultrasensitive detection of the pseudorabies virus (PrV) antibody.[307] Figure 31 shows a schematic representation and the overall ECL response of the ECL-based immunosensors. The electrode modification involves the immobilization of AuNP–GR hybrids followed by the development of an immunoassay.[307] The interaction

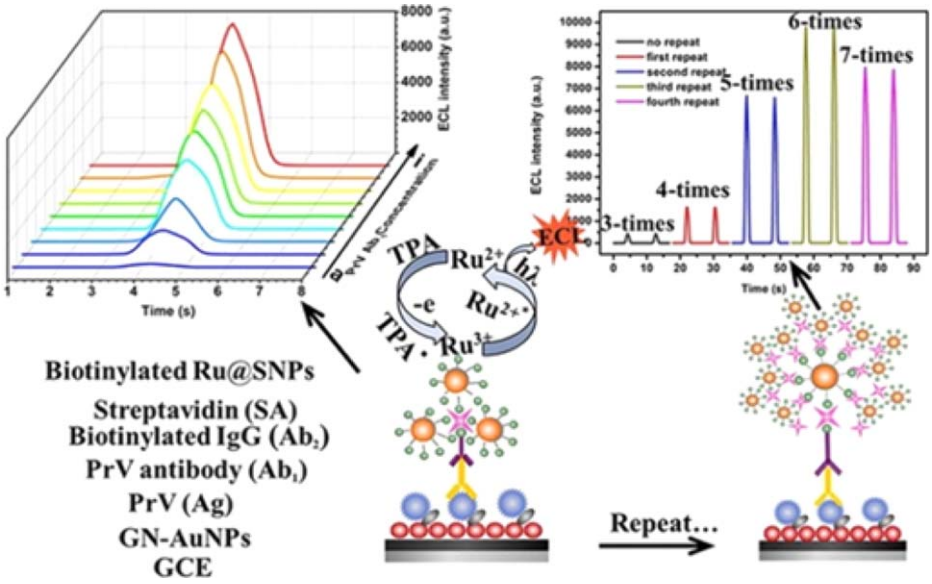

Fig. 31. Schematic illustration of ECL biosensor for detection of PrV antibody indicating the respective ECL response. Reprinted from reference [307]. Copyright 2014 American Chemical Society.

of antigen–antibody and of B–SA, the "Au–GN/PrV (Ag)/PrV antibody (Ab_1)/biotinylated-IgG (B-Ab_2)/SA/biotinylated-Ru $(bpy)_3^{2+}$-encapsulated SNPs (B–Ru@SNPs)", resulted in a triply amplified biosensor, which exhibited better analytical performance towards the monoclonal PrV antibody with a linear detection range from 50 nM to 1 pM and a detection limit of 0.40 pM.

5.2. Electrochemical Bioanalysis

Direct electron transfer (DET) between the electrode and active centers of enzymes, without using mediators or other reagents, is a fundamental process in bioelectrochemistry. However, the enzymes exhibit sluggish electron transfer ability as their redox centers are often buried deep inside the three-dimensional structure. Recently, nanomaterial-facilitated protein electron transfer has gained substantial attention, owing to the excellent electrical conductivity and tunable morphology.[308] For example, carbon-based nanostructures, especially GR, are found to facilitate the electron transfer between various redox proteins including glucose oxidase, cytochrome C (cyt C), horseradish peroxidase (HRP), and nicotinamide adenine dinucleotide (NADH), etc.[309] Zuo et al. interrogated the electron transfer between GO and heme-containing metalloproteins such as cyt C, HRP, and myoglobin (Mb).[310] Figure 32 shows a cartoon of GO-supported heme proteins on a glassy carbon electrode. The authors demonstrated that ultrahigh electron mobility and irreversible protein adsorption at the GR surface facilitated the DET, resulting in a well-defined electrochemistry of the glassy carbon electrode. From DET, it

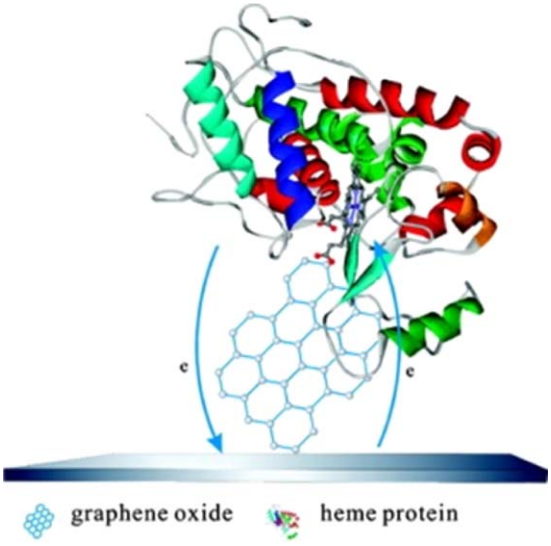

Fig. 32. Cartoon illustrating the GO-supported heme proteins immobilized on a glassy carbon electrode. Reprinted from reference [310]. Copyright 2014 American Chemical Society.

was also found that proteins remain structurally intact and retain their biological activity upon binding with GO.

Wang and his research group have developed a new electrochemical aptasensor platform for detecting adenosine triphosphate (ATP) by employing the ultrahigh electron transfer ability of GR.[311] Figure 33a shows a schematic representation of the electrochemical sensing strategy for the detection of ATP.

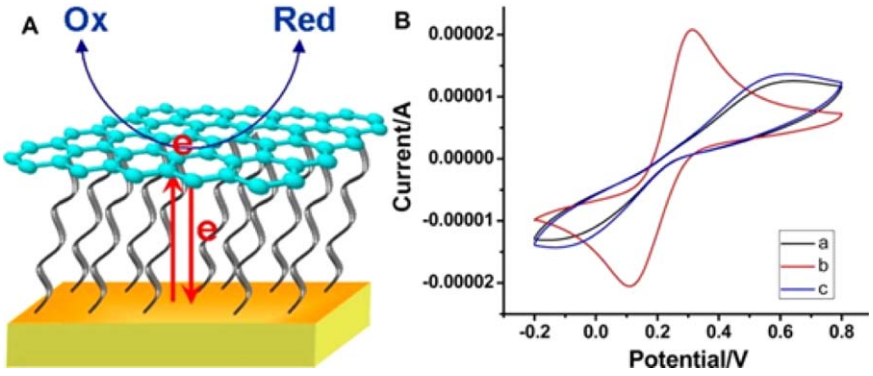

Fig. 33. (A) Schematic representation of an electrode modified with GR and ATP-binding aptamer, and (B) electrochemical response of modified electrodes (b) before and (c) after adding 2 mM ATP. Reprinted from reference [311]. Copyright 2014 American Chemical Society.

Here, an ATP-binding aptamer (ABA) is immobilized on the gold electrode, followed by binding GR through the strong π–π interaction between GR and ssDNA. This process greatly reduces the charge transfer resistance at the electrode surface. Upon adding ATP, the superior binding ability of ABA towards ATP inhibits the GR immobilization on ABA (Figure 33b). The degree of inhibition depends on the amount of ATP and, thus, a highly sensitive and selective electrochemical sensing platform with a wide dynamic range from 15×10^{-9} to 4×10^{-3} M for ATP bioanalysis was demonstrated.

Similarly, Liu et al. reported that the enzyme glucose oxidase immobilized on GO exhibited highly sensitive glucose sensing with high reproducibility and good storage stability.[312] It is well known that the electrochemical sensing of NADH and H_2O_2 is limited by the high overpotential and electrode-fouling ability. Lin et al. demonstrated that GR-modified basal and edge plane pyrolytic graphite electrodes exhibited the ability to lower the electrooxidation potentials of NADH and H_2O_2, compared to unmodified electrodes; this demonstrated the potential candidature of GR towards enhancing the electrochemical biosensing efficiency.[309a] Besides enzymatic biosensing, GR and its derivatives have been widely investigated in non-enzymatic bioanalysis. As the enzymatic biosensors show limited long-term stability, non-enzymatic bioanalysis gained a special focus. Non-enzymatic bioanalysis is based on biomolecular oxidation catalyzed by a strong electrocatalyst. GR has unusual mechanical strength, ultrahigh specific surface area, and extraordinary electrical properties, which make it an excellent electrocatalyst for biomolecular oxidation. It has been reported that functionalized GR-modified graphite electrode (FGGE) could be used for enzyme-free determination of glucose in alkaline solution.[313] Later reports showed that metal oxide nanoparticles with functionalized GO exhibited high sensitivity towards biosensing.[314] Very recently, Zhang et al. reported a GR–Pt nanocomposite as a potential candidate for H_2O_2 detection in living cells.[315]

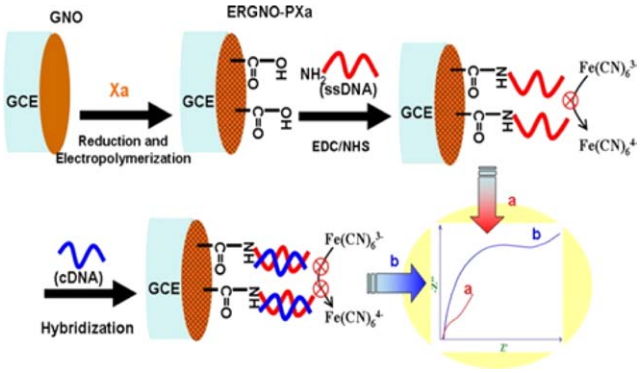

Fig. 34. Schematic representation of synchronous electrosynthesis of PXa-ERGNO for impedimetric DNA detection. Reprinted from reference [316]. Copyright 2014 American Chemical Society.

Electrochemical impedance spectroscopy (EIS) is currently one of the most sensitive electrochemical techniques for the detection of the interfacial phenomena on the surface of electrochemical sensors.[317] Yang and co-workers developed poly(xanthurenic acid) electrochemically reduced GO nanocomposite (PXa-ERGNO) modified electrodes as a potential substrate for impedimetric detection of DNA.[316] Figure 34 shows a schematic representation of the synchronous electrosynthesis of PXa-ERGNO for impedimetric DNA detection. Here, the probe ssDNA was immobilized on carboxylate PXa-ERGNO modified electrodes through forming an amide group with the probe ssDNA. This sensing platform could sensitively recognize the target DNA through EIS using an $[Fe(CN)_6]^{3-/4-}$ redox couple as a classical indicator. A dynamic detection range from 1.0×10^{-14} to 1.0×10^{-8} M with a detection limit of 4.2×10^{-15} M was obtained because of the synergistic effect of the integrated PXa-ERGNO nanocomposite. Similarly, the capabilities of GR and its derivatives were exploited for the successful detection of ethers, and other biological binding events of antigen–antibody interactions.[318]

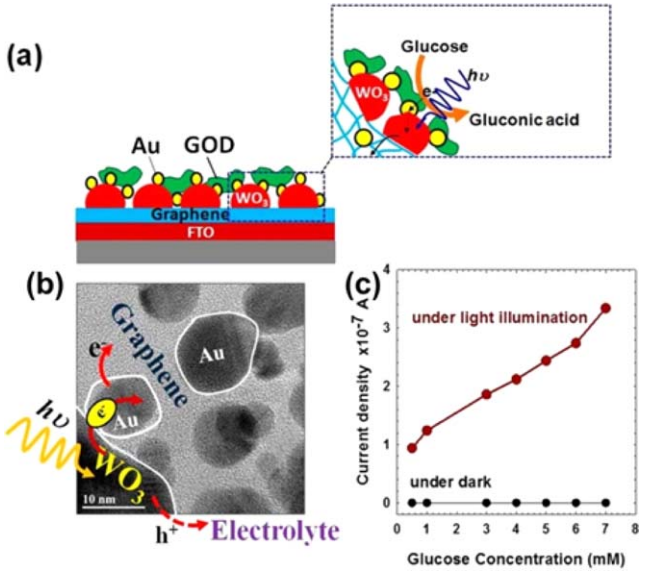

Fig. 35. (a) Scheme illustrating the PEC mechanism of glucose oxidation. (b) TEM image and (c) PEC response at GR-WO_3-Au hybrid membranes. Reprinted from reference [325]. Copyright 2014 American Chemical Society.

5.3. Photoelectrochemical Bioanalysis

The PEC process relates to the photon-to-electricity conversion resulting from charge separation and the subsequent charge transfer after absorbing photons upon illumination.[319] With the favorable charge transfer mechanism, the PEC process has become a new and promising analytical tool for the detection of biomolecules.[320] PEC sensing is a low-cost and promising analytical tool, which involves charge transfer reactions among the photoactive material, analyte, and electrode upon light irradiation. Despite the given advantages, PEC-based sensing has received rather limited attention in DNA,[321] protein,[322] and other small-molecule bioanalysis in the past decade. Zhang and co-workers reported the first PEC biosensor using functionalized GR.[323] Later, Zhao et al. reported that the CdS and folic acid co-functionalized GR can be effectively utilized for cell detection.[324] The interactions between folic acid and folate receptors on the cell surface have been utilized for the highly sensitive detection of HeLa cells.

Recently, we have reported the fabrication of GR-WO_3-Au hybrid membranes and evaluated their photocatalytic activity towards enzymatic glucose sensing.[325] Typically, metal oxide based photoelectrodes suffer from poor conductivity and charge recombination issues, which subsequently limits their PEC performance. The GR acts as an excellent conducting scaffold at the photoelectrode. Moreover, the presence of GR facilitated the electron transport and minimized the charge recombination and thus supports the enhancement of the overall PEC efficiency of the sensor. Figures 35a,b show the schematic representation of PEC glucose oxidation and the corresponding TEM image of GR-WO_3-Au hybrid membranes. Figure 35c shows the PEC response of the hybrid membranes in the dark and the light with the successive addition of glucose. The GR-WO_3-Au hybrid membranes exhibited high activity towards PEC glucose oxidation and thus opened a new avenue for the application of GR in PEC bioanalysis.

6. Conclusions and Future Prospects

Graphene, with its unique 2D structure and excellent electrical, thermal, mechanical, and optical properties, has attracted tremendous multidisciplinary research interest since its discovery in 2004. In this updated review, we have explored and summarized the exciting recent progress on the use of GR and its derivatives for PEC and photocatalytic water splitting, photocatalytic conversion for fuels, photovoltaics, supercapacitors, batteries, fuel cells, degradation of pollutants, gas sensors, heavy-metal removal, and biosensing. It is clear that the unique structural properties of graphene and its combination with semiconductors to design and fabricate novel GR-based nanocomposites have opened new doors in the fields of energy conversion, storage, environmental purification, and bioscience. Indisputably, the opportunities offered by the family of GR-based materials are exceptional and studies in this field are at the early stage. There are still numerous challenges and barriers to realize the true potential of GR-based materials for energy and environmental applications. Some of the key challenges are:

(i) Defect-controlled facile synthesis

The energy and environmental applications are highly dependent on the physicochemical properties of the materials and these properties can only be controlled through a facile synthetic strategy. Composition-, morphology-, and texture-controlled large-scale synthesis of GR-based materials is one of the key challenges that must be addressed efficiently in order to exploit the full potential of GR-based materials. The precise structure is crucial for both bandgap engineering and efficient charge transportation. GR-based materials for energy conversion, storage, and photocatalysis are mostly prepared by the chemical route in the shape of sheets. Banhart et al. have reported that some of the astonishing properties of GR can only be observed at an extremely low defect concentration and electronic, optical, thermal, and mechanical properties of GR strongly depend upon defect concentration.[326]

Zhao et al. have recently reviewed the synthetic strategies for GR materials for energy- and environment-related areas and concluded that the materials synthesized through "top-down" or "bottom-up" methods show prominent properties compared with other nanomaterials.[17b] However, there are

still many fundamental issues needing to be addressed, as the top-down synthesis often results in large amounts of defects on the graphene framework, while the bottom-up method is difficult to realize for mass production in practical applications. Thus, new cost-effective approaches for the large-scale synthesis of high-quality graphene with minimal defects or oxidation sites, and the desired composition, size, edge structure, and dimensionality, are required for practical applications.

(ii) Interfacial engineering between GR and nanoparticles

The interface engineering challenge is mostly related to synthetic methodologies. The most common approaches to prepare GR-based nanocomposites for energy, environment, and bioscience applications are based on the dispersion of semiconductor nanoparticles on the surface of GR nanosheets. Such hard integration strategies often result in weak interfacial contact between the semiconductor and GR. As discussed, the key roles of GR in solar energy conversion, photocatalysis, and electronic devices are the effective charge collection and transportation. An inadequate interfacial contact and unfavorable synergetic effect is the main cause for poor performance of the GR-based nanocomposites. Thus, the interface interaction of loaded functional nanomaterials on the GR should be improved through innovative design, by controlling the phase, porosities, surface active sites, and the structural optimization of the graphene-based nanoarchitectures.

(iii) Morphology and thickness control

GR systems with different dimensions, such as 0D GR quantum dots (GR-QDs), 1D GR nanoribbons, 2D GR sheets, and 3D porous frameworks, have specific electronic and optical properties. For example, the GR single layer is a zero-gap semiconductor with linear energy dispersion, while the GR bilayer is also a zero-gap semiconductor whose electrons obey parabolic energy dispersion. By breaking the symmetry between the two GR layers, a tunable bandgap of several hundred meV can be induced in the GR bilayer by carefully applying a gate bias.[327] Similarly, the light absorption range of GR-QDs can be tuned from UV–visible into infrared by controlling the size, geometry, and boundary conditions. Furthermore, GR-QDs have an incredible ability to convert low-energy photons into high-energy photons and a remarkably long lifetime of hot carriers, which were very effective in improving the photovoltage or photodegradation activity of the semiconductors. As discussed, the energy and environmental applications are highly dependent on the percentage of GR content in the composite. The performance of GR-based materials increases up to a certain amount of GR content and then decreases, indicating that it is important to optimize the composition, morphology, and thickness of the GR-based composite materials. Despite the recent progress on the fabrication of GR, relatively fewer efforts have been made toward the generation of GR with optimized thickness, texture, size, and shape.[328] Therefore, in order to further improve and exploit the performance of GR and GR-based nanocomposites, the fundamental issue of morphology and thickness-controlled fabrication of GR-based materials need to be addressed.

(iv) Comprehensive mechanistic study to understand the precise contribution of GR

As mentioned in this review, the strong synergic interaction between GR and the semiconductor enhances the charge collection, separation, and transfer properties of nanocomposites; however, the roles of GR have not been fully explored. Mostly, GR is discussed as the electron acceptor and transporter and its semiconducting properties are usually overlooked in composite materials, where the combination of GR results in opening the bandgap of photoactive material in the zero-bandgap GR and induces a doping effect in the carbon monolayer. GR also plays a significant role in the improvement of the electrochemical stability and catalytic activity of supported catalysts. For example, the photosensitization of GR in water splitting demonstrates a lack of direct experimental proof compared with the experimental evidence that demonstrates the role of GR as an electron acceptor. In the case of rGO/semiconductor nanocomposites, the effect of photosensitization may be from the isolated sp^2 clusters of rGO within the matrices. Thus, full understanding of the role of GR and the mechanisms of GR-based materials is subject to further exploration. Understanding the exact role and mechanism will be very helpful in designing and fabricating more efficient materials to address the energy and environmental issues.

(v) Theoretical simulation and modeling study

It is absolutely clear from the experimental results discussed in this review that GR and its derivatives play vital roles for the enhancement of solar energy conversion, storage, biosensing, and environmental purification. We also mentioned that there is scope to improve the interfacial contact between GR and semiconductor components in order to boost the overall performance of GR-based materials. However, the issue is not only related to the improved interfacial connection and enhancing the charge transfer but also requires an in-depth understanding of the inherent mechanisms behind the better performance of GR-based materials in energy and the environment, as well as in other fields of science. The current experimental methodologies do not provide enough evidence that there has been improvement in interfacial charge transfer, storage, band bending, and the role of the additional metal nanoparticles/catalysts. So along with the experimental efforts, theoretical calculations are required, as theoretical computational modeling can simulate the specific microstructures and provide comprehensive insight to the electronic properties of GR-based materials.

Furthermore, theoretical modeling is considered to be one of the most powerful tools to investigate surface and interface reactions, screen for catalysts, design new materials, engineer the electronic structures, and effect the composition and structural changes on the performance. Therefore, the combination of experimental and theoretical study would considerably improve our understanding of the role of GR at the molecular level, which will provide us with a firm guide towards designing smarter GR-based materials for potential applications.

(vi) Device fabrication, scalability, and durability

Finally, the construction of GR-based devices for energy and environmental applications is another crucial and challenging task. Few energy devices from GR-based nanocomposites work well in lab-scale tests. However, there are still many challenges that need to be addressed to realize industrial applications. The most important one is the large-scale synthesis of high-quality GR-based materials that should be electronically and chemically stable during operation. Along with the large-scale production, the development of standardized testing methods is also important for the exploration of the stability and durability of GR-based materials in device form. Environment-related applications, such as heavy-metal detection and photodegradation of organic pollutants by GR-based photocatalysts, are still in their preliminary stages when trying to envision large-scale applications. This is because there is a lack of fundamental study into the influence of GR on the ecosystem and human environment.[329] Therefore, to construct a scalable, durable, and cost-effective device, thorough efforts are required to further improve the quality of fabrication methodologies and device construction techniques to create a suitable and cost-effective device design that can be fully utilized with high performance.

Certainly, GR and its derivatives are robust materials and have great potential to address various energy and environmental issues. The interdisciplinary nature of GR-based materials, involving chemistry, physics, materials, engineering, and bioscience, makes them an exciting research avenue where challenges and opportunities coexist. Researchers around the world are progressing rapidly toward the exploration of GR-based materials, and the joint efforts and close cooperation between academia and industry will soon overcome the challenges and make a breakthrough in constructing rational devices using GR-based materials to address energy and environmental issues.

Acknowledgements

The authors would like to thank the National University of Malaysia for providing financial assistance with grant number ICONIC-2013-005.

REFERENCES

[1] V. Chabot, D. Higgins, A. Yu, X. Xiao, Z. Chen, J. Zhang, *Energy Environ. Sci.* **2014**, *7*, 1564–1596.
[2] H. W. Kroto, J. R. Heath, S. C. O'Brien, R. F. Curl, R. E. Smalley, *Nature* **1985**, *318*, 162–163.
[3] S. Iijima, *Nature* **1991**, *354*, 56–58.
[4] K. S. Novoselov, A. K. Geim, S. V. Morozov, D. Jiang, Y. Zhang, S. V. Dubonos, I. V. Grigorieva, A. A. Firsov, *Science* **2004**, *306*, 666–669.
[5] a) M. J. Allen, V. C. Tung, R. B. Kaner, *Chem. Rev.* **2010**, *110*, 132–145; b) C. N. R. Rao, A. K. Sood, K. S. Subrahmanyam, A. Govindaraj, *Angew. Chem. Int. Ed.* **2009**, *48*, 7752–7777; c) H. Chang, H. Wu, *Adv. Funct. Mater.* **2013**, *23*, 1984–1997; d) K. Yang, L. Feng, X. Shi, Z. Liu, *Chem. Soc. Rev.* **2013**, *42*, 530–547.
[6] a) A. K. Geim, *Science* **2009**, *324*, 1530–1534; b) J. C. Meyer, A. K. Geim, M. Katsnelson, K. Novoselov, T. Booth, S. Roth, *Nature* **2007**, *446*, 60–63.
[7] N. Zhang, Y. Zhang, Y.-J. Xu, *Nanoscale* **2012**, *4*, 5792–5813.
[8] M. D. Stoller, S. Park, Y. Zhu, J. An, R. S. Ruoff, *Nano Lett.* **2008**, *8*, 3498–3502.
[9] A. S. Mayorov, R. V. Gorbachev, S. V. Morozov, L. Britnell, R. Jalil, L. A. Ponomarenko, P. Blake, K. S. Novoselov, K. Watanabe, T. Taniguchi, *Nano Lett.* **2011**, *11*, 2396–2399.
[10] A. A. Balandin, *Nat. Mater.* **2011**, *10*, 569–581.
[11] X. Huang, Z. Yin, S. Wu, X. Qi, Q. He, Q. Zhang, Q. Yan, F. Boey, H. Zhang, *Small* **2011**, *7*, 1876–1902.
[12] M. F. El-Kady, V. Strong, S. Dubin, R. B. Kaner, *Science* **2012**, *335*, 1326–1330.
[13] H. Wang, L. F. Cui, Y. Yang, H. Sanchez Casalongue, J. T. Robinson, Y. Liang, Y. Cui, H. Dai, *J. Am. Chem. Soc.* **2010**, *132*, 13978–13980.
[14] F. Schedin, A. K. Geim, S. V. Morozov, E. W. Hill, P. Blake, M. I. Katsnelson, K. S. Novoselov, *Nat. Mater.* **2007**, *6*, 652–655.
[15] a) D. Chen, H. Zhang, Y. Liu, J. Li, *Energy Environ. Sci.* **2013**, *6*, 1362–1387; b) H. Chang, H. Wu, *Energy Environ. Sci.* **2013**, *6*, 3483–3507.
[16] a) Y. Sun, Q. Wu, G. Shi, *Energy Environ. Sci.* **2011**, *4*, 1113–1132; b) S. Wu, Q. He, C. Zhou, X. Qi, X. Huang, Z. Yin, Y. Yang, H. Zhang, *Nanoscale* **2012**, *4*, 2478–2483; c) Z. Yin, Q. He, X. Huang, J. Zhang, S. Wu, P. Chen, G. Lu, Q. Zhang, Q. Yan, H. Zhang, *Nanoscale* **2012**, *4*, 293–297; d) Z. Wang, J. Zhang, Z. Yin, S. Wu, D. Mandler, H. Zhang, *Nanoscale* **2012**, *4*, 2728–2733; e) Y. Zhang, T. R. Nayak, H. Hong, W. Cai, *Nanoscale* **2012**, *4*, 3833–3842.
[17] a) K. S. Kim, Y. Zhao, H. Jang, S. Y. Lee, J. M. Kim, K. S. Kim, J. H. Ahn, P. Kim, J.-Y. Choi, B. H. Hong, *Nature* **2009**, *457*, 706–710; b) G. Zhao, T. Wen, C. Chen, X. Wang, *RSC Adv.* **2012**, *2*, 9286–9303; c) Y. Hernandez, V. Nicolosi, M. Lotya, F. M. Blighe, Z. Sun, S. De, I. T. McGovern, B. Holland, M. Byrne, Y. K. Gun'Ko, J. J. Boland, P. Niraj, G. Duesberg, S. Krishnamurthy, R. Goodhue, J. Hutchison, V. Scardaci, A. C. Ferrari, J. N.

Coleman, *Nat. Nanotechnol.* **2008**, *3*, 563–568; d) S. Park, R. S. Ruoff, *Nat. Nanotechnol.* **2009**, *4*, 217–224.
[18] D. Chen, H. Feng, J. Li, *Chem. Rev.* **2012**, *112*, 6027–6053.
[19] a) L. K. Putri, W. J. Ong, W. S. Chang, S.-P. Chai, *Appl. Surf. Sci.* **2015**, *358*, 2–14; b) M. Q. Yang, C. Han, Y. J. Xu, *J. Phys. Chem. C* **2015**, *119*, 27234–27246.
[20] a) Y. Wang, J. Yu, W. Xiao, Q. Li, *J. Mater. Chem. A* **2014**, *2*, 3847–3855; b) N. Zhang, M.-Q. Yang, S. Liu, Y. Sun, Y.-J. Xu, *Chem. Rev.* **2015**, *115*, 10307–10377; c) Q. Li, H. Meng, J. Yu, W. Xiao, Y. Zheng, J. Wang, *Chem. Eur. J.* **2014**, *20*, 1176–1185.
[21] A. Geim, K. Novoselov, O. V. Yazyev, S. G. Louie, S. Ghosh, W. Bao, D. L. Nika, S. Subrina, E. P. Pokatilov, C. N. Lau, *Nat. Mater.* **2007**, *6*, 183–191.
[22] G. Eda, M. Chhowalla, *ACS Nano* **2011**, *5*, 4265–4268.
[23] L. Jiao, L. Zhang, X. Wang, G. Diankov, H. Dai, *Nature* **2009**, *458*, 877–880.
[24] A. Sinitskii, J. M. Tour, *IEEE Spectrum* **2010**, *47*, 28–33.
[25] O. V. Prezhdo, P. V. Kamat, G. C. Schatz, *J. Phys. Chem. C* **2011**, *115*, 3195–3197.
[26] a) N. Lu, Z. Li, J. Yang, *J. Phys. Chem. C* **2009**, *113*, 16741–16746; b) S. Saxena, T. A. Tyson, E. Negusse, *J. Phys. Chem. Lett.* **2010**, *1*, 3433–3437.
[27] M. J. McAllister, J. L. Li, D. H. Adamson, H. C. Schniepp, A. A. Abdala, J. Liu, M. Herrera-Alonso, D. L. Milius, R. Car, R. K. Prud'homme, I. A. Aksay, *Chem. Mater.* **2007**, *19*, 4396–4404.
[28] K. P. Loh, Q. Bao, G. Eda, M. Chhowalla, *Nat. Chem.* **2010**, *2*, 1015–1024.
[29] Y. Zhu, S. Murali, W. Cai, X. Li, J. W. Suk, J. R. Potts, R. S. Ruoff, *Adv. Mater.* **2010**, *22*, 3906–3924.
[30] C. Gómez-Navarro, R. T. Weitz, A. M. Bittner, M. Scolari, A. Mews, M. Burghard, K. Kern, *Nano Lett.* **2007**, *7*, 3499–3503.
[31] a) B. Li, L. Zhou, D. Wu, H. Peng, K. Yan, Y. Zhou, Z. Liu, *ACS Nano* **2011**, *5*, 5957–5961; b) T. Ramanathan, A. Abdala, S. Stankovich, D. Dikin, M. Herrera-Alonso, R. Piner, D. Adamson, H. Schniepp, X. Chen, R. Ruoff, *Nat. Nanotechnol.* **2008**, *3*, 327–331; c) H. Wang, Y. B. Wu, S. Gao, X. C. Liu, Q. Liu, Z.-W. Qin, S. W. Xie, L. Zhou, S.-H. Yang, *Precambrian Res.* **2013**, *230*, 13–30.
[32] L. Zhang, S. Diao, Y. Nie, K. Yan, N. Liu, B. Dai, Q. Xie, A. Reina, J. Kong, Z. Liu, *J. Am. Chem. Soc.* **2011**, *133*, 2706–2713.
[33] a) Q. Xiang, J. Yu, *J. Phys. Chem. Lett.* **2013**, *4*, 753–759; b) C. Chen, W. Cai, M. Long, B. Zhou, Y. Wu, D. Wu, Y. Feng, *ACS Nano* **2010**, *4*, 6425–6432; c) J. S. Lee, K. H. You, C. B. Park, *Adv. Mater.* **2012**, *24*, 1084–1088.
[34] L. Liao, H. Peng, Z. Liu, *J. Am. Chem. Soc.* **2014**, *136*, 12194–12200.
[35] Z. P. Huang, P. Zhong, C. F. Wang, X. X. Zhang, C. Zhang, *ACS Appl. Mater. Interfaces.* **2013**, *5*, 1961–1966.
[36] C. G. Silva, I. Luz, F. X. Llabres, A. Corma, H. Garcia, *Chem. Eur. J.* **2010**, *16*, 11133–11138.
[37] S. Sarkar, E. Bekyarova, S. Niyogi, R. C. Haddon, *J. Am. Chem. Soc.* **2011**, *133*, 3324–3327.
[38] a) D. W. Boukhvalov, M. I. Katsnelson, *J. Phys. Chem. C* **2009**, *113*, 14176–14178; b) Q. Wu, Y. Wu, Y. Hao, J. Geng, M. Charlton, S. Chen, Y. Ren, H. Ji, H. Li, D. W. Boukhvalov, *Chem. Commun.* **2012**, *49*, 677–679; c) D. W. Boukhvalov, Y. W. Son, *ChemPhysChem* **2012**, *13*, 1463–1469; d) M. A. Bissett, M. Tsuji, H. Ago, *J. Phys. Chem. C* **2013**, *117*, 3152–3159.
[39] S. Senthilarasu, F. Almonacid, T. K. Mallick, *Sol. Energy Mater. Sol. Cells* **2015**, *133*, 92–98.
[40] S. Bai, X. Shen, *RSC Adv.* **2012**, *2*, 64–98.
[41] a) M. R. Hoffmann, S. T. Martin, W. Choi, D. W. Bahnemann, *Chem. Rev.* **1995**, *95*, 69–96; b) A. Mills, R. H. Davies, D. Worsley, *Chem. Soc. Rev.* **1993**, *22*, 417–425; c) U. I. Gaya, A. H. Abdullah, *J. Photochem. Photobiol., C* **2008**, *9*, 1–12; d) S. Liu, Z. Chen, N. Zhang, Z.-R. Tang, Y.-J. Xu, *J. Phys. Chem. C* **2013**, *117*, 8251–8261.
[42] G. Xie, K. Zhang, B. Guo, Q. Liu, L. Fang, J. R. Gong, *Adv. Mater.* **2013**, *25*, 3820–3839.
[43] N. S. Lewis, *Nature* **2001**, *414*, 589–590.
[44] T. F. Yeh, J. M. Syu, C. Cheng, T. H. Chang, H. Teng, *Adv. Funct. Mater.* **2010**, *20*, 2255–2262.
[45] See reference [33a].
[46] a) J. Low, J. Yu, W. Ho, *J. Phys. Chem. Lett.* **2015**, *6*, 4244–4251; b) J. Wen, X. Li, W. Liu, Y. Fang, J. Xie, Y. Xu, *Chin. J. Catal.* **2015**, *36*, 2049–2070.
[47] M.-Q. Yang, Y.-J. Xu, *Phys. Chem. Chem. Phys.* **2013**, *15*, 19102–19118.
[48] A. Fujishima, *Nature* **1972**, *238*, 37–38.
[49] P. V. Kamat, *J. Phys. Chem. Lett.* **2012**, *3*, 663–672.
[50] a) X. Yu, R. Du, B. Li, Y. Zhang, H. Liu, J. Qu, X. An, *Appl. Catal., B* **2016**, *182*, 504–512; b) Y. Li, Y. Hu, S. Peng, G. Lu, S. Li, *J. Phys. Chem. C* **2009**, *113*, 9352–9358.
[51] X. J. Lv, W. F. Fu, H. X. Chang, H. Zhang, J. S. Cheng, G. J. Zhang, Y. Song, C.-Y. Hu, J. H. Li, *J. Mater. Chem.* **2012**, *22*, 1539–1546.
[52] X. Y. Zhang, H.-P. Li, X. L. Cui, Y. Lin, *J. Mater. Chem.* **2010**, *20*, 2801–2806.
[53] Q. Xiang, J. Yu, M. Jaroniec, *Nanoscale* **2011**, *3*, 3670–3678.
[54] X. Y. Zhang, Y. J. Sun, X. L. Cui, Z. Y. Jiang, *Int. J. Hydrogen Energy* **2012**, *37*, 811–815.
[55] P. W. Chou, Y.-S. Wang, C. C. Lin, Y. J. Chen, C. L. Cheng, M. S. Wong, *Surf. Coat. Technol.* **2009**, *204*, 834–839.
[56] W. Q. Fan, Q. H. Lai, Q. H. Zhang, Y. Wang, *J. Phys. Chem. C* **2011**, *115*, 10694–10701.
[57] H. I. Kim, G. H. Moon, D. Monllor-Satoca, Y. Park, W. Choi, *J. Phys. Chem. C* **2012**, *116*, 1535–1543.
[58] a) B. Zielińska, E. Borowiak-Palen, R. J. Kalenczuk, *Int. J. Hydrogen Energy* **2008**, *33*, 1797–1802; b) G. Liu, H. G. Yang, X. Wang, L. Cheng, J. Pan, G. Q. Lu, H. M. Cheng, *J. Am. Chem. Soc.* **2009**, *131*, 12868–12869; c) J. Yu, L. Qi, M. Jaroniec, *J. Phys. Chem. C* **2010**, *114*, 13118–13125.
[59] Y. Park, S. H. Kang, W. Choi, *Phys. Chem. Chem. Phys.* **2011**, *13*, 9425–9431.
[60] P. V. Kamat, *J. Phys. Chem. Lett.* **2009**, *1*, 520–527.
[61] Q. Xiang, B. Cheng, J. Yu, *Angew. Chem. Int. Ed.* **2015**, *54*, 11350–11366.

[62] a) Y. T. Liang, B. K. Vijayan, K. A. Gray, M. C. Hersam, *Nano Lett.* **2011**, *11*, 2865–2870; b) Y. Zhang, N. Zhang, Z. R. Tang, Y.-J. Xu, *Phys. Chem. Chem. Phys.* **2012**, *14*, 9167–9175.
[63] T. Y. Peng, K. Li, P. Zeng, Q. G. Zhang, X. G. Zhang, *J. Phys. Chem. C* **2012**, *116*, 22720–22726.
[64] Q. Li, B. D. Guo, J. G. Yu, J. R. Ran, B. H. Zhang, H. J. Yan, J. R. Gong, *J. Am. Chem. Soc.* **2011**, *133*, 10878–10884.
[65] P. Gao, J. C. Liu, S. Lee, T. Zhang, D. D. Sun, *J. Mater. Chem.* **2012**, *22*, 2292–2298.
[66] L. Jia, D.-H. Wang, Y.-X. Huang, A.-W. Xu, H.-Q. Yu, *J. Phys. Chem. C* **2011**, *115*, 11466–11473.
[67] S. Liu, B. Weng, Z.-R. Tang, Y.-J. Xu, *Nanoscale* **2015**, *7*, 861–866.
[68] J. Zhang, J. G. Yu, M. Jaroniec, J. R. Gong, *Nano Lett.* **2012**, *12*, 4584–4589.
[69] J. Zhang, L. Qi, J. Ran, J. Yu, S. Z. Qiao, *Adv. Energy Mater.* **2014**, *4*, 1301925–1301931.
[70] N. Zhang, Y.-J. Xu, *CrystEngComm* **2016**, *18*, 24–37.
[71] Q. J. Xiang, J. G. Yu, M. Jaroniec, *J. Am. Chem. Soc.* **2012**, *134*, 6575–6578.
[72] R. Ciriminna, N. Zhang, M.-Q. Yang, F. Meneguzzo, Y.-J. Xu, M. Pagliaro, *Chem. Commun.* **2015**, *51*, 7090–7095.
[73] M.-Q. Yang, N. Zhang, M. Pagliaro, Y.-J. Xu, *Chem. Soc. Rev.* **2014**, *43*, 8240–8254.
[74] J. Ding, W. Yan, W. Xie, S. Sun, J. Bao, C. Gao, *Nanoscale* **2014**, *6*, 2299–2306.
[75] A. Mukherji, B. Seger, G. Q. Lu, L. Z. Wang, *ACS Nano* **2011**, *5*, 3483–3492.
[76] J. Ding, W. Yan, S. Sun, J. Bao, C. Gao, *Int. J. Hydrogen Energy* **2014**, *39*, 119–126.
[77] A. Kudo, Y. Miseki, *Chem. Soc. Rev.* **2009**, *38*, 253–278.
[78] Y. Sasaki, H. Nemoto, K. Saito, A. Kudo, *J. Phys. Chem. C* **2009**, *113*, 17536–17542.
[79] X. Chen, S. Shen, L. Guo, S. S. Mao, *Chem. Rev.* **2010**, *110*, 6503–6570.
[80] A. Iwase, Y. H. Ng, Y. Ishiguro, A. Kudo, R. Amal, *J. Am. Chem. Soc.* **2011**, *133*, 11054–11057.
[81] Z. Yan, X. Yu, A. Han, P. Xu, P. Du, *J. Phys. Chem. C* **2014**, *118*, 22896–22903.
[82] Z. Khan, T. R. Chetia, A. K. Vardhaman, D. Barpuzary, C. V. Sastri, M. Qureshi, *RSC Adv.* **2012**, *2*, 12122–12128.
[83] J. G. Hou, Z. Wang, W. B. Kan, S. Q. Jiao, H. M. Zhu, R. V. Kumar, *J. Mater. Chem.* **2012**, *22*, 7291–7299.
[84] S. Yin, X. Wang, Z. Mou, Y. Wu, H. Huang, M. Zhu, Y. Du, P. Yang, *Phys. Chem. Chem. Phys.* **2014**, *16*, 11289–11296.
[85] Y. Hou, F. Zuo, Q. Ma, C. Wang, L. Bartels, P. Feng, *J. Phys. Chem. C* **2012**, *116*, 20132–20139.
[86] A. Kay, I. Cesar, M. Grätzel, *J. Am. Chem. Soc.* **2006**, *128*, 15714–15721.
[87] Y. H. Ng, A. Iwase, A. Kudo, R. Amal, *J. Phys. Chem. Lett.* **2010**, *1*, 2607–2612.
[88] L. Gao, F. Qu, X. Wu, *Adv. Sci., Eng. Med.* **2013**, *5*, 1485–1492.
[89] K. Zhang, X. Shi, J. K. Kim, J. S. Lee, J. H. Park, *Nanoscale* **2013**, *5*, 1939–1944.
[90] H. Wu, M. Xu, P. Da, W. Li, D. Jia, G. Zheng, *Phys. Chem. Chem. Phys.* **2013**, *15*, 16138–16142.
[91] Y. Hou, F. Zuo, A. Dagg, P. Y. Feng, *Nano Lett.* **2012**, *12*, 6464–6473.
[92] P. D. Tran, S. K. Batabyal, S. S. Pramana, J. Barber, L. H. Wong, S. C. J. Loo, *Nanoscale* **2012**, *4*, 3875–3878.
[93] A. A. Dubale, W.-N. Su, A. G. Tamirat, C.-J. Pan, B. A. Aragaw, H.-M. Chen, C.-H. Chen, B.-J. Hwang, *J. Mater. Chem. A* **2014**, *2*, 18383–18397.
[94] W. Tu, Y. Zhou, Q. Liu, Z. Tian, J. Gao, X. Chen, H. Zhang, J. Liu, Z. Zou, *Adv. Funct. Mater.* **2012**, *22*, 1215–1221.
[95] X. An, K. Li, J. Tang, *ChemSusChem* **2014**, *7*, 1086–1093.
[96] X.-J. Lv, W.-F. Fu, C.-Y. Hu, Y. Chen, W.-B. Zhou, *RSC Adv.* **2013**, *3*, 1753–1757.
[97] D. Chen, H. Zhang, Y. Liu, J. Li, *Energy Environ. Sci.* **2013**, *6*, 1362–1387.
[98] W. Bao, X. Cai, D. Kim, K. Sridhara, M. S. Fuhrer, *Appl. Phys. Lett.* **2013**, *102*, 042104.
[99] J. Zhou, G. H. Tian, Y. J. Chen, X. Y. Meng, Y. H. Shi, X. R. Cao, K. Pan, H. G. Fu, *Chem. Commun.* **2013**, *49*, 2237–2239.
[100] M. S. Zhu, Z. Li, B. Xiao, Y. T. Lu, Y. K. Du, P. Yang, X. M. Wang, *ACS Appl. Mater. Interfaces* **2013**, *5*, 1732–1740.
[101] A. H. Ye, W. Q. Fan, Q. H. Zhang, W. P. Deng, Y. Wang, *Catal. Sci. Technol.* **2012**, *2*, 969–978.
[102] Z. G. Mou, S. L. Yin, M. S. Zhu, Y. K. Du, X. M. Wang, P. Yang, J. W. Zheng, C. Lu, *Phys. Chem. Chem. Phys.* **2013**, *15*, 2793–2799.
[103] S. X. Min, G. X. Lu, *Int. J. Hydrogen Energy* **2013**, *38*, 2106–2116.
[104] S. X. Min, G. X. Lu, *Int. J. Hydrogen Energy* **2012**, *37*, 10564–10574.
[105] Z. Li, Y. J. Chen, Y. K. Du, X. M. Wang, P. Yang, J. W. Zheng, *Int. J. Hydrogen Energy* **2012**, *37*, 4880–4888.
[106] M. S. Zhu, Y. P. Dong, B. Xiao, Y. K. Du, P. Yang, X. M. Wang, *J. Mater. Chem.* **2012**, *22*, 23773–23779.
[107] See reference [92].
[108] Z. Y. Wang, B. B. Huang, Y. Dai, Y. Y. Liu, X. Y. Zhang, X. Y. Qin, J. P. Wang, Z. K. Zheng, H. F. Cheng, *CrystEngComm* **2012**, *14*, 1687–1692.
[109] See reference [51].
[110] S. X. Min, G. X. Lu, *J. Phys. Chem. C* **2012**, *116*, 25415–25424.
[111] See reference [66].
[112] A. K. Agegnehu, C. J. Pan, J. Rick, J. F. Lee, W. N. Su, B. J. Hwang, *J. Mater. Chem.* **2012**, *22*, 13849–13854.
[113] M. Latorre-Sanchez, C. Lavorato, M. Puche, V. Fornes, R. Molinari, H. Garcia, *Chem. Eur. J.* **2012**, *18*, 16774–16783.
[114] P. Zeng, Q. G. Zhang, X. G. Zhang, T. Y. Peng, *J. Alloys Compd.* **2012**, *516*, 85–90.
[115] See reference [53].
[116] Z. G. Mou, Y. P. Dong, S. J. Li, Y. K. Du, X. M. Wang, P. Yang, S. D. Wang, *Int. J. Hydrogen Energy* **2011**, *36*, 8885–8893.
[117] S. X. Min, G. X. Lu, *J. Phys. Chem. C* **2011**, *115*, 13938–13945.

[118] Q. J. Xiang, J. G. Yu, M. Jaroniec, *J. Phys. Chem. C* **2011**, *115*, 7355–7363.
[119] J. F. Shen, M. Shi, B. Yan, H. W. Ma, N. Li, M. X. Ye, *Nano Res.* **2011**, *4*, 795–806.
[120] N. Li, G. Liu, C. Zhen, F. Li, L. L. Zhang, H. M. Cheng, *Adv. Funct. Mater.* **2011**, *21*, 1717–1722.
[121] See reference [44].
[122] X. Y. Zhang, H. P. Li, X. L. Cui, *Chin. J. Inorg. Chem.* **2009**, *25*, 1903–1907.
[123] Y. G. Lin, C. K. Lin, J. T. Miller, Y. K. Hsu, Y. C. Chen, L. C. Chen, K. H. Chen, *RSC Adv.* **2012**, *2*, 11258–11262.
[124] J. Y. Kim, J. W. Jang, D. H. Youn, E. S. Kim, J. S. Lee, *RSC Adv.* **2012**, *2*, 9415–9422.
[125] P. Song, X. Y. Zhang, M. X. Sun, X. L. Cui, Y. H. Lin, *Nanoscale* **2012**, *4*, 1800–1804.
[126] See reference [44].
[127] a) T. H. Vo, M. Shekhirev, D. A. Kunkel, M. D. Morton, E. Berglund, L. Kong, P. M. Wilson, P. A. Dowben, A. Enders, A. Sinitskii, *Nat. Commun.* **2014**, *5*, 3189–3198; b) L. Gao, G.-X. Ni, Y. Liu, B. Liu, A. H. Castro Neto, K. P. Loh, *Nature* **2014**, *505*, 190–194; c) Y. P. Chen, Q. Yu, *Nat. Nanotechnol.* **2010**, *5*, 559–560.
[128] a) Y. Chen, B. Zhang, G. Liu, X. Zhuang, E.-T. Kang, *Chem. Soc. Rev.* **2012**, *41*, 4688–4707; b) H. Liu, Y. Liu, D. Zhu, *J. Mater. Chem.* **2011**, *21*, 3335–3345; c) L. Lai, J. R. Potts, D. Zhan, L. Wang, C. K. Poh, C. Tang, H. Gong, Z. Shen, J. Lin, R. S. Ruoff, *Energy Environ. Sci.* **2012**, *5*, 7936–7942; d) S. Das, P. Sudhagar, E. Ito, D.-y. Lee, S. Nagarajan, S. Y. Lee, Y. S. Kang, W. Choi, *J. Mater. Chem.* **2012**, *22*, 20490–20497.
[129] a) S. Das, P. Sudhagar, Y. S. Kang, W. Choi, *J. Mater. Res.* **2014**, *29*, 299–319; b) Z. Yin, J. Zhu, Q. He, X. Cao, C. Tan, H. Chen, Q. Yan, H. Zhang, *Adv. Energy Mater.* **2014**, *4*, 1–19; c) J. D. Roy-Mayhew, I. A. Aksay, *Chem. Rev.* **2014**, *114*, 6323–6348; d) H. Tang, C. M. Hessel, J. Wang, N. Yang, R. Yu, H. Zhao, D. Wang, *Chem. Soc. Rev.* **2014**, *43*, 4281–4299.
[130] B. O'Regan, M. Gratzel, *Nature* **1991**, *353*, 737–740.
[131] S. Mathew, A. Yella, P. Gao, R. Humphry-Baker, B. F. E. Curchod, N. Ashari-Astani, I. Tavernelli, U. Rothlisberger, Md. K. Nazeeruddin, M. Grätzel, *Nat. Chem.* **2014**, *6*, 242–247.
[132] A. Hagfeldt, G. Boschloo, L. Sun, L. Kloo, H. Pettersson, *Chem. Rev.* **2010**, *110*, 6595–6663.
[133] R. R. Nair, P. Blake, A. N. Grigorenko, K. S. Novoselov, T. J. Booth, T. Stauber, N. M. R. Peres, A. K. Geim, *Science* **2008**, *320*, 1308.
[134] K. Ellmer, *Nat. Photonics* **2012**, *6*, 809–817.
[135] X. Wang, L. Zhi, K. Müllen, *Nano Lett.* **2007**, *8*, 323–327.
[136] G. S. Selopal, R. Milan, L. Ortolani, V. Morandi, R. Rizzoli, G. Sberveglieri, G. P. Veronese, A. Vomiero, I. Concina, *Sol. Energy Mater. Sol. Cells*, **2015**, *135*, 99–105.
[137] L. M. Peter, *Phys. Chem. Chem. Phys.* **2007**, *9*, 2630–2642.
[138] a) Y. B. Tang, C. S. Lee, J. Xu, Z. T. Liu, Z. H. Chen, Z. He, Y. L. Cao, G. Yuan, H. Song, L. Chen, L. Luo, H. M. Cheng, W. J. Zhang, I. Bello, S. T. Lee, *ACS Nano* **2010**, *4*, 3482–3488; b) J. Song, Z. Yin, Z. Yang, P. Amaladass, S. Wu, J. Ye, Y. Zhao, W. Q. Deng, H. Zhang, X. W. Liu, *Chem. Eur. J.* **2011**, *17*, 10832–10837; c) N. J. Bell, Y. H. Ng, A. Du, H. Coster, S. C. Smith, R. Amal, *J. Phys. Chem. C* **2011**, *115*, 6004–6009.
[139] T. Chen, W. Hu, J. Song, G. H. Guai, C. M. Li, *Adv. Funct. Mater.* **2012**, *22*, 5245–5250.
[140] B. Tang, G. Hu, *J. Power Sources* **2012**, *220*, 95–102.
[141] C. Y. Neo, J. Ouyang, *J. Power Sources* **2013**, *222*, 161–168.
[142] a) M. Zhu, X. Li, W. Liu, Y. Cui, *J. Power Sources* **2014**, *262*, 349–355; b) J. Chang, J. Yang, P. Ma, D. Wu, L. Tian, Z. Gao, K. Jiang, L. Yang, *J. Colloid Interface Sci.* **2013**, *394*, 231–236; c) J. Fan, S. Liu, J. Yu, *J. Mater. Chem.* **2012**, *22*, 17027–17036.
[143] G. Khurana, S. Sahoo, S. K. Barik, R. S. Katiyar, *J. Alloys Compd.* **2013**, *578*, 257–260.
[144] S. Sun, L. Gao, Y. Liu, *Appl. Phys. Lett.* **2010**, *96*.
[145] a) See reference [52]; b) X. Xin, X. Zhou, J. Wu, X. Yao, Z. Liu, *ACS Nano* **2012**, *6*, 11035–11043.
[146] See reference [138b].
[147] H. Wang, S. L. Leonard, Y. H. Hu, *Ind. Eng. Chem. Res.* **2012**, *51*, 10613–10620.
[148] Z. Chen, W. Ren, L. Gao, B. Liu, S. Pei, H.-M. Cheng, *Nat. Mater.* **2011**, *10*, 424–428.
[149] P. M. Sudeep, T. N. Narayanan, A. Ganesan, M. M. Shaijumon, H. Yang, S. Ozden, P. K. Patra, M. Pasquali, R. Vajtai, S. Ganguli, A. K. Roy, M. R. Anantharaman, P. M. Ajayan, *ACS Nano* **2013**, *7*, 7034–7040.
[150] Z. He, H. Phan, J. Liu, T.-Q. Nguyen, T. T. Y. Tan, *Adv. Mater.* **2013**, *25*, 6900–6904.
[151] N. Yang, J. Zhai, D. Wang, Y. Chen, L. Jiang, *ACS Nano* **2010**, *4*, 887–894.
[152] a) C. Li, G. Shi, *Nanoscale* **2012**, *4*, 5549–5563; b) X. Cao, Z. Yin, H. Zhang, *Energy Environ. Sci.* **2014**, *7*, 1850–1865.
[153] J. Du, X. Lai, N. Yang, J. Zhai, D. Kisailus, F. Su, D. Wang, L. Jiang, *ACS Nano* **2010**, *5*, 590–596.
[154] H.-N. Kim, H. Yoo, J. H. Moon, *Nanoscale* **2013**, *5*, 4200–4204.
[155] B. Tang, G. Hu, H. Gao, Z. Shi, *J. Power Sources* **2013**, *234*, 60–68.
[156] a) J.-H. Yum, E. Baranoff, S. Wenger, M. K. Nazeeruddin, M. Gratzel, *Energy Environ. Sci.* **2011**, *4*, 842–857; b) C. H. Lee, S. A. Kim, M. R. Jung, K.-S. Ahn, Y. S. Han, J. H. Kim, *Jpn. J. Appl. Phys.* **2014**, *53*, 08NC04.
[157] A. Kongkanand, K. Tvrdy, K. Takechi, M. Kuno, P. V. Kamat, *J. Am. Chem. Soc.* **2008**, *130*, 4007–4015.
[158] P. Sudhagar, E. Juárez-Pérez, Y. Kang, I. Mora-Seró, in *Low-Cost Nanomaterials* (Eds.: Z. Lin, J. Wang), Springer, London, **2014**, pp. 89–136.
[159] a) A. J. Nozik, M. C. Beard, J. M. Luther, M. Law, R. J. Ellingson, J. C. Johnson, *Chem. Rev.* **2010**, *110*, 6873–6890; b) J. B. Sambur, T. Novet, B. A. Parkinson, *Science* **2010**, *330*, 63–66.
[160] Z. Pan, I. Mora-Seró, Q. Shen, H. Zhang, Y. Li, K. Zhao, J. Wang, X. Zhong, J. Bisquert, *J. Am. Chem. Soc.* **2014**, *136*, 9203–9210.
[161] G. Hodes, *J. Phys. Chem. C* **2008**, *112*, 17778–17787.

[162] I. Hod, V. González-Pedro, Z. Tachan, F. Fabregat-Santiago, I. Mora-Seró, J. Bisquert, A. Zaban, *J. Phys. Chem. Lett.* **2011**, *2*, 3032–3035.

[163] a) P. Sudhagar, V. Gonzalez-Pedro, I. Mora-Sero, F. Fabregat-Santiago, J. Bisquert, Y. S. Kang, *J. Mater. Chem.* **2012**, *22*, 14228–14235; b) P. Sudhagar, J. H. Jung, S. Park, Y.-G. Lee, R. Sathyamoorthy, Y. S. Kang, H. Ahn, *Electrochem. Commun.* **2009**, *11*, 2220–2224.

[164] a) P. Sudhagar, T. Song, D. H. Lee, I. Mora-Seró, J. Bisquert, M. Laudenslager, W. M. Sigmund, W. I. Park, U. Paik, Y. S. Kang, *J. Phys. Chem. Lett.* **2011**, *2*, 1984–1990; b) H. Han, P. Sudhagar, T. Song, Y. Jeon, I. Mora-Sero, F. Fabregat-Santiago, J. Bisquert, Y. S. Kang, U. Paik, *Chem. Commun.* **2013**, *49*, 2810–2812.

[165] C. X. Guo, H. B. Yang, Z. M. Sheng, Z. S. Lu, Q. L. Song, C. M. Li, *Angew. Chem. Int. Ed.* **2010**, *49*, 3014–3017.

[166] P. K. Santra, P. V. Kamat, *J. Am. Chem. Soc.* **2012**, *135*, 877–885.

[167] H. Yang, C. Guo, G. H. Guai, Q. Song, S. P. Jiang, C. M. Li, *ACS Appl. Mater. Interfaces* **2011**, *3*, 1940–1945.

[168] J. Chen, F. Xu, J. Wu, K. Qasim, Y. Zhou, W. Lei, L.-T. Sun, Y. Zhang, *Nanoscale* **2012**, *4*, 441–443.

[169] I. V. Lightcap, P. V. Kamat, *J. Am. Chem. Soc.* **2012**, *134*, 7109–7116.

[170] J. Chen, C. Li, G. Eda, Y. Zhang, W. Lei, M. Chhowalla, W. I. Milne, W.-Q. Deng, *Chem. Commun.* **2011**, *47*, 6084–6086.

[171] a) Y. Lin, K. Zhang, W. Chen, Y. Liu, Z. Geng, J. Zeng, N. Pan, L. Yan, X. Wang, J. G. Hou, *ACS Nano* **2010**, *4*, 3033–3038; b) S. Kundu, S. Sadhu, R. Bera, B. Paramanik, A. Patra, *J. Phys. Chem. C* **2013**, *117*, 23987–23995; c) X.-Y. Yu, Z.-H. Chen, D.-B. Kuang, C.-Y. Su, *ChemPhysChem* **2012**, *13*, 2654–2658.

[172] A. Cao, Z. Liu, S. Chu, M. Wu, Z. Ye, Z. Cai, Y. Chang, S. Wang, Q. Gong, Y. Liu, *Adv. Mater.* **2010**, *22*, 103–106.

[173] M.-H. Jung, M.-J. Chu, *Nanoscale* **2014**, *6*, 9241–9249.

[174] N. Papageorgiou, *Coord. Chem. Rev.* **2004**, *248*, 1421–1446.

[175] H. Choi, H. Kim, S. Hwang, Y. Han, M. Jeon, *J. Mater. Chem.* **2011**, *21*, 7548–7551.

[176] M. J. Ju, J. C. Kim, H.-J. Choi, I. T. Choi, S. G. Kim, K. Lim, J. Ko, J.-J. Lee, I.-Y. Jeon, J.-B. Baek, H. K. Kim, *ACS Nano* **2013**, *7*, 5243–5250.

[177] a) S. Das, P. Sudhagar, V. Verma, D. Song, E. Ito, S. Y. Lee, Y. S. Kang, W. Choi, *Adv. Funct. Mater.* **2011**, *21*, 3729–3736; b) J. D. Roy-Mayhew, D. J. Bozym, C. Punckt, I. A. Aksay, *ACS Nano* **2010**, *4*, 6203–6211.

[178] S. Das, P. Sudhagar, S. Nagarajan, E. Ito, S. Y. Lee, Y. S. Kang, W. Choi, *Carbon* **2012**, *50*, 4815–4821.

[179] a) K. S. Lee, Y. Lee, J. Y. Lee, J.-H. Ahn, J. H. Park, *ChemSusChem* **2012**, *5*, 379–382; b) L. Qiu, H. Zhang, W. Wang, Y. Chen, R. Wang, *Appl. Surf. Sci.* **2014**, *319*, 339–343.

[180] M. Al-Mamun, J.-Y. Kim, Y.-E. Sung, J.-J. Lee, S.-R. Kim, *Chem. Phys. Lett.* **2013**, *561–562*, 115–119.

[181] P. Sudhagar, E. Ramasamy, W.-H. Cho, J. Lee, Y. S. Kang, *Electrochem. Commun.* **2011**, *13*, 34–37.

[182] a) J. G. Radich, R. Dwyer, P. V. Kamat, *J. Phys. Chem. Lett.* **2011**, *2*, 2453–2460; b) M. Ye, C. Chen, N. Zhang, X. Wen, W. Guo, C. Lin, *Adv. Energy Mater.* **2014**, *4*, 1301564; c) P. Parand, M. Samadpour, A. Esfandiar, A. Iraji Zad, *ACS Photonics* **2014**, *1*, 323–330.

[183] K. F. Mak, M. Y. Sfeir, Y. Wu, C. H. Lui, J. A. Misewich, T. F. Heinz, *Phys. Rev. Lett.* **2008**, *101*, 196405.

[184] X. T. Zheng, A. Than, A. Ananthanaraya, D.-H. Kim, P. Chen, *ACS Nano* **2013**, *7*, 6278–6286.

[185] a) Q. Liu, B. Guo, Z. Rao, B. Zhang, J. R. Gong, *Nano Lett.* **2013**, *13*, 2436–2441; b) S. Zhu, J. Zhang, C. Qiao, S. Tang, Y. Li, W. Yuan, B. Li, L. Tian, F. Liu, R. Hu, H. Gao, H. Wei, H. Zhang, H. Sun, B. Yang, *Chem. Commun.* **2011**, *47*, 6858–6860.

[186] X. Yan, X. Cui, L. S. Li, *J. Am. Chem. Soc.* **2010**, *132*, 5944–5945.

[187] L. Wang, Y. Wang, T. Xu, H. Liao, C. Yao, Y. Liu, Z. Li, Z. Chen, D. Pan, L. Sun, M. Wu, *Nat. Commun.* **2014**, *5*, 1–9.

[188] M. A. Sk, A. Ananthanarayanan, L. Huang, K. H. Lim, P. Chen, *J. Mater. Chem. C* **2014**, *2*, 6954–6960.

[189] Y. Li, Y. Zhao, H. Cheng, Y. Hu, G. Shi, L. Dai, L. Qu, *J. Am. Chem. Soc.* **2011**, *134*, 15–18.

[190] J. Ge, M. Lan, B. Zhou, W. Liu, L. Guo, H. Wang, Q. Jia, G. Niu, X. Huang, H. Zhou, X. Meng, P. Wang, C. S. Lee, W. Zhang, X. Han, *Nat. Commun.* **2014**, *5*, 1–8.

[191] Z. Zhang, J. Zhang, N. Chen, L. Qu, *Energy Environ. Sci.* **2012**, *5*, 8869–8890.

[192] S. H. Jin, D. H. Kim, G. H. Jun, S. H. Hong, S. Jeon, *ACS Nano* **2012**, *7*, 1239–1245.

[193] X. Yan, X. Cui, B. Li, L. S. Li, *Nano Lett.* **2010**, *10*, 1869–1873.

[194] L. S. Li, X. Yan, *J. Phys. Chem. Lett.* **2010**, *1*, 2572–2576.

[195] I. P. Hamilton, B. Li, X. Yan, L. S. Li, *Nano Lett.* **2011**, *11*, 1524–1529.

[196] X. Yan, B. Li, L.-S. Li, *Acc. Chem. Res.* **2012**, *46*, 2254–2262.

[197] K. J. Williams, C. A. Nelson, X. Yan, L.-S. Li, X. Zhu, *ACS Nano* **2013**, *7*, 1388–1394.

[198] Z. Ji, R. Wu, L. Adamska, K. A. Velizhanin, S. K. Doorn, M. Sykora, *ACS Appl. Mater. Interfaces* **2014**, *6*, 20473–20478.

[199] X. Fang, M. Li, K. Guo, J. Li, M. Pan, L. Bai, M. Luoshan, X. Zhao, *Electrochim. Acta* **2014**, *137*, 634–638.

[200] a) P. Lian, X. Zhu, S. Liang, Z. Li, W. Yang, H. Wang, *Electrochim. Acta* **2010**, *55*, 3909–3914; b) P. Guo, H. Song, X. Chen, *Electrochem. Commun.* **2009**, *11*, 1320–1324.

[201] M. Liang, L. Zhi, *J. Mater. Chem.* **2009**, *19*, 5871–5878.

[202] a) S.-M. Paek, E. Yoo, I. Honma, *Nano Lett.* **2008**, *9*, 72–75; b) D. Pan, S. Wang, B. Zhao, M. Wu, H. Zhang, Y. Wang, Z. Jiao, *Chem. Mater.* **2009**, *21*, 3136–3142; c) C. Uthaisar, V. Barone, *Nano Lett.* **2010**, *10*, 2838–2842.

[203] Z.-S. Wu, W. Ren, L. Xu, F. Li, H.-M. Cheng, *ACS Nano* **2011**, *5*, 5463–5471.

[204] a) G. Zhou, D.-W. Wang, F. Li, L. Zhang, N. Li, Z.-S. Wu, L. Wen, G. Q. Lu, H.-M. Cheng, *Chem. Mater.* **2010**, *22*, 5306–5313; b) E. Yoo, J. Kim, E. Hosono, H.-s. Zhou, T. Kudo, I. Honma, *Nano Lett.* **2008**, *8*, 2277–2282; c) X. Wang, X. Zhou, K. Yao, J. Zhang, Z. Liu, *Carbon* **2011**, *49*, 133–139.

[205] a) J. Zhu, T. Zhu, X. Zhou, Y. Zhang, X. W. Lou, X. Chen, H. Zhang, H. H. Hng, Q. Yan, *Nanoscale* **2011**, *3*, 1084–

1089; b) D. Wang, D. Choi, J. Li, Z. Yang, Z. Nie, R. Kou, D. Hu, C. Wang, L. V. Saraf, J. Zhang, *ACS Nano* **2009**, *3*, 907–914; c) Z.-S. Wu, W. Ren, L. Wen, L. Gao, J. Zhao, Z. Chen, G. Zhou, F. Li, H.-M. Cheng, *ACS Nano* **2010**, *4*, 3187–3194; d) S. Yang, X. Feng, S. Ivanovici, K. Müllen, *Angew. Chem. Int. Ed.* **2010**, *49*, 8408–8411.

[206] W. Zhou, J. Zhu, C. Cheng, J. Liu, H. Yang, C. Cong, C. Guan, X. Jia, H. J. Fan, Q. Yan, *Energy Environ. Sci.* **2011**, *4*, 4954–4961.

[207] Y.-T. Xu, Y. Guo, C. Li, X.-Y. Zhou, M. C. Tucker, X.-Z. Fu, R. Sun, C.-P. Wong, *Nano Energy*, **2015**, *11*, 38–47

[208] H. Kim, K.-Y. Park, J. Hong, K. Kang, *Sci. Rep.* **2014**, *4*, 1–8.

[209] L. Li, A. R. O. Raji, J. M. Tour, *Adv. Mater.* **2013**, *25*, 6298–6302.

[210] X.-C. Dong, H. Xu, X.-W. Wang, Y.-X. Huang, M. B. Chan-Park, H. Zhang, L.-H. Wang, W. Huang, P. Chen, *ACS Nano* **2012**, *6*, 3206–3213.

[211] J. Zhu, D. Yang, Z. Yin, Q. Yan, H. Zhang, *Small* **2014**, *10*, 3480–3498.

[212] H. Liu, P. Gao, J. Fang, G. Yang, *Chem. Commun.* **2011**, *47*, 9110–9112.

[213] C. Su, X. Bu, L. Xu, J. Liu, C. Zhang, *Electrochim. Acta* **2012**, *64*, 190–195.

[214] a) J. Yang, J. Wang, D. Wang, X. Li, D. Geng, G. Liang, M. Gauthier, R. Li, X. Sun, *J. Power Sources* **2012**, *208*, 340–344; b) S.-M. Bak, K.-W. Nam, C.-W. Lee, K.-H. Kim, H.-C. Jung, X.-Q. Yang, K.-B. Kim, *J. Mater. Chem.* **2011**, *21*, 17309–17315.

[215] H. Wang, Y. Yang, Y. Liang, L. F. Cui, H. Sanchez Casalongue, Y. Li, G. Hong, Y. Cui, H. Dai, *Angew. Chem. Int. Ed.* **2011**, *50*, 7364–7368.

[216] S. Yang, Y. Gong, Z. Liu, L. Zhan, D. P. Hashim, L. Ma, R. Vajtai, P. M. Ajayan, *Nano Lett.* **2013**, *13*, 1596–1601.

[217] J. W. Lee, S. Y. Lim, H. M. Jeong, T. H. Hwang, J. K. Kang, J. W. Choi, *Energy Environ. Sci.* **2012**, *5*, 9889–9894.

[218] a) J. Qu, Y. Shen, X. Qu, S. Dong, *Chem. Commun.* **2004**, 34–35; b) S. Golabi, A. Nozad, *J. Electroanal. Chem.* **2002**, *521*, 161–167.

[219] C. Wang, M. Waje, X. Wang, J. M. Tang, R. C. Haddon, Y. Yan, *Nano Lett.* **2004**, *4*, 345–348.

[220] R. Kou, Y. Shao, D. Wang, M. H. Engelhard, J. H. Kwak, J. Wang, V. V. Viswanathan, C. Wang, Y. Lin, Y. Wang, *Electrochem. Commun.* **2009**, *11*, 954–957.

[221] a) D. Chen, L. Tang, J. Li, *Chem. Soc. Rev.* **2010**, *39*, 3157–3180; b) L. Qu, Y. Liu, J.-B. Baek, L. Dai, *ACS Nano* **2010**, *4*, 1321–1326.

[222] N. Alexeyeva, T. Laaksonen, K. Kontturi, F. Mirkhalaf, D. J. Schiffrin, K. Tammeveski, *Electrochem. Commun.* **2006**, *8*, 1475–1480.

[223] D. A. Brownson, C. E. Banks, *Analyst* **2010**, *135*, 2768–2778.

[224] R. I. Jafri, N. Rajalakshmi, S. Ramaprabhu, *J. Mater. Chem.* **2010**, *20*, 7114–7117.

[225] S. Zhang, Y. Shao, X. Li, Z. Nie, Y. Wang, J. Liu, G. Yin, Y. Lin, *J. Power Sources* **2010**, *195*, 457–460.

[226] K. Kakaei, M. Zhiani, *J. Power Sources* **2013**, *225*, 356–363.

[227] Y. Xin, J.-g. Liu, Y. Zhou, W. Liu, J. Gao, Y. Xie, Y. Yin, Z. Zou, *J. Power Sources* **2011**, *196*, 1012–1018.

[228] P. Simon, Y. Gogotsi, *Nat. Mater.* **2008**, *7*, 845–854.

[229] J. Xia, F. Chen, J. Li, N. Tao, *Nat. Nanotechnol.* **2009**, *4*, 505–509.

[230] W. Lv, D.-M. Tang, Y.-B. He, C.-H. You, Z.-Q. Shi, X.-C. Chen, C.-M. Chen, P.-X. Hou, C. Liu, Q.-H. Yang, *ACS Nano* **2009**, *3*, 3730–3736.

[231] S. Stankovich, D. A. Dikin, R. D. Piner, K. A. Kohlhaas, A. Kleinhammes, Y. Jia, Y. Wu, S. T. Nguyen, R. S. Ruoff, *Carbon* **2007**, *45*, 1558–1565.

[232] G. Yu, L. Hu, M. Vosgueritchian, H. Wang, X. Xie, J. R. McDonough, X. Cui, Y. Cui, Z. Bao, *Nano Lett.* **2011**, *11*, 2905–2911.

[233] M. Xue, F. Li, J. Zhu, H. Song, M. Zhang, T. Cao, *Adv. Funct. Mater.* **2012**, *22*, 1284–1290.

[234] Y. Xu, Z. Lin, X. Zhong, X. Huang, N. O. Weiss, Y. Huang, X. Duan, *Nat. Commun.* **2014**, *5*, 1–8.

[235] Z. Bo, W. Zhu, W. Ma, Z. Wen, X. Shuai, J. Chen, J. Yan, Z. Wang, K. Cen, X. Feng, *Adv. Mater.* **2013**, *25*, 5799–5806.

[236] See reference [215b].

[237] T. Y. Kim, H. W. Lee, M. Stoller, D. R. Dreyer, C. W. Bielawski, R. S. Ruoff, K. S. Suh, *ACS Nano* **2010**, *5*, 436–442.

[238] a) A. A. Adeyemo, I. O. Adeoye, O. S. Bello, *Toxicol. Environ. Chem.* **2012**, *94*, 1846–1863; b) G. Liu, X. Li, J. Zhao, H. Hidaka, N. Serpone, *Environ. Sci. Technol.* **2000**, *34*, 3982–3990; c) E. W. George, L. Baughman, *Environ. Sci. Technol.* **1994**, *28*, 267–276; d) A. P. Janez, *Catal. Today* **2007**, *124*, 172–184; e) X. Lv, Y.-Q. Zhang, G. Guo, *Energy Environ. Sci.* **2014**, *7*, 2831–2867; f) X. Fu, Y.-J. Xu, *ACS Nano* **2010**, *4*, 7303–7314.

[239] M. A. Ali, T. A. Khan, *J. Environ. Manage.* **2012**, *113*, 170–183.

[240] N. Zhang, Y.-J. Xu, *Nanoscale* **2015**, *7*, 18062–18070.

[241] a) M. N. Chong, C. W. Chow, C. Saint, *Water Resour.* **2010**, *44*, 2997–3027; b) D. H. Bremner, R. Molina, F. Martínez, J. A. Melero, Y. Segura, *Appl. Catal., B* **2009**, *90*, 380–388.

[242] A. Dabrowski, *Adv. Colloid Interface Sci.* **2001**, *93*, 135–224.

[243] K. C. Kemp, H. Seema, M. Saleh, N. H. Le, K. Mahesh, V. Chandra, K. S. Kim, *Nanoscale* **2013**, *5*, 3149–3171.

[244] a) S. Ahuja, T. R. N. Kutty, *J. Photochem. Photobiol., A* **1996**, *97*, 99–107; b) H. Fu, J. Lin, L. Zhang, Y. Zhu, *Appl. Catal., A* **2006**, *306*, 58–67; c) X. Fan, W. Cai, J. Zhang, *Appl. Catal., B* **2010**, *96*, 162–168; d) J. Yu, X. Yu, B. Huang, X. Zhang, Y. Dai, *Cryst. Growth Des.* **2009**, *9*, 1474–1480; e) G. K. Prasad, B. Singh, K. Batra, A. R. Srivatsava, K. Ganesan, R. Vijayaraghavan, *J. Mol. Catal. A: Chem.* **2011**, *349*, 55–62; f) L. Yin, H.-M. Cheng, *J. Am. Chem. Soc.* **2012**, *134*, 9070–9073; g) J. Yu, J. Zhang, S. Liu, *J. Phys. Chem. C* **2010**, *114*, 13642–13649; h) X. F. Cheng, D. P. Liu, J. Q. Zhang, C. N. Cao, *Chemosphere* **2007**, *68*, 1976–1984; i) J. Yu, X. Yu, *Environ. Sci. Technol.* **2008**, *42*, 4902–4907; j) J. X. Jiaguo, Y. B. Cheng, Y. Yu, J. Wang, *J. Solid State Chem.* **2005**, *178*, 1968–1972; k) X. Zhu, J. Zhang, F. Chen, *Chemosphere* **2010**, *78*, 1350–1355; l) A. G. S. Prado, L. B. Bolzon,

C. P. Pedroso, A. O. Moura, L. L. Costa, *Appl. Catal., B* **2008**, *82*, 219–224; m) P. Ctibor, H. Ageorges, V. Stengl, N. Murafa, I. Pis, T. Zahoranova, V. Nehasil, Z. Pala, *Ceram. Int.* **2011**, *37*, 2561–2567; n) Y. Wang, G. Ding, P. Yuan, *Mater. Res. Bull.* **2013**, *48*, 869–877; o) A. Ishikawa, J. N. Kondo, M. Hara, H. Kobayashi, K. Domen, *J. Am. Chem. Soc.* **2002**, *124*, 13547–13553; p) J. Y. Gaopeng, G. Liu, *J. Phys. Chem. C* **2012**, *116*, 15519–15524; q) see reference [5a].

[245] a) T. S. Sreeprasad, K. P. Lisha, T. Pradeep, *J. Hazard. Mater.* **2011**, *186*, 921–931; b) B. Li, H. Cao, G. Yin, *J. Mater. Chem.* **2011**, *21*, 13765–13768; c) B. Li, J. Yin, J. H. Warner, *J. Mater. Chem.* **2012**, *22*, 1876–1883; d) S. M. Maliyekkal, T. S. Sreeprasad, D. Krishnan, S. Kouser, A. K. Mishra, U. V. Waghmare, T. Pradeep, *Small* **2013**, *9*, 273–283; e) S. Soujit, S. Mundampra, T. Pradeep, *ACS Appl. Mater. Interfaces* **2012**, *4*, 4156–4163.

[246] A. W. Rowan, *Carbon* **2011**, *49*, 741–772.

[247] a) S. Liu, M. Q. Yang, Y. J. Xu, *J. Mater. Chem. A* **2014**, *2*, 430–440; b) M. O. Vasilios, B. Athanasios, V. Chandra, N. Kim, K. C. Kemp, *Chem. Rev.* **2012**, *112*, 6156–6214; c) see reference [5a]; d) R. Sungjin, *Nat. Nanotechnol.* **2009**, *4*, 217–214; e) X. Huang, Z. Zeng, Z. Fan, J. Liu, H. Zhang, *Adv. Mater.* **2012**, *24*, 5979–6004; f) Q. Xiang, J. Yu, M. Jaroniec, *Chem. Soc. Rev.* **2012**, *41*, 782–796; g) Y. Liu, X. Dong, P. Chen, *Chem. Soc. Rev.* **2012**, *41*, 2283–2307; h) W. Choi, R. Seelaboyina, Y. S. Kang, *Crit. Rev. Solid State Mater. Sci.* **2010**, *35*, 52–71; i) P. V. Kamat. V. Ian, *Nano Lett.* **2010**, *10*, 577–583; j) see reference [60]; k) H. Zhang, X. Lv, Y. Li, Y. Wang, J. Li, *ACS Nano* **2010**, *4*, 380–386; l) see reference [87].

[248] a) W. Wang, P. Kalck, J. Faria, *J. Mol. Catal. A: Chem.* **2005**, *235*, 194–199; b) Y. Long, Y. Lu, Y. Huang, Y. Peng, Y. Lu, S.-Z. Kang, J. Mu, *J. Phys. Chem. C* **2009**, *113*, 13899–13905; c) A. Mills, S. Le Hunte, *J. Photochem. Photobiol., A* **1997**, *108*, 1–35.

[249] A. Fujishima, K. Kohayakawa, K. Honda, *J. Electrochem. Soc.* **1975**, *122*, 1487–1489.

[250] See reference [41a].

[251] H. Wang, L. Zhang, Z. Chen, J. Hu, S. Li, Z. Wang, J. Liu, X. Wang, *Chem. Soc. Rev.* **2014**, *43*, 5234–5244.

[252] Y. H. Ng, I. V. Lightcap, K. Goodwin, M. Matsumura, P. V. Kamat, *J. Phys. Chem. Lett.* **2010**, *1*, 2222–2227.

[253] a) See reference [33c]; b) see reference [247k]; c) I. Y. Kim, J. M. Lee, T. W. Kim, H. N. Kim, H. Kim, W. Choi, S.-J. Hwang, *Small* **2012**, *8*, 1038–1048; d) D. Zhao, G. Sheng, C. Chen, X. Wang, *Appl. Catal., B* **2012**, *111–112*, 303–308; e) B. Jiang, C. Tian, W. Zhou, J. Wang, Y. Xie, Q. Pan, Z. Ren, Y. Dong, D. Fu, J. Han, H. Fu, *Chem. Eur. J.* **2011**, *17*, 8379–8387; f) W. Tu, Y. Zhou, Q. Liu, S. Yan, S. Bao, X. Wang, M. Xiao, Z. Zou, *Adv. Funct. Mater.* **2013**, *23*, 1743–1749.

[254] F. Wang, K. Zhang, *Curr. Appl. Phys.* **2012**, *12*, 346–352.

[255] Y. Zhang, C. Pan, *J. Mater. Sci.* **2011**, *46*, 2622–2626.

[256] a) H. Adamu, P. Dubey, J. A. Anderson, *Chem. Eng. J.* **2016**, *284*, 380–388; b) P. Calza, C. Hadjicostas, V. A. Sakkas, M. Sarro, C. Minero, C. Medana, T. A. Albanis, *Appl. Catal., B* **2016**, *183*, 96–106; c) F. Wu, W. Liu, J. Qiu, J. Li, W. Zhou, Y. Fang, S. Zhang, X. Li, *Appl. Surf. Sci.* **2015**, *358*, 425–435.

[257] a) C. Han, M.-Q. Yang, B. Weng, Y.-J. Xu, *Phys. Chem. Chem. Phys.* **2014**, *16*, 16891–16903; b) R. Cai, J. Wu, L. Sun, Y. Liu, T. Fang, S. Zhu, S. Li, Y. Wang, L. Guo, C. Zhao, A. Wei, *Mater. Des.* **2015**, *90*, 839–844.

[258] H. Fakhri, A. R. Mahjoub, A. H. Cheshme Khavar, *Mater. Sci. Semicond. Process.* **2016**, *41*, 38–44.

[259] a) S. Song, B. Cheng, N. Wu, A. Meng, S. Cao, J. Yua, *Appl. Catal., B* **2016**, *181*, 71–78; b) D. Zhang, H. Tang, Y. Wang, K. Wu, H. Huang, G. Tang, J. Yang, *Appl. Surf. Sci.* **2014**, *319*, 306–311.

[260] P. Madhusudan, J. Yu, W. Wang, B. Cheng, G. Liu, *Dalton Trans.* **2012**, *41*, 14345–14353.

[261] L. Sun, G. Wang, R. Hao, D. Han, S. Cao, *Appl. Surf. Sci.* **2015**, *358*, 91–99.

[262] a) J. Li, L. Wei, C. Yu, W. Fang, Y. Xie, W. Zhou, L. Zhu, *Appl. Surf. Sci.* **2015**, *358*, 168–174; b) X. Pan, Y. J. Xu, *J. Phys. Chem. C* **2015**, *119*, 7184–7194; c) Y. Zhang, N. Zhang, Z.-R. Tang, Y. Xu, *ACS Nano* **2012**, *6*, 9777–9789; d) T. Xu, H. Cheng, Y. Zhu, *Appl. Catal., B* **2011**, *101*, 382–387; e) M. Zhu, P. Chen, M. Liu, *ACS Nano* **2011**, *5*, 4529–4536; f) G. Liao, X. Quan, H. Yu, H. Zhao, *J. Mater. Chem.* **2012**, *22*, 2721–2726; g) Z. Xiong, L. L. Zhang, X. S. Zhao, *Chem. Eur. J.* **2011**, *17*, 2428–2434; h) B. Li, H. Cao, G. Yin, Y. Lu, J. Yin, *J. Mater. Chem.* **2011**, *21*, 10645–10648; i) W. Zhang, F. Dong, W. Zhang, *Appl. Surf. Sci.* **2015**, *358*, 75–83; j) S. H. Hsieh, W. J. Chen, T. H. Yeh, *Appl. Surf. Sci.* **2015**, *358*, 63–69; k) G. Li, W. Wang, Y. Cai, H. Yip, H. Zhao, P. Wong, *Appl. Surf. Sci.* **2015**, *358*, 137–145; l) Y. Zhang, H. Huang, Y. He, B. Fei, F. Lv, *Appl. Surf. Sci.* **2014**, *319*, 272–277; m) W. Wang, Q. Xiang, B. Cheng, *Appl. Catal., B* **2012**, *119–120*, 109–116; n) Y. Zhang, X. Fu, Y. Xu, *ACS Nano* **2011**, *5*, 7426–7435.

[263] a) T. Wagner, C. Weinberger, D. Klaus, M. Tiemann, *Chem. Soc. Rev.* **2013**, *42*, 4036–4053; b) C. Li, H. Bai, G. Shi, *Chem. Soc. Rev.* **2009**, *38*, 2397–2409; c) W. Yuan, G. Shi, *J. Mater. Chem. A* **2013**, *1*, 10078–10091; d) H. Ullah, A. A. Shah, S. Bilal, K. Ayub, *J. Phys. Chem. C* **2013**, *117*, 23701–23711; e) H. Ullah, A. A. Shah, K. Ayub, S. Bilal, *J. Phys. Chem. C* **2013**, *117*, 4069–4078; f) H. Ullah, A. A. Shah, S. Bilal, K. Ayub, *J. Phys. Chem. C* **2014**, *118*, 17819–17830; g) S. Bibi, H. Ullah, S. M. Ahmad, A. A. Shah, S. Bilal, A. A. Tahir, K. Ayub, *J. Phys. Chem. C* **2015**, *119*, 15994–16003; h) H. Ullah, K. Ayub, Z. Ullah, M. Hanif, R. Nawaz, S. Bilal, *Synth. Met.* **2013**, *172*, 14–20.

[264] a) See reference [29]; b) Y. Zhang, H. L. Stormer, P. Kim, *Nature* **2005**, *438*, 201–204; c) T. Kuila, S. Bose, P. Khanra, A. K. Mishra, N. H. Kim, J. H. Lee, *Biosens. Bioelectron.* **2011**, *26*, 4637–4648.

[265] a) A. A. Balandin, S. Rumyantsev, M. S. Shur, *IEEE Electron Device Lett.* **2009**, *30*, 288–290; b) K. R. Ratinac, W. Yang, S. P. Ringer, *Env. Sci. Technol.* **2010**, *44*, 1167–1176; c) Y. M. Lin, P. Avouris, *Nano Lett.* **2008**, *8*, 2119–2125; d) see reference [4].

[266] a) See reference [14]; b) J. T. Robinson, F. K. Perkins, E. S. Snow, Z. Wei, *Nano Lett.* **2008**, *8*, 3137–3140; c) S. Jain, K. E. Roberts, S. Park, R. S. Ruoff, *Angew. Chem. Int. Ed.* **2010**, *49*, 2154–2157; d) T. H. Han, Y.-K. Huang, A. T. L. Tan, V. P. Dravid, J. Huang, *J. Am. Chem. Soc.* **2011**, *133*, 15264–15267; e) see reference [15b].

[267] D. Jesse. C. Vincent. Y. Yang, R. B. Kaner, B. H. Weiller, *ACS Nano* **2009**, *3*, 301–306.

[268] M. W. Jung, W. Song, M. Kang, S. Kim, C. Yang, S. S. Lee, J. Lim, C. Park, J.-O. Lee, K.-S. An, *ACS Appl. Mater. Interfaces* **2014**, *6*, 13319–13323.

[269] S. Paek, M. Akada, J. P. Hill, A. Vinu, K. Ariga, *Angew. Chem. Int. Ed.* **2010**, *49*, 9737–9739.

[270] a) Y. Guo, J. Rong, Y. Gong, L. Wu, X. Zhang, P. Li, J. Xu, G. Cheng, M. Sun, L. Liu, *ACS Nano* **2011**, *5*, 6955–6961; b) S. Dubin, R. B. Kaner, K. Kalantar-Zadeh, *J. Phys. Chem. C* **2010**, *114*, 13796–13801; c) J. Nicolosi, C. Y. Chang, V. Chen, W. Strupinski, *Sens. Actuators, B* **2011**, *157*, 500–503; d) L. Al-Mashat, K. Shin, K. Kalantar-Zadeh, *J. Phys. Chem. C* **2010**, *114*, 16168–16173.

[271] G. Singh, D. Haranatha, G. Joshi, N. Singh, S. Singh, R. Pasricha, *Carbon* **2012**, *50*, 385–394.

[272] J. G. Yu, X. H. Zhao, L. Y. Yu, F. P. Jiao, J. H. Jiang, X. Q. Chen, *J. Radioanal. Nucl. Chem.* **2014**, *299*, 1155–1163.

[273] See reference [3].

[274] X.-Y. Yu, R. X. Xu, J. H Liu, X.-J. Huang, *ACS Appl. Mater. Interfaces* **2012**, *4*, 4672–4682.

[275] M. A. Ferreira, A. A. Barros, *Anal. Chem. Acta* **2002**, *459*, 151–159.

[276] H. P. Wu, *Anal. Chem.***1996**, *68*, 1639–1645.

[277] a) Y. Y. Mohammad, A. Saleh, M. Rezaee, M. Ghambarian, R. Hassani, *Anal. Chem. Acta* **2010**, *659*, 172–177; b) L. Rui, P. Liang, *J. Hazard. Mater.* **2008**, *152*, 166–171; c) Y. Liu, L. Guo, *Talanta* **2005**, *68*, 25–30.

[278] a) J. Gong, L. Wang, X. Miao, L. Zhang, *Electrochem. Commun.* **2010**, *12*, 1658–1661; b) D. Du, M. Wang, J. Zhang, J. Cai, H. Tu, A. Zhang, *Electrochem. Commun.* **2008**, *10*, 85–89.

[279] a) D. Suna, Y. Cai, H. Zhang, K. Wu, *Anal. Chem. Acta* **2007**, *581*, 27–31; b) S. H. Kangbing, J. Fei, W. Bai, *Anal. Chem. Acta* **2003**, *489*, 215–221; c) R. Yang, J. Zhai, *Electroanalysis* **2008**, *20*, 527–533; d) J. Dongyue, J. Wang, *Talanta* **2010**, *83*, 332–336.

[280] S. He, B. Song, D. Li, C. Zhu, W. Qi, Y. Wen, C. Fan, *Adv. Funct. Mater.* **2010**, *20*, 453–459.

[281] F. Wen, S. He, S. Song, L. Wang, Y. Long, D. Li, C. Fan, *Chem. Commun.* **2010**, *46*, 2596–2598.

[282] See reference [15b].

[283] M. Zhang, W. Tan, B. Ye, *Biosens. Bioelectron.* **2011**, *26*, 3260–3265.

[284] T. Zhang, Y. Wang, Z. Li, C. Wang, Y. Li, Y. Fang, *Nano Lett.* **2010**, *10*, 4738–4741.

[285] Q. H. Herry, H. Zhang, P. Chen, *ACS Nano* **2011**, *5*, 1990–1994.

[286] J. P. Vimlesh, Y. Chun, J. Lee, I. Hwang, S. Kim, *ACS Nano* **2010**, *4*, 3979–3986.

[287] M. Sun, H. Qiu, *J. Mater. Chem.* **2012**, *22*, 24577–24583.

[288] a) X. Zhang, R. Mab, B. Cao, *J. Mater. Chem.* **2012**, *22*, 8767–8771; b) K. H. Madadrang, N. Wang, H. Feng, S. Hou, *ACS Appl. Mater. Interfaces* **2012**, *4*, 1186–1193.

[289] a) N. L. Rosi, C. A. Mirkin, *Chem. Rev.* **2005**, *105*, 1547–1562; b) see reference [247g].

[290] a) N. Varghese, U. Mogera, A. Govindaraj, A. Das, P. K. Maiti, A. K. Sood, C. N. R. Rao, *ChemPhysChem* **2009**, *10*, 206–210; b) C.-H. Lu, H.-H. Yang, C.-L. Zhu, X. Chen, G.-N. Chen, *Angew. Chem. Int. Ed.* **2009**, *48*, 4785–4787.

[291] a) O. Akhavan, E. Ghaderi, *J. Phys. Chem. C* **2009**, *113*, 20214–20220; b) S. Alwarappan, C. Liu, A. Kumar, C.-Z. Li, *J. Phys. Chem. C* **2010**, *114*, 12920–12924; c) L. Cui, Z. Chen, Z. Zhu, X. Lin, X. Chen, C. J. Yang, *Anal. Chem.* **2013**, *85*, 2269–2275; d) A. M. Pinto, I. C. Gonçalves, F. D. Magalhães, *Colloids Surf., B* **2013**, *111*, 188–202; e) K. Wang, J. Ruan, H. Song, J. Zhang, Y. Wo, S. Guo, D. Cui, *Nanoscale Res. Lett.* **2011**, *6*, 8.

[292] H. Liu, C.-a. Tao, Z. Hu, S. Zhang, J. Wang, Y. Zhan, *RSC Adv.* **2014**, *4*, 43624–43629.

[293] a) C. Chung, Y.-K. Kim, D. Shin, S.-R. Ryoo, B. H. Hong, D.-H. Min, *Acc. Chem. Res.* **2013**, *46*, 2211–2224; b) A. Wisitsoraat, A. Tuantranont, in *Applications of Nanomaterials in Sensors and Diagnostics* (Ed.: A. Tuantranont), Springer, Berlin/Heidelberg, **2013**, Vol. 14, pp. 103–141; c) S. Guo, S. Dong, *J. Mater. Chem.* **2011**, *21*, 18503–18516.

[294] H. Dong, W. Gao, F. Yan, H. Ji, H. Ju, *Anal. Chem.* **2010**, *82*, 5511–5517.

[295] R. S. Swathi, K. L. Sebastian, *J. Chem. Phys.* **2008**, *129*, 054703–054712.

[296] a) L. Xie, X. Ling, Y. Fang, J. Zhang, Z. Liu, *J. Am. Chem. Soc.* **2009**, *131*, 9890–9891; b) Y. Xu, Z. Liu, X. Zhang, Y. Wang, J. Tian, Y. Huang, Y. Ma, X. Zhang, Y. Chen, *Adv. Mater.* **2009**, *21*, 1275–1279.

[297] M. Liu, H. Zhao, X. Quan, S. Chen, X. Fan, *Chem. Commun.* **2010**, *46*, 7909–7911.

[298] H. Dong, J. Zhang, H. Ju, H. Lu, S. Wang, S. Jin, K. Hao, H. Du, X. Zhang, *Anal. Chem.* **2012**, *84*, 4587–4593.

[299] X.-H. Zhao, R.-M. Kong, X.-B. Zhang, H.-M. Meng, W.-N. Liu, W. Tan, G.-L. Shen, R.-Q. Yu, *Anal. Chem.* **2011**, *83*, 5062–5066.

[300] F. Long, A. Zhu, H. Shi, H. Wang, *Anal. Chem.* **2014**, *86*, 2862–2866.

[301] a) L. Wu, H. S. Chu, W. S. Koh, E. P. Li, *Opt. Express* **2010**, *18*, 14395–14400; b) S. Zeng, S. Hu, J. Xia, T. Anderson, X.-Q. Dinh, X.-M. Meng, P. Coquet, K.-T. Yong, *Actuator B Chem* **2015**, *207*, 801–810; c) B. Song, D. Li, W. Qi, M. Elstner, C. Fan, H. Fang, *ChemPhysChem* **2010**, *11*, 585–589.

[302] a) Y.-K. Kim, S. W. Han, D.-H. Min, *ACS Appl. Mater. Interfaces* **2012**, *4*, 6545–6551; b) see reference [28]; c) Y.-K. Kim, H.-K. Na, Y. W. Lee, H. Jang, S. W. Han, D.-H. Min, *Chem. Commun.* **2010**, *46*, 3185–3187; d) X. Qi, H. Li, J. W. Y. Lam, X. Yuan, J. Wei, B. Z. Tang, H. Zhang, *Adv. Mater.* **2012**, *24*, 4191–4195.

[303] a) R. J. Forster, P. Bertoncello, T. E. Keyes, *Annu. Rev. Anal. Chem.* **2009**, *2*, 359–385; b) A. Devadoss, L. Dennany, C.

Dickinson, T. E. Keyes, R. J. Forster, *Electrochem. Commun.* **2012**, *19*, 43–45.
[304] a) A. Devadoss, A.-M. Spehar-Délèze, D. A. Tanner, P. Bertoncello, R. Marthi, T. E. Keyes, R. J. Forster, *Langmuir* **2009**, *26*, 2130–2135; b) A. Devadoss, C. Dickinson, T. E. Keyes, R. J. Forster, *Anal. Chem.* **2011**, *83*, 2383–2387; c) E. J. O'Reilly, T. E. Keyes, R. J. Forster, L. Dennany, *Analyst* **2013**, *138*, 677–682.
[305] a) S. Zhang, Y. Shao, H.-g. Liao, J. Liu, I. A. Aksay, G. Yin, Y. Lin, *Chem. Mater.* **2011**, *23*, 1079–1081; b) S. Wang, X. Wang, S. P. Jiang, *Phys. Chem. Chem. Phys.* **2011**, *13*, 6883–6891; c) Y. Su, Y. Lv, *RSC Adv.* **2014**, *4*, 29324–29339.
[306] Z. Guo, T. Hao, S. Du, B. Chen, Z. Wang, X. Li, S. Wang, *Biosens. Bioelectron.* **2013**, *44*, 101–107.
[307] K. Shao, J. Wang, X. Jiang, F. Shao, T. Li, S. Ye, L. Chen, H. Han, *Anal. Chem.* **2014**, *86*, 5749–5757.
[308] a) C. H. Wang, C. Yang, Y. Y. Song, W. Gao, X. H. Xia, *Adv. Funct. Mater.* **2005**, *15*, 1267–1275; b) Y. Xiao, F. Patolsky, E. Katz, J. F. Hainfeld, I. Willner, *Science* **2003**, *299*, 1877–1881.
[309] a) W.-J. Lin, C.-S. Liao, J.-H. Jhang, Y.-C. Tsai, *Electrochem. Commun.* **2009**, *11*, 2153–2156; b) Q. Lu, X. Dong, L.-J. Li, X. Hu, *Talanta* **2010**, *82*, 1344–1348; c) see reference [264c]; d) A. T. E. Vilian, V. Mani, S.-M. Chen, B. Dinesh, S.-T. Huang, *Ind. Eng. Chem. Res.* **2014**, *53*, 15582–15589.
[310] X. Zuo, S. He, D. Li, C. Peng, Q. Huang, S. Song, C. Fan, *Langmuir* **2009**, *26*, 1936–1939.
[311] L. Wang, M. Xu, L. Han, M. Zhou, C. Zhu, S. Dong, *Anal. Chem.* **2012**, *84*, 7301–7307.
[312] Y. Liu, D. Yu, C. Zeng, Z. Miao, L. Dai, *Langmuir* **2010**, *26*, 6158–6160.
[313] M. Mallesha, R. Manjunatha, G. Suresh, J. Melo, S. F. D'Souza, T. Venkatesha, *J. Solid State Electrochem.* **2012**, *16*, 2675–2681.
[314] a) J. Song, L. Xu, C. Zhou, R. Xing, Q. Dai, D. Liu, H. Song, *ACS Appl. Mater. Interfaces* **2013**, *5*, 12928–12934; b) L. Li, Z. Du, S. Liu, Q. Hao, Y. Wang, Q. Li, T. Wang, *Talanta* **2010**, *82*, 1637–1641.
[315] Y. Zhang, X. Bai, X. Wang, K.-K. Shiu, Y. Zhu, H. Jiang, *Anal. Chem.* **2014**, *86*, 9459–9465.
[316] T. Yang, Q. Li, L. Meng, X. Wang, W. Chen, K. Jiao, *ACS Appl. Mater. Interfaces* **2013**, *5*, 3495–3499.
[317] E. Katz, I. Willner, *Electroanalysis* **2003**, *15*, 913–947.
[318] a) A. Gutes, B.-Y. Lee, C. Carraro, W. Mickelson, S.-W. Lee, R. Mabouduan, *Nanoscale* **2013**, *5*, 6048–6052; b) K. S. Kim, Y. M. Um, J.-r. Jang, W.-S. Choe, P. J. Yoo, *ACS Appl. Mater. Interfaces* **2013**, *5*, 3591–3598.
[319] L. Zhang, H. H. Mohamed, R. Dillert, D. Bahnemann, *J. Photochem. Photobiol., C* **2012**, *13*, 263–276.
[320] a) Z. Yue, F. Lisdat, W. J. Parak, S. G. Hickey, L. Tu, N. Sabir, D. Dorfs, N. C. Bigall, *ACS Appl. Mater. Interfaces* **2013**, *5*, 2800–2814; b) H. Tokudome, Y. Yamada, S. Sonezaki, H. Ishikawa, M. Bekki, K. Kanehira, M. Miyauchi, *Appl. Phys. Lett.* **2005**, *87*, 213901–213904.
[321] a) I. Willner, F. Patolsky, J. Wasserman, *Angew. Chem. Int. Ed.* **2001**, *40*, 1861–1864; b) P. C. Pandey, H. H. Weetall, *Anal. Chem.* **1994**, *66*, 1236–1241; c) W.-W. Zhao, J.-J. Xu, H.-Y. Chen, *Chem. Rev.* **2014**, *114*, 7421–7441; d) S. Liu, C. Li, J. Cheng, Y. Zhou, *Anal. Chem.* **2006**, *78*, 4722–4726.
[322] a) N. Haddour, J. Chauvin, C. Gondran, S. Cosnier, *J. Am. Chem. Soc.* **2006**, *128*, 9693–9698; b) H. B. Yildiz, R. Freeman, R. Gill, I. Willner, *Anal. Chem.* **2008**, *80*, 2811–2816.
[323] X. Zhang, S. Li, X. Jin, S. Zhang, *Chem. Commun.* **2011**, *47*, 4929–4931.
[324] a) X. Zhao, S. Zhou, L.-P. Jiang, W. Hou, Q. Shen, J.-J. Zhu, *Chem. Eur. J.* **2012**, *18*, 4974–4981; b) X. Zhao, S. Zhou, Q. Shen, L.-P. Jiang, J.-J. Zhu, *Analyst* **2012**, *137*, 3697–3703.
[325] A. Devadoss, P. Sudhagar, S. Das, S. Y. Lee, C. Terashima, K. Nakata, A. Fujishima, W. Choi, Y. S. Kang, U. Paik, *ACS Appl. Mater. Interfaces* **2014**, *6*, 4864–4871.
[326] F. Banhart, J. Kotakoski, A. V. Krasheninnikov, *ACS Nano* **2010**, *5*, 26–41.
[327] Y. Zhang, T.-T. Tang, C. Girit, Z. Hao, M. C. Martin, A. Zettl, M. F. Crommie, Y. R. Shen, F. Wang, *Nature* **2009**, *459*, 820–823.
[328] A. A. Green, M. C. Hersam, *J. Phys. Chem. Lett.* **2009**, *1*, 544–549.
[329] X. Hu, Q. Zhou, *Chem. Rev.* **2013**, *113*, 3815–3835.

Received: November 16, 2015
Published online: May 27, 2016

